

RICE UNIVERSITY

**Manipulation of Electromagnetic Fields with Plasmonic Nanostructures:**  
*Nonlinear Frequency Mixing, Optical Manipulation, Enhancement and  
Suppression of Photocurrent in a Silicon Photodiode,  
and Surface-Enhanced Spectroscopy*

by

**Nathaniel K Grady**

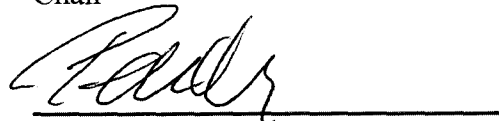
A THESIS SUBMITTED  
IN PARTIAL FULFILLMENT OF THE  
REQUIREMENTS FOR THE DEGREE

**Doctor of Philosophy**

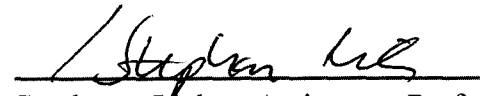
APPROVED, THESIS COMMITTEE:



Naomi J. Halas, Stanley C. Moore Professor of  
Electrical and Computer Engineering,  
Professor of Bioengineering, Professor of  
Chemistry, Professor of Physics Astronomy,  
Chair



Peter Nordlander, Professor of Physics and  
Astronomy, Professor of Electrical and  
Computer Engineering



Stephan Link, Assistant Professor of  
Chemistry, Assistant Professor of Electrical  
and Computer Engineering

HOUSTON, TX  
MAY 2010

UMI Number: 3421182

All rights reserved

INFORMATION TO ALL USERS

The quality of this reproduction is dependent upon the quality of the copy submitted.

In the unlikely event that the author did not send a complete manuscript and there are missing pages, these will be noted. Also, if material had to be removed, a note will indicate the deletion.



UMI 3421182

Copyright 2010 by ProQuest LLC.

All rights reserved. This edition of the work is protected against unauthorized copying under Title 17, United States Code.



ProQuest LLC  
789 East Eisenhower Parkway  
P.O. Box 1346  
Ann Arbor, MI 48106-1346

## **ABSTRACT**

Manipulation of Electromagnetic Fields with Plasmonic Nanostructures:  
*Nonlinear Frequency Mixing, Optical Manipulation, Enhancement and  
Suppression of Photocurrent in a Silicon Photodiode,  
and Surface-Enhanced Spectroscopy*

by

**Nathaniel K Grady**

Metallic nanostructures are one of the most versatile tools available for manipulating light at the nanoscale. These nanostructures support surface plasmons, which are collective excitations of the conduction electrons that can exist as propagating waves at a metallic interface or as localized excitations of a nanoparticle or nanostructure. Plasmonic structures can efficiently couple energy from freely propagating electromagnetic waves to localized electromagnetic fields and vice-versa, essentially acting as an optical antenna. As a result, the intensity of the local fields around and inside the nanostructure are strongly enhanced compared to the incident radiation.

In this thesis, this ability to manipulate electromagnetic fields on the nanoscale is employed to control a wide range of optical phenomena. These studies are performed using structures based on metallic nanoshells, which consist of a thin Au shell coating a silica nanosphere. To investigate the parameters controlling the plasmonic response of metallic nanoshells, two changes to the nanoshell composition are studied: (1) the Au shell is replaced with Cu which has interband transitions that strongly influence the plasmon resonance, and (2) the silica core is replaced by a semiconducting  $\text{Cu}_2\text{O}$  core

which has a significantly higher dielectric constant and non-trivial absorbance. The focusing of electromagnetic energy into intense local fields by plasmonic nanostructures is then directly investigated by profiling the nanoshell near field using a Raman-based molecular ruler. Next, plasmons supported by Au nanoshells are used to control the fluorescence of near-infrared fluorophores placed at controlled distances from the nanoshell surface. In this context, the analogy of an optical antenna is very relevant: the enhanced field at the surface of the nanoshell increases the absorption of light by the fluorophore, or equivalently couples propagating electromagnetic waves into a localized receiver, while the large scattering cross section enhances the coupling of energy from a localized source, the fluorophore, to far-field radiation. Excellent agreement with models based on Mie theory is achieved for both Raman and fluorescence. Experimentally measured enhancements of the radiative decay rate for fluorophores on Au nanoshells and Au nanorods are also consistent with this model. Plasmonic nanostructures can also control the flow of light into larger structures. This is observed by measuring the nanoparticle-induced enhancement and suppression of photocurrent in a silicon photodiode is at the single particle level for silica nanospheres, Au nanospheres, and two types of Au nanoshell. Finally, the simultaneous physical manipulation of an individual plasmonic nanostructure on the few-nanometer scale using light and detection of the local electromagnetic field during this ongoing process with the same incident beam is performed. For this experiment, a Au nanoshell is separated from a metallic surface by a few-nanometer thick polymer layer to form a nanoscale junction, or nanogap. Illuminating this structure with ultrashort optical pulses, exciting the plasmon resonance, results in a continuous, monitorable collapse of the nanogap. An easily detectable four-

wave mixing (FWM) signal is simultaneously generated by this illumination of the nanogap, providing a continuous, highly sensitive optical monitor of the nanogap spacing while it is being optically reduced. The dramatic increase in this signal upon contact provides a clear, unambiguous signal of the gap closing.

## **Acknowledgments**

First and foremost, I have to thank my parents, Michael and Carolyn Grady, who have served as a constant inspiration to open my mind and think about the world around me. Their example has instilled in me the work ethic that I should never aim for “good enough,” rather I should push myself to do the best I can, without which I never would have made it to graduate school. My dad’s unwavering willingness to answer questions, help me with chemistry sets and electronics kits, bring me along to help set up undergraduate labs and explain what they were about when I was growing up is what inspired me to follow in his footsteps and study physics. My adviser and mentor, Naomi Halas, and Peter Nordlander have both been instrumental in helping develop the ideas in this thesis. Finally, I’d like to thank all the members of the Halas group, whose ideas, criticisms, and support has helped refine the ideas in this thesis. Finally, I have to thank quite a few people who helped me make it through the traumatic events in my personal life over the last year including my family, especially my parents, siblings, aunt Marie and uncle Tom who all came down to Houston; my advisor Naomi Halas who has been unendingly supportive and understanding; and all the members of the Halas group.

## Table of Contents

<b>Chapter 1. Introduction .....</b>	<b>1</b>
<b>Chapter 2. Electromagnetic properties of nanoparticles .....</b>	<b>4</b>
2.1 Plasmon hybridization.....	4
2.2 Mie theory .....	8
2.3 Surface-enhanced Raman scattering.....	9
2.4 Fluorescence Enhancement by Plasmonic Nanoantennas.....	11
<b>Chapter 3. Cu nanoshells: effects of interband transitions on the nanoparticle plasmon resonance .....</b>	<b>13</b>
<b>Chapter 4. Metallic nanoshells with semiconducting Cu<sub>2</sub>O cores .....</b>	<b>26</b>
4.1 Results and Discussion.....	30
4.2 Conclusions .....	56
<b>Chapter 5. Profiling the Near Field of a Nanoshell with Raman-Based Molecular Rulers.....</b>	<b>57</b>
<b>Chapter 6. Nanoscale Control of Near-Infrared Fluorescence Enhancement Using Au Nanoshells.....</b>	<b>69</b>
6.1 Fabrication of Nanoshell-ICG Conjugates.....	73
6.1.1 NS@SiO <sub>2</sub> fabrication: .....	73
6.1.2 ICG Binding to NS@SiO <sub>2</sub> Nanoparticles: .....	74
6.2 Characterization of Nanoshell-ICG Conjugates .....	75
6.3 Experimental Fluorescence Enhancement .....	78
6.4 Calculated Fluorescence Enhancement.....	80
6.5 Calculated Quantum Yield and Lifetime .....	85
6.6 Conclusions .....	86
<b>Chapter 7. Fluorescence Enhancement by Au nanostructures: Nanoshells and Nanorods .....</b>	<b>88</b>

7.1	Introduction .....	88
7.2	Fabrication of Nanoparticle-Fluorophore Conjugates .....	92
7.2.1	Nanoparticle Fabrication .....	92
7.2.2	Protein and Fluorophore Conjugation .....	93
7.2.3	Protein-Fluorophore Complex Binding to Nanoparticles .....	94
7.2.4	Calculation of surface area available for HSA-IR800 to bind to nanoparticles .....	95
7.2.5	Calculation of no. of HSA-IR800 molecules bound to the nanoparticles.....	96
7.3	Characterization of Nanoparticle-Fluorophore Conjugates .....	97
7.4	Experimental Fluorescence Enhancement .....	101
7.5	Calculated and Experimental Scattering Efficiency of Nanostructures.....	102
7.6	Frequency Domain Lifetime Decay.....	105
7.7	Experimental Quantification of Quantum Yield .....	109
7.8	Conclusions .....	113
<b>Chapter 8. Nanoparticle-Induced Enhancement and Suppression of Photocurrent in a Silicon Photodiode.....</b>		<b>114</b>
8.1	Structure .....	116
8.2	Measurement .....	119
8.3	Results.....	121
8.4	Conclusions .....	130
<b>Chapter 9. Optically-Driven Collapse of a Plasmonic Nanogap Self-monitored by Optical Frequency Mixing .....</b>		<b>132</b>
9.1	Apparatus .....	135
9.2	Sample Fabrication .....	139
9.3	Results.....	140
9.4	Conclusions .....	149

**Chapter 10. Bibliography..... 150**

## List of Figures

<b>Figure 2-1</b> Incompressible fluid model for oscillating plasmons in a solid metallic sphere. The metal (green) is composed of a fixed ion background (blue) and an oscillating electron fluid (yellow).....	4
<b>Figure 2-2</b> (A) Schematic diagram of a nanoshell. (B) Hybridization diagram for a Au shell - SiO <sub>2</sub> core nanoshell.....	5
<b>Figure 2-3</b> Horizontal lines: dipole plasmon resonance for a Au sphere immersed in air ( $\epsilon_m = 1.00$ ) or H <sub>2</sub> O ( $\epsilon_m = 1.77$ ). Blue curve: dipole plasmon resonance for a spherical cavity in Au ( $\omega_s$ ) as a function of the dielectric constant ( $\epsilon_c$ ) of the material inside the cavity. Points corresponding to a silica core ( $\epsilon_c = 2.04$ , $\blacklozenge$ ), a Cu <sub>2</sub> O core ( $\epsilon_c \approx 7.1$ to $9.1$ , $\blacksquare$ ), and an iron oxide core ( $\epsilon_c \approx 12$ , $\bullet$ ) are indicated in black along the cavity plasmon line.....	6
<b>Figure 2-4</b> Energy level diagram for Raman scattering.....	10
<b>Figure 3-1</b> Theoretically calculated far field extinction of a solid nanosphere (black solid curves) and nanoshell (blue solid curves) made of (A) Ag, (B) Au, and (C) Cu. The nanospheres are 20 nm in radius and the nanoshells are 63 nm in core (silica) radius and 10 nm in shell thickness. The refractive index of ethanol ( $n = 1.36$ ) is used as the refractive index of the medium surrounding the particles. Dielectric function (red curves) of (A) Ag, (B) Au, and (C) Cu are also shown. $\epsilon'$ and $\epsilon''$ are the real and imaginary parts of the dielectric constants, respectively. The green shaded areas indicate the wavelength regions where interband transitions of the metals occur. ....	16
<b>Figure 3-2</b> (A) Theoretically calculated far-field extinction of a Cu nanoshell with core radius of 63 nm and shell thickness of 10 nm. Near-field patterns of the dipole resonance excited at (B) 550 nm and (C) 720 nm. The polarization ( <b>E</b> ) and propagation ( <b>k</b> ) vectors are indicated in (C).....	19
<b>Figure 3-3</b> (A) Theoretically calculated far-field extinction of a Cu nanoshell with core radius of 63 nm and shell thickness of 40 nm. (B) Near-field pattern in the plane containing the polarization and propagation vectors as indicated in the Figure 3-2. The color bars indicate the magnitude of the $ \mathbf{E} ^2$ . The columns indicate the excitation wavelengths. The first row includes the first 5 terms in the Mie expansion, the second row contains only the first (dipole) term, and the third row only includes the second (quadrupole) term. ....	19
<b>Figure 3-4</b> (A) Illustration of the fabrication of Cu nanoshells. SEM (B) and TEM (C) images of the seed particles. SEM (D) and TEM (E) images of Cu nanoshells (63 + 8 nm core radius and 30 + 4 nm shell thickness).....	22

**Figure 3-5** Extinction spectra of Cu nanoshells with core radius of  $63 \pm 8$  nm and shell thickness of (A)  $52 \pm 7$  nm, (B)  $45 \pm 6$  nm, (C)  $38 \pm 5$  nm, and (D)  $30 \pm 4$  nm. The solid curves are the experimentally measured extinction spectra of Cu nanoshells dispersed in ethanol. The dash curves are the theoretically calculated extinction (red), absorption (green), and scattering (blue) of the Cu nanoshells..... 24

**Figure 4-1** SEM images of  $\text{Cu}_2\text{O}$  nanoparticles of different sizes. The radii of the nanoparticles are (A)  $15 \pm 0.5$  nm, (B)  $30 \pm 1$  nm, (C)  $50 \pm 2$  nm, (D)  $100 \pm 5$  nm, (E)  $250 \pm 30$  nm, and (F)  $350 \pm 50$  nm..... 33

**Figure 4-2** (A) Optical image of  $\text{Cu}_2\text{O}$  nanoparticles dispersed in aqueous media of increasing sizes. (B) Experimental absorption spectra of the  $\text{Cu}_2\text{O}$  nanoparticles dispersed in aqueous media. The radius of the nanoparticles corresponding to the spectra is indicated on the right. Spectra are offset for clarity. (C) Calculated absorption spectra of the  $\text{Cu}_2\text{O}$  nanoparticles in aqueous media ( $n = 1.33$ ). The spectra are color coordinated with part (B) and offset for clarity. .... 34

**Figure 4-3** SEM images of  $\text{Cu}_2\text{O}/\text{Au}$ -NS of different sizes. (A)  $[r_1, r_2] = [15, 32]$  nm, (B)  $[r_1, r_2] = [30, 46]$  nm, (C)  $[r_1, r_2] = [40, 54]$  nm, (D)  $[r_1, r_2] = [50, 65]$  nm. The scale bar is 200 nm. .... 36

**Figure 4-4** (A) Optical image of  $\text{Cu}_2\text{O}/\text{Au}$ -NS of different sizes. (i)  $[r_1, r_2] = [15, 32]$  nm, (ii)  $[r_1, r_2] = [30, 46]$  nm, (iii)  $[r_1, r_2] = [40, 54]$  nm, and (iv)  $[r_1, r_2] = [50, 65]$  nm. (B) Experimental extinction spectra of  $\text{Cu}_2\text{O}/\text{Au}$ -NS dispersed in aqueous media of different sizes: (i)  $[r_1, r_2] = [15, 32]$  nm,  $\lambda_{\text{max}} = 610$  nm, (ii)  $[r_1, r_2] = [30, 46]$  nm,  $\lambda_{\text{max}} = 705$  nm (iii)  $[r_1, r_2] = [40, 54]$  nm,  $\lambda_{\text{max}} = 780$  nm and (iv)  $[r_1, r_2] = [50, 65]$  nm,  $\lambda_{\text{max}} = 830$  nm. Spectra are offset for clarity. (C) Calculated extinction spectra of the  $\text{Cu}_2\text{O}/\text{Au}$ -NS in aqueous media. The spectra are color coordinated with part (B) and offset for clarity. The calculations were performed assuming spherical core and shell geometry..... 38

**Figure 4-5** (A) Experimental extinction spectra of  $\text{Cu}_2\text{O}/\text{Au}$ -NS for core radius  $r_1 = 40 \pm 2$  nm with varying Au shell thicknesses: (i)  $r_2 = 54 \pm 5$  nm, (ii)  $57 \pm 5$  nm, (iii)  $60 \pm 7$  nm and (iv)  $63 \pm 11$  nm. (B) Calculated extinction spectra of  $\text{Cu}_2\text{O}/\text{Au}$ -NS of similar sizes as observed experimentally. The calculations were performed assuming a spherical core and shell geometry..... 40

**Figure 4-6** Plasmon hybridization diagram (left) and the surface charge overlaid on the near field intensity enhancement at the bonding (middle) and antibonding (right) plasmon resonance for Au nanoshells with (A-C)  $\text{SiO}_2$ , (D-F)  $\text{Cu}_2\text{O}$ , or (G-I) iron oxide cores. .... 41

**Figure 4-7** Real ( $\epsilon'$ ) and imaginary ( $\epsilon''$ ) parts of the complex dielectric function of  $\text{Cu}_2\text{O}$  obtained from ref. 26. .... 44

**Figure 4-8** Calculated extinction, absorption, and scattering efficiency spectra of  $\text{Cu}_2\text{O}/\text{Au}$ -NS (solid) compared with  $\text{SiO}_2/\text{Au}$ -NS (dash) nanostructures of different

sizes. (A-C)  $[r_1, r_2] = [30, 42]$  nm, (D-F)  $[r_1, r_2] = [40, 52]$  nm, (G-I)  $[r_1, r_2] = [50, 62]$  nm, (J-L)  $[r_1, r_2] = [60, 72]$  nm. The calculations are performed assuming a spherical core encapsulated in a spherical shell..... 47

**Figure 4-9** Calculated extinction (blue), absorption (red) and scattering (black) spectra of Cu<sub>2</sub>O/Au nanoshells of different sizes. Calculation performed using Mie theory assuming a spherical core and spherical shell with a constant real permittivity of 8 for the cores. .... 50

**Figure 4-10** Total optical absorption cross section for an  $[r_1, r_2] = [40, 52]$  nm Cu<sub>2</sub>O/Au-NS (solid black line), separated into the contribution from the core (solid red line) and shell (solid blue line). The total absorption cross section for a nanoshell of the same dimensions but a constant real  $\epsilon_c = 7.6$  is shown for comparison (dashed orange line). .... 50

**Figure 4-11** Effect of the core dielectric on (A-D) the peak near field intensity enhancement in the (—) core, (—) shell and (—) medium, and (E-H) far field (—) scattering, (—) absorption and (—) extinction at the (I-L) dipole plasmon resonance for nanoshells of four aspect ratios: (A,E,I)  $r_1 / r_2 = 15 \text{ nm} / 32 \text{ nm} = 0.47$ , (B,F,J)  $r_1 / r_2 = 30 \text{ nm} / 46 \text{ nm} = 0.65$ , (C,G,K)  $r_1 / r_2 = 40 \text{ nm} / 54 \text{ nm} = 0.74$ , and (D,H,L)  $r_1 / r_2 = 50 \text{ nm} / 65 \text{ nm} = 0.77$ . The dielectric function of the three oxides considered here are indicated by dashed vertical lines: SiO<sub>2</sub> at  $\epsilon_c = 2.04$ , Cu<sub>2</sub>O at  $\epsilon_c = 7.5$ , and iron oxide at  $\epsilon_c = 12$ ..... 52

**Figure 5-1.** Schematic diagram showing the bifunctional Raman-active molecular rulers at varying distances from the nanoshell surface ( $y$ -axis). Both the terminal fluorescein and adenine strand moieties used as building blocks are shown. The SERS spectrum for each molecular component of the ruler provides an independent SERS spectrum dependent on the nanoparticle's near field, as described in text..... 59

**Figure 5-2** Extinction spectra (black) and the calculated surface average  $\langle |E|^4 \rangle$ -field spectrum (red) for the two sizes of nanoshells. (a)  $[r_1, r_2] = [43, 58]$  nm nanoshells (b)  $[r_1, r_2] = [70, 91]$  nm nanoshells. The excitation laser wavelength at 785 nm (purple vertical line) and the emission peak for adenine (red vertical line) and fluorescein (green vertical line) analyzed are shown. .... 60

**Figure 5-3** (a) SERS spectra for DNA-fluorescein adsorbate layer on  $[r_1, r_2] = [43, 58]$  nm nanoshells and (b) same as (a) but for  $[r_1, r_2] = [70, 91]$  nm nanoshells. Spectra correspond to DNA strands of 2, 6 12 and 18 adenines, respectively. (c) SERS intensity of 1185 cm<sup>-1</sup> fluorescein peak (counts / 60 s). (■): Experimental values; solid lines: theoretically calculated values for  $[r_1, r_2] = [43, 58]$  nm nanoshells (d) same as (c) for  $[r_1, r_2] = [70, 91]$  nm nanoshells (counts/30s) (e) same as (c) for 736 cm<sup>-1</sup> adenine peak (f) same as (d) for 736 cm<sup>-1</sup> adenine peak. (g) The ratios of SERS intensities ( $I(\text{fluorescein}@1185 \text{ cm}^{-1})/I(\text{adenine}@736 \text{ cm}^{-1})$ ) as a function of distance from the nanoshell surface on  $[r_1, r_2] = [43, 58]$  nm nanoshells. (■): Experimental values; solid lines: theoretically calculated values (h) same as (g) for  $[r_1, r_2] = [70, 91]$  nm nanoshells..... 62

- Figure 5-4** Surface average  $\langle |G_{SERS}| \rangle$  as function of distance from nanoparticle surface for (a)  $[r_1, r_2] = [43, 58]$  nm nanoshells and (b)  $[r_1, r_2] = [70, 91]$  nm nanoshells. Circles (○) are calculated using Mie theory, solid line (—) is a fit to a dipole model, and dashed line (- -) is a fit to an exponential decay. **Inset:** The field intensity enhancement at the excitation and emission wavelength for the two nanoshells. The intensity color bar is the same for all the surface plots. .... 66
- Figure 6-1** Absorption–emission spectra ( $\lambda_{\max\text{-Ab}} = 780$  nm and  $\lambda_{\max\text{-Em}} = 820$  nm) and chemical structure (inset) of ICG..... 75
- Figure 6-2** (A) Schematic diagram of fabrication procedure, and TEM micrographs (B – F) of NS coated with varying thicknesses of silica epilayers (B)  $7 \pm 2$  nm (C)  $13 \pm 2$  nm (D)  $21 \pm 3$  nm (E)  $30 \pm 3$  nm (F)  $42 \pm 3$  nm. Scale bar is 50 nm for all TEM images..... 76
- Figure 6-3** Observed shift in the plasmon resonance peak with increasing thickness of silica layer surrounding the NS. (■) Experimental, and (—) calculated values for NS  $[r_1, r_2] = [60, 76]$  nm and NS@SiO<sub>2</sub> nanoparticles, with  $7 \pm 2$  nm,  $13 \pm 2$  nm,  $21 \pm 3$  nm,  $30 \pm 3$  nm,  $42 \pm 3$  nm,  $61 \pm 4$  nm, and  $90 \pm 4$  nm thick silica epilayers are shown..... 77
- Figure 6-4** (A) Schematic diagram of ICG conjugation on NS@SiO<sub>2</sub> nanoparticles, excitation and observed emission. (B) Fluorescence spectra of ICG conjugated at various distances from the NS surface. (—) Emission spectrum of control, ICG deposited on silica nanospheres is also included. (C) Fluorescence enhancement factor of ICG conjugated on NS@SiO<sub>2</sub> nanoparticles relative to silica nanospheres is shown as a function of thickness of silica layer surrounding the NS (color coordinated with reference to panel B). .... 79
- Figure 6-5** Fluorescence enhancement factor of ICG molecules adsorbed on NS without any silica layer (■) is represented showing strong quenching of ICG molecules. ICG molecules bound to NS@SiO<sub>2</sub> nanoparticles relative to silica nanospheres is also shown as a function of silica layer thickness surrounding the NS. The data points representing ICG-NS@SiO<sub>2</sub> nanoparticles are color coordinated with ref. to Figure 6-4B and C. .... 83
- Figure 6-6** (A) (■) Experimental, and (—) calculated values of fluorescence enhancement factor of ICG conjugated to NS@SiO<sub>2</sub> nanoparticles relative to ICG bound to silica nanospheres. (B)–(D) Calculated values of distance dependent fluorescence of ICG as a function of silica spacer thickness surrounding the NS. (B) Calculated surface average field enhancements, (C) Calculated radiative rate enhancements, (D) Calculated Q.E. enhancement of ICG conjugated to NS@SiO<sub>2</sub> nanoparticles relative to that of silica nanospheres. .... 84
- Figure 6-7** Calculated values of distance dependent fluorescence of ICG as a function of silica spacer thickness surrounding the Au-NS (a) quantum yield and (b) lifetime. .... 86

**Figure 7-1** (a) Absorption - emission profile ( $\lambda_{\max\text{-Ab}} \sim 782$  nm and  $\lambda_{\max\text{-Em}} \sim 804$  nm) of IR800 conjugated with HSA. Chemical structure of IR800 is provided as inset. (b) Schematic diagram illustrating the conjugation of HSA-IR800 protein-fluorophore complex to Nanoshells (NSs) and Nanorods (NRs) to form NSs-HSA-IR800 and NRs-HSA-IR800 respectively. The blue curved line represents HSA and red dots represent IR800 dye. .... 98

**Figure 7-2** TEM micrographs of (a) NSs [ $r_1, r_2$ ] = [63, 78] nm, (b) NSs coated with  $8 \pm 3$  nm HSA-IR800, (c) NRs [ $w, l$ ] = [11, 46] nm, and d) NRs coated with  $8 \pm 3$  nm HSA-IR800. .... 100

**Figure 7-3** Surface plasmon resonance shift when nanoparticles are conjugated with HSA-IR800 (a) NSs (solid red),  $\lambda_{\max} \sim 800$  nm and NSs coated with HSA-IR800 (dash),  $\lambda_{\max} \sim 805$  nm, and (b) NRs (solid blue),  $\lambda_{\max} \sim 796$  nm and NRs coated with HSA-IR800 (dash),  $\lambda_{\max} \sim 804$  nm. The peak at 280 nm is protein absorbance peak. ... 100

**Figure 7-4** (a) Extinction spectra of (i) NSs-HSA-IR800, plasmon maximum at  $\sim 805$  nm, and (ii) NRs-HSA-IR800, plasmon maximum at  $\sim 804$  nm are shown. Spectra are offset for clarity. (b) Fluorescence (FL) spectra,  $\lambda_{\max} \sim 804$  nm of (i) NSs-HSA-IR800, (ii) NRs-HSA-IR800, and (iii) control sample HSA-IR800 are shown..... 101

**Figure 7-5** Emission spectra of control, HSA-IR800 (black), nanoshells coated with HSA without IR800 (red), and nanorods coated with HSA without IR800 (blue) are shown. Fluorescence is not observed from the nanoparticles without the fluorophore. . 102

**Figure 7-6** Calculated scattering spectra of (i) NSs [ $r_1, r_2$ ] = [63, 78] nm,  $\lambda_{\max} = 805$  nm and (ii) NRs [ $w, l$ ] = [11, 46] nm,  $\lambda_{\max} = 824$  nm. .... 103

**Figure 7-7** (a) Schematic diagram representing angle-resolved fluorescence emission apparatus. M1: Mirror1, M2: Mirror 2, P1: Polarizer, P2: Polarizer,  $\lambda/2$ : Half-wavelength plate, F1: Laser selection filter, F2: Long pass filter, RM: Rotating mount with knob to control the angle of the sample relative to the excitation light (Red circle). Black solid line indicates laser light path. (b) Experimental angle-resolved scattering spectra of NSs (red circles) and NRs (blue circles). Spectra are normalized by concentration of nanoparticles. The radial axis ranges from 0 – 4. .... 104

**Figure 7-8** Frequency domain fluorescence decay of (a) IR800 ( $\tau \sim 564$  ps), (b) HSA-IR800 ( $\tau \sim 427$  ps), (c) NRs-HSA-IR800 ( $\tau \sim 121$  ps), and (d) NSs-HSA-IR800 ( $\tau \sim 68$  ps). The curves referring to phase and modulation are shown with arrows. .... 105

**Figure 8-1** (A) Schematic of the nanoparticle functionalized p<sup>+</sup>n photodiode. Right: Scanning electron micrograph images, indicating representative densities of nanoparticle surface coverage on devices for (B)  $r = 60$  nm silica particles, (C)  $r = 25$  nm Au colloid, and (D) [ $r_1, r_2$ ] = [96, 116] nm nanoshells. .... 116

**Figure 8-2** Measured extinction spectra in aqueous suspension for: (A)  $r = 61$  nm silica nanospheres, (B)  $r = 25$  nm Au nanospheres, (C)  $[r_1, r_2] = [38, 62]$  nm nanoshells, (D)  $[r_1, r_2] = [62, 81]$  nm nanoshells, and (E)  $[r_1, r_2] = [96, 116]$  nm nanoshells. .... 118

**Figure 8-3** Confocal scanning photocurrent apparatus..... 119

**Figure 8-4.** Photocurrent images [in nanoamperes] of (A-D)  $r = 61$  nm silica nanospheres, (E-H)  $r = 25$  nm solid Au nanospheres, (I-L)  $[r_1, r_2] = [38, 62]$  nm nanoshells, and (M-P)  $[r_1, r_2] = [96, 116]$  nm nanoshells for light incident at wavelengths of 532, 633, 785, and 980 nm. Symbols represent single nanoparticles, dimers, and higher order aggregates sampled during each scan. Scale bars are  $2 \mu\text{m}$ ... 122

**Figure 8-5.** Local photocurrent modification for photodiodes functionalized with (A)  $r = 61$  nm silica nanospheres, (B)  $r = 25$  nm solid Au nanospheres, (C)  $[r_1, r_2] = [38, 62]$  nm nanoshells, or (D)  $[r_1, r_2] = [96, 116]$  nm nanoshells. Symbols correspond to particles marked in the rightmost column images of Figure 8-4 (Figure 8-4, panels D, H, L, and P, respectively). Solid lines indicate the trend of the average value. In panel C, the red square pertains to parameters modeled in Figure 8-7A, and the green square corresponds to Figure 8-7B. .... 124

**Figure 8-6.** Photocurrent images [in nanoamperes] of (A-D)  $[r_1, r_2] = [62, 81]$  nm nanoshells for light incident at wavelengths of 532, 633, 785, and 980 nm. (E) Topographic (AFM) image of the same area shown in panels A-D, revealing individual nanoparticle geometry. Scale bars all correspond to  $3 \mu\text{m}$ . Individual nanoshells are highlighted in magenta, nanoshell dimers in green. In panels A-E, the blue inset boxes mark a representative subset of nanoparticles replicated in each image but with varying influence on the photocurrent. (F) Photocurrent modification for isolated nanoshells and (G) dimers of nanoshells. Solid lines represent average trend. Each symbol in panels F and G corresponds to one of the marked particles in panel E. .... 127

**Figure 8-7.** Poynting vector field plots show power flow through a  $[r_1, r_2] = [38, 61]$  nm nanoshell on a Si slab at (A) 633 nm and (B) 980 nm, corresponding to the data points shown in Figure 8-5C enclosed in red and green, respectively. Arrows are normalized for power flow magnitude and indicate direction of power flow. The top and bottom white lines indicate the air-Si interface at  $z = 0$  and at a depth of 500 nm, respectively. These cross sections are in the  $yz$  plane, perpendicular to the incident light polarization. The Poynting vector field is overlaid onto the norm of the vector electric field (indicated by colorbar). .... 128

**Figure 9-1** (A) Schematic illustration of the experiment. Lasers at frequencies  $\omega_1$  and  $\omega_2$  are applied to the nanoshell over film structure, both generating a four wave mixing (FWM) signal at  $2\omega_1 - \omega_2$  and driving the particle into the film. (B) Spectrum of the applied pump and continuum laser fields. Note that the relative amplitude of the continuum has been exaggerated for visibility. (C) Example output FWM spectrum obtained when both the pump and continuum are applied (solid

black) and the background TPPL when only the pump is applied (dotted orange). Two strong peaks in the FWM ( $2\omega_1 - \omega_2$ ) are observed at 671 nm and 710 nm, indicated by green and blue arrows, respectively. The corresponding frequencies in the continuum ( $\omega_2$ ), 978 nm and 906 nm, which mix with the pump ( $\omega_1$ ) at 796 nm to generate these peaks are indicated with the correspondingly colored arrows in (B). The spectral feature at  $\sim 775$  nm is the edge of the short pass filter used to block the excitation light. .... 134

**Figure 9-2** Experimental apparatus used to measure FWM. SP Filter is a combined dielectric and colored glass 785 nm short pass filter, LP Filter is a dielectric 795 nm long pass filter, and  $\lambda/2$ s are half-wave plates. .... 137

**Figure 9-3** Temporal evolution of the normalized FWM signal at  $\omega_{FWM} = 680$  nm for an  $[r_1, r_2] = [90, 104]$  nm nanoshell initially held  $\sim 1$  nm above the surface of a 15 nm thick Au film by a single layer of PDDA. .... 140

**Figure 9-4** Field enhancements for an  $[r_1, r_2] = [90, 104]$  nm Au nanoshell on a 15 nm thick Au film with a gap of (A) +5 nm and (B) -5 nm at 795 nm shown with the same color scale. The behavior of the FWM signal as a function of gap can be obtained by integrating  $|E(\omega_1)|^4 |E(\omega_2)|^2 |E(\omega_{FWM})|^2$  over the region containing the nonlinear material. In this case, the integral is carried out over either the metal (C) or in the air outside the metal (D). Gray lines are a guide to the eye. .... 143

**Figure 9-5** Simulated scattering spectra of an  $[r_1, r_2] = [90, 104]$  nm nanoshell over a 15 nm thick Au film with a varying gap size. The top curve is an  $[r_1, r_2] = [90, 104]$  nm nanoshell in free space. .... 145

**Figure 9-6** Scanning electron micrographs of the nanoshell / PDDA / Au film nanostructures after irradiation. The specific nanostructure measured in Figure 9-3 is shown in (B) with the brightness adjusted to highlight the effect of irradiation on the film and (C) where the brightness has been adjusted to show the nanoshell clearly. A nanoshell that was not irradiated is shown in (D). .... 146

**Figure 9-7** Temporal evolution of the normalized FWM signal at 680 nm, corresponding to the pump at 795 nm mixing with 957 nm light from the continuum, for (A) nanoshells deposited directly on the Au film and (B) nanoshells on top of a PDDA / [PSS / PDDA]<sub>2</sub> multilayer film. .... 148

## List of Tables

<b>Table 7-1</b> Multiexponential analysis of intensity decay of IR800 with nanoparticles showing molecular fraction ( $\alpha$ ), observed lifetime ( $\tau_i$ , ns), amplitude weighted lifetime ( $\langle\tau\rangle$ , ns), and goodness of fit parameter ( $\chi^2_R$ ).....	109
<b>Table 7-2</b> Quantum yield (Q.Y.), radiative decay rate ( $\Gamma$ ) and nonradiative decay rate ( $k_{nr}$ ) of IR800, HSA-IR800 and HSA-IR800 with nanoparticles.....	111

## Chapter 1. Introduction

Metallic nanostructures are one of the most versatile tools available for manipulating light at the nanoscale.<sup>1-10</sup> These nanostructures support surface plasmons, which are collective excitations of the conduction electrons that can exist as propagating waves at a metallic interface or as localized excitations of a nanoparticle or nanostructure. Plasmonic structures can efficiently couple energy from freely propagating electromagnetic waves to localized electromagnetic fields and vice-versa, essentially acting as optical antennas.<sup>6, 9,</sup>

<sup>11</sup> This subwavelength focusing of light into nanoscale volumes results in a dramatic enhancement of the local fields around and inside the nanostructure are strongly enhanced compared to the incident radiation.

In this thesis, the basic parameters allowing manipulation of the near and far field electromagnetic response of plasmonic structures are investigated; the near field is profiled Raman-based molecular rulers; plasmonic nanoparticles are used as nanoantennas to control the coupling of light into and out of organic fluorophores and modify the photocurrent generated in a silicon photodiode; and the intense focusing of light into nanoscale volumes is exploited for nonlinear optic and optically-driven physical manipulation.

These studies are performed using structures based on metallic nanoshells, which consist of a thin Au shell coating a silica nanosphere. The plasmon resonances of this structure arise from the hybridization of a sphere and a cavity primitive plasmon. Controlling the interaction of these plasmons allows the nanoshell plasmons to be tuned across the visible and near-infrared. To further investigate the parameters controlling the plasmonic

response of metallic nanoshells, two changes to the nanoshell composition are studied: (1) the Au shell is replaced with Cu which has interband transitions that strongly influence the plasmon resonance,<sup>12-14</sup> and (2) the silica core is replaced by a semiconducting  $\text{Cu}_2\text{O}$  core which has a significantly higher dielectric constant and non-trivial absorbance. Due to the spherical symmetry, the exact electromagnetic response in the near and far field is readily evaluated using Mie theory.<sup>15-18</sup> The focusing of electromagnetic energy into intense local fields by plasmonic nanostructures is then directly investigated by profiling the nanoshell near field using a Raman-based molecular ruler.<sup>19</sup>

Plasmons supported by Au nanoshells are can be used as optical antennas to control the coupling of light between far-field radiation and localized excitations.<sup>6, 9, 11</sup> This is used to dramatically enhance the fluorescence of near-infrared fluorophores placed at controlled distances from the nanoshell surface.<sup>20</sup> In this context, the analogy of an optical antenna is very relevant: the enhanced field at the surface of the nanoshell increases the absorption of light by the fluorophore, or equivalently couples propagating electromagnetic waves into a localized receiver. The large scattering cross section then enhances the coupling of energy from this localized source, the excited fluorophore, to far-field radiation. Excellent agreement is obtained with models based on Mie, elucidating the mechanisms responsible for this enhancement. Analogous to the Purcell effect in cavities and waveguides, emission from an adjacent excited atom, molecule, or semiconductor can decay directly into a resonant plasmon, modifying the available photon density of states and changing its radiative decay rate.<sup>4, 6, 11, 21</sup> This directly results in a dramatic decrease in the lifetime of the excited state. Experimentally, the radiative

decay rate for fluorophores on Au nanoshells and Au nanorods are measured.<sup>22</sup> These results are also found to be consistent with this model.

Plasmonic nanostructures can also control the flow of light into larger structures. This is observed by measuring the nanoparticle-induced enhancement and suppression of photocurrent in a silicon photodiode is at the single particle level for silica nanospheres, Au nanospheres, and two types of Au nanoshell.<sup>23</sup>

Finally, the simultaneous physical manipulation of an individual plasmonic nanostructure on the few-nanometer scale using light and detection of the local electromagnetic field during this ongoing process with the same incident beam is performed.<sup>24</sup> The intense fields arising from the sub-wavelength focusing of light by plasmonic structures is critical to this process. For this experiment, a Au nanoshell is separated from a metallic surface by a few-nanometer thick polymer layer to form a nanoscale junction, or nanogap. Illuminating this structure with ultrashort optical pulses, exciting the plasmon resonance, results in a continuous, monitorable collapse of the nanogap. An easily detectable four-wave mixing (FWM) signal is simultaneously generated by this illumination of the nanogap, providing a continuous, highly sensitive optical monitor of the nanogap spacing while it is being optically reduced. This signal increases dramatically upon contact providing a clear, unambiguous signal of the gap closing.

## Chapter 2. Electromagnetic properties of nanoparticles

### 2.1 Plasmon hybridization

Plasmon hybridization is a powerful analytical tool for obtaining intuitive understanding of the plasmon resonances in complex structures. In this model, the plasmons supported by complex structures are built up from the interactions of simple structures. The modes of the complex structure are expressed as linear combinations of the primitive plasmon modes associated with each metallic surface in the structure.

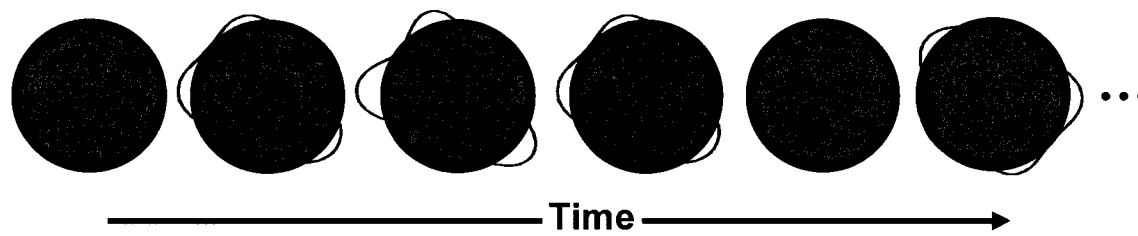


**Figure 2-1** Incompressible fluid model for oscillating plasmons in a solid metallic sphere. The metal (green) is composed of a fixed ion background (blue) and an oscillating electron fluid (yellow).

In the plasmon hybridization model, the metal is treated as an irrotational, incompressible electron fluid of uniform density constrained by a fixed positive background due to the ion cores. Deformation of this fluid result in spill-out of the electrons at the surface of the nanoparticle as illustrated in Figure 2-1. This deformation can be expressed as the gradient of a scalar potential which satisfies the Laplace equation. Coulomb interaction with the fixed ion cores results in a strong restoring force acting against any deformation of the electron cloud. This scalar potential can be expanded in a complete basis set of primitive plasmons in geometries where the Laplace equation is separable. The Lagrangian describing the dynamics of this system is then composed of the kinetic energy due to motion of the electron liquid and the potential energy arising

from the instantaneous Coulomb interactions. While the primitive plasmon modes are associated with a particular interface of a metallic structure, it will result in a secondary surface charge distribution on all other surfaces of the same metallic object due to the incompressible nature of the electron fluid.

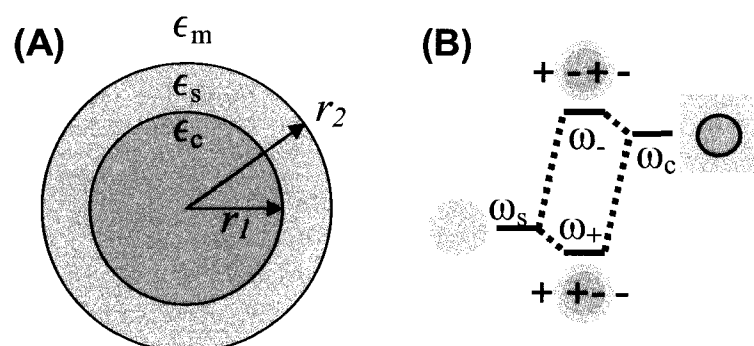


**Figure 2-2** (A) Schematic diagram of a nanoshell. (B) Hybridization diagram for a Au shell - SiO<sub>2</sub> core nanoshell.

The tunable plasmon resonances supported by metallic nanoshells, which consist of a dielectric core of radius  $r_1$  and a thin metal shell with an outer radius  $r_2$  as illustrated in (A), can be easily described using the plasmon hybridization model. In this structure, the nanoshell plasmons are linear combinations of sphere and hollow spherical cavity plasmons, each of which can be written as a sum of spherical multipoles of order  $l$ . Due to the spherical symmetry, only cavity and sphere plasmons of the same order  $l$  interact. The resulting nanoshell plasmons then consist of a low energy symmetric, or antibonding, combination of a sphere and cavity plasmon of order  $l$  ( $\omega_+$ ), and a symmetric (bonding) plasmon ( $\omega_-$ ) at higher energy. Intuitively, one might expect the symmetric plasmon mode to be the high energy mode as dipoles in the same orientation should repel each other. Indeed, the primary charge surface charge associated with the sphere plasmon on the outer surface of the nanoshell and the cavity plasmon on the inner surface do repel

each for the symmetric mode and attract for the antisymmetric. Due to the incompressible nature of the electron fluid, adding electrons to one surface of the nanoshell requires removing electrons from the other. The sphere primitive plasmon therefore induces a secondary surface charge on the inner surface of the nanoshell of opposite sign to the primary charge induced on the outer surface and the cavity plasmon likewise induces a charge on the outer surface. The interaction of the primary and secondary charge on each surface is therefore opposite that of the primary charges. Since this occurs on both surfaces, the total effect is twice as strong as the interaction of the primary charges. As a result, the symmetric combination of sphere and cavity plasmon is at a lower energy than the antisymmetric combination.

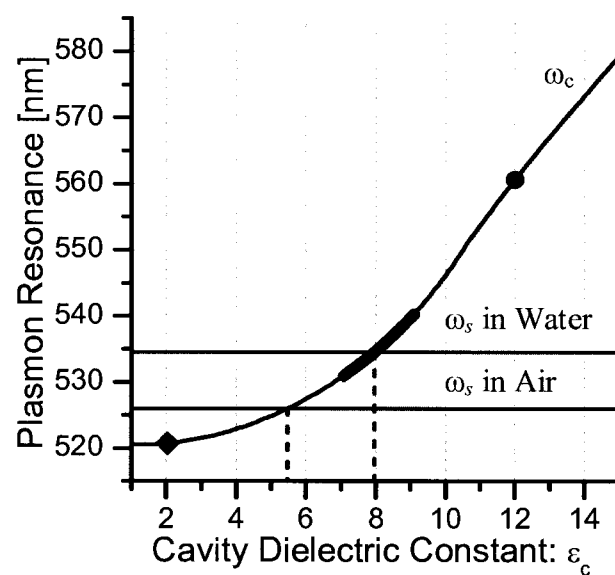


**Figure 2-3** Horizontal lines: dipole plasmon resonance for a Au sphere immersed in air ( $\epsilon_m = 1.00$ ) or H<sub>2</sub>O ( $\epsilon_m = 1.77$ ). Blue curve: dipole plasmon resonance for a spherical cavity in Au ( $\omega_s$ ) as a function of the dielectric constant ( $\epsilon_c$ ) of the material inside the cavity. Points corresponding to a silica core ( $\epsilon_c = 2.04$ ,  $\blacklozenge$ ), a Cu<sub>2</sub>O core ( $\epsilon_c \approx 7.1$  to  $9.1$ ,  $\text{—}$ ), and an iron oxide core ( $\epsilon_c \approx 12$ ,  $\bullet$ ) are indicated in black along the cavity plasmon line.

The splitting of the nanoshell plasmons is determined by the strength of the interaction of the primitive plasmons, which is controlled by the spatial and energetic overlap. Reducing the relative shell thickness, specifically the aspect ratio  $r_1/r_2$ , increases the strength of this interaction, resulting in a red-shift of the low energy ( $\omega_-$ ) plasmon and a blue-shift of the high energy ( $\omega_+$ ) plasmon. This allows the nanoshell plasmon to be tuned across the visible and near-infrared by simply adjusting the inner and outer radius. For a finite sized nanoshell, phase retardation effects will contribute an additional shift of the plasmons to lower energy as the nanoshell increases in size. The energy of the sphere plasmon and cavity plasmon are controlled by the adjacent dielectric. Increasing the dielectric of the embedding medium shifts the sphere plasmon to a lower energy and increasing the core dielectric shifts the cavity plasmon to a lower energy. This effect is shown quantitatively in Figure 2-3. Here, the dipole plasmon resonance for a spherical cavity in Au ( $\omega_s$ ) as a function of the dielectric constant ( $\epsilon_c$ ) of the material inside the cavity is shown as a solid blue line. Three core materials upon which Au nanoshells have experimentally been fabricated<sup>25-27</sup> are indicated along this curve in black: silica core ( $\epsilon_c = 2.04$ ), a  $\text{Cu}_2\text{O}$  core ( $\epsilon_c \approx 7.1$  to  $9.1$ ), and an iron oxide core ( $\epsilon_c \approx 12$ ). The energy of the sphere plasmon ( $\omega_s$ ) embedded in air ( $\epsilon_m = 1.00$ ) and water ( $\epsilon_m = 1.77$ ) are indicated as horizontal lines in Figure 2-3. The sphere and cavity plasmon energies will be equal for a nanoshell embedded in air with a core dielectric  $\epsilon_c = 5.48$ , and for a nanoshell immersed in water with a core dielectric of  $\epsilon_c = 8.0$ .

For the typical case of a Au coated silica nanoshell, shown schematically in Figure 2-2(B), the sphere plasmon ( $\omega_s$ ) is at a lower energy than the cavity plasmon ( $\omega_c$ ). The resulting low energy symmetric ( $\omega_+$ ) nanoshell plasmon is therefore dominated by the

sphere mode while the high energy antisymmetric ( $\omega_+$ ) plasmon is dominated by the cavity mode. Because the plasmon modes supported by a cavity with no dielectric filler have no net dipole moment, the total dipole moment of the nanoshell plasmon is proportional to the square of the admixture of the sphere plasmon. In the case of a Au-SiO<sub>2</sub> nanoshell, the low energy sphere-dominated plasmon therefore has a large overall dipole moment, while the high energy cavity-dominated plasmon has a vanishing dipole moment. We refer to the low energy plasmon as “bright” and the high energy plasmon as “dark” because only the low energy plasmon interacts strongly with light.

## 2.2 Mie theory

While plasmon hybridization excels at providing intuitive pictures to understand the plasmon resonances in complex structures, quantitative comparison with experimental results requires modeling techniques that account for phase retardation and arbitrary dielectric functions. For spherically symmetric particles, such as solid spheres or concentric nanoshells, Mie theory provides an exact quasi-analytic solution to the electromagnetic scattering problem in the frequency domain.<sup>18, 28, 29</sup> Following the approach of Aden and Kerker,<sup>15, 29</sup> the vector spherical harmonics are used as a basis set to express the incident plane wave, the electromagnetic fields in the core and shell, and the scattered field outside the nanoshell. Imposing continuity of the tangential  $\mathbf{E}$  and  $\mathbf{H}$  fields at the interfaces yields a straightforward eigenvalue problem for the expansion, or Mie, coefficients for each multipolar order  $n$ . Using these Mie coefficients, the electromagnetic fields anywhere in space can then be evaluated. The far field extinction and scattering coefficients are then obtained by integrating the energy flow across the boundary of an imaginary sphere concentric with the nanoparticle. These integrals can be

carried out analytically to obtain simple expressions for the far field cross sections for each multipolar order  $n$  in terms of the Mie coefficients. As a result, the far field cross sections can be evaluated very quickly for a spherically symmetric particle.

### **2.3 Surface-enhanced Raman scattering**

When a photon interacts with a molecule, where the photon energy does correspond to an accessible electronic state, three processes can occur. The molecule can be excited to a virtual electronic state, then immediately relax back to the initial state emitting a photon of exactly the same energy as the incident photon. This process is referred to as Rayleigh scattering. Raman scattering is the inelastic scattering of a photon by the molecule, where energy is transfer between the molecule and the photon, leaving the molecule in a different vibration state, as illustrated in Figure 2-4. If the molecule starts in the ground state, the photon will loose energy leaving the molecule in an excited vibration state. This is referred to as the Stokes process. If the molecule starts in an excited vibration state, the photon will gain energy, leaving the molecule in the ground state. The difference between the incident photon and the scattered photon is then always equal to the energy of the vibration level. The spectrum of the scattered photons therefore corresponds to the energies of the vibrational states of the molecule. Raman scattering is inherently a weak process: for a typical organic molecule, perhaps 1 in  $10^{10}$  photons will undergo a Stokes scattering process while the anti-Stokes process is even less likely.

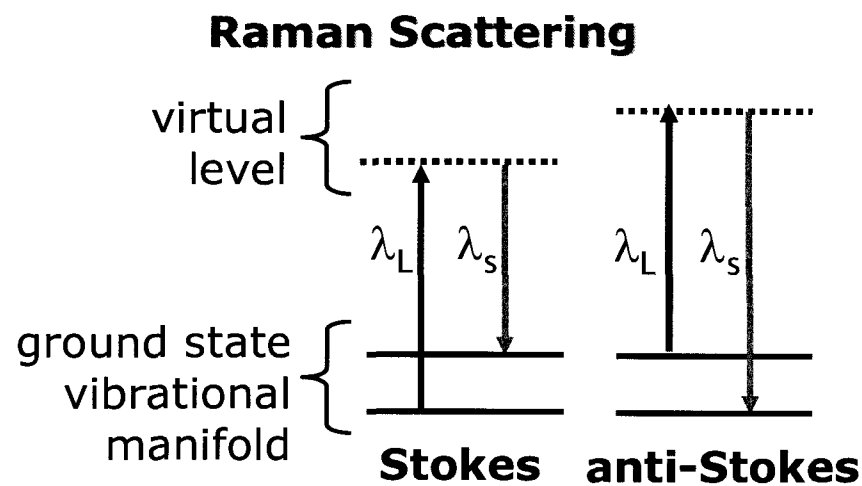


**Figure 2-4** Energy level diagram for Raman scattering.

In the presence of a plasmonic nanostructure, the Raman scattering signal can be enhanced significantly. Both the absorption and emission are enhanced. At the excitation laser frequency  $\omega_L$ , the molecule experiences both the incident laser field  $E_{incident}(\omega_L)$  and the enhanced local field from the nanostructure ( $E_{NS}(\omega_L)$ ). By reciprocity, the nanostructure will also enhance the radiation from the molecule at the Raman shifted frequency  $\omega_S$ . The average enhancement for a molecule on the structure is then

$$G_{SERS} = \left\langle \left| E_{incident}(\omega_L) + E_{NS}(\omega_L) \right|^2 \left| E_{NS}(\omega_S) \right|^2 \right\rangle, \quad (2-1)$$

where the average is over the nanoparticle surface. When considering the enhancement, it is important to keep the actual experiment in mind. The measured signal will be proportional to the average enhancement only in an experiment where one molecule is placed randomly on the surface. For experiments where the nanoparticle is coated in molecules, the total signal will be proportional to the surface integral of the enhancement. This quantity may be quite different from the surface average or spatially maximum enhancement! For example, quite different conclusions may be drawn from calculations

comparing a structure where the field is confined to a small junction to a larger structure with a more modest field enhancement over a larger area if the maximum, average, or integrated enhancement is taken.<sup>30</sup>

#### 2.4 Fluorescence Enhancement by Plasmonic Nanoantennas

Fluorescence is the radiative decay of an electronic excitation in a molecule. In contrast to Raman scattering, this involves a real excitation of the molecule to an excited electronic state rather than scattering nearly instantaneously off a virtual state. When a sample of molecules with absorptivity  $\epsilon$  is excited with light of intensity  $I_{exc}$ , the total amount of energy absorbed is simply  $I_{exc} \cdot \epsilon$ . The quantum yield determines what portion of this energy is reemitted as fluorescence; therefore, the observed emission intensity is  $I_o = I_{exc} \cdot \epsilon \cdot Q_o$ . Intrinsically, this process is best described in terms of the radiative emission rate ( $\Gamma$ ) and non-radiative decay rate ( $k_{nr}$ ). The quantum yield  $Q_o = \Gamma / (\Gamma + k_{nr})$  is then the relative likelihood that the excited molecule relaxes follow a radiative decay pathway, while the observed lifetime is simply the inverse of the total decay rate of the excited state  $\tau_0 = (\Gamma + k_{nr})^{-1}$ .

In the presence of a plasmonic nanostructure, the enhanced local field will increase the amount of light absorbed by the molecule. The surface average of the near field intensity enhancement,  $\langle |\mathbf{E}|^2 \rangle$ , can be calculated directly using Mie theory for Au nanoshells, leading to a fluorescence emission of  $(\langle |\mathbf{E}|^2 \rangle \cdot I_{exc}) \cdot \epsilon \cdot Q_o$ . However, this is only half of the process. Electromagnetic coupling between the fluorophore and the plasmons at the emission wavelength increases the radiative decay rate of the molecule by a factor  $\gamma_r$ , resulting in an effective radiative decay rate ( $\gamma_r \cdot \Gamma$ ). For nanoshells, this can also be

evaluated using Mie theory following the method in Gibson et al.<sup>31</sup> This results in a decrease in lifetime  $\tau_{NS} = (\gamma_r\Gamma + k_{nr})^{-1}$  and an increase in quantum yield  $Q_{NS} = \gamma_r\Gamma / (\gamma_r\Gamma + k_{nr})$ . Assuming that  $k_{nr}$  is unaffected by the presence of the nanostructure, the emission of the molecule-nanostructure complex is  $I_{NS} = \langle |\mathbf{E}|^2 \rangle I_{exc} \cdot \epsilon \cdot Q_{NS}$ . The enhancement is then the emission in the presence of the nanostructure ( $I_{NS}$ ) relative to the emission from the unenhanced dye under the same conditions ( $I_0$ ):

$$\frac{I_{NS}}{I_0} = \langle |\mathbf{E}|^2 \rangle \frac{Q_{NS}}{Q_o} = \langle |\mathbf{E}|^2 \rangle \frac{\chi_r(\Gamma + k_{nr})}{\chi_r\Gamma + k_{nr}}. \quad 2-2$$

From this expression, one can see that the observed enhancement can be separated into the effect of the field enhancement ( $\langle |\mathbf{E}|^2 \rangle$ ) and the quantum yield enhancement ( $Q_{NS}/Q_o$ ). This expression indicates that fluorescence enhancement depends on the properties of the nanostructure, and also the molecule via  $\Gamma$  and  $k_{nr}$ .

### **Chapter 3. Cu nanoshells: effects of interband transitions on the nanoparticle plasmon resonance**

While the focus of this thesis is on the plasmonic response of metallic nanostructures, the optical properties of metals arise from both the optical excitation of interband transitions and the free-electron response. In this chapter, we examine the optical properties of Cu, whose strong interband transitions dominate its optical response in the visible region of the spectrum. Spectral overlap of the interband transitions in Cu with the nanoshell plasmon resonance results in a striking double-peaked plasmon resonance. For this work, I performed the theoretical analysis and Hui Wang experimentally fabricated the Cu nanoshells. Reprinted from Hui Wang, Felicia Tam, Nathaniel K. Grady, and Naomi J. Halas, "Cu Nanoshells: Effects of Interband Transitions on the Nanoparticle Plasmon Resonance," *Journal of Physical Chemistry B* **109**(39), 18218-18222 (2005). Copyright 2005 American Chemical Society.

Metallic nanostructures are attracting an increasing interest as an important class of photonic components that control and manipulate light at the nanometer scale.<sup>1-3, 32</sup> The interaction of light with electrons in metallic nanostructures can give rise to collective excitations known as plasmon resonances. Plasmonic excitations provide a means to focus light to subwavelength dimensions, making it possible to overcome the optical diffraction limit and enabling the design of nanoscale optical devices, such as waveguides.<sup>2, 5</sup> The intense local electromagnetic fields of metallic nanostructures at their plasmon resonant energies can also be exploited for surface enhanced spectroscopies.<sup>33-35</sup> Recent advances in size- and shape-controlled fabrication of metallic nanostructures,<sup>36</sup> along with the development of highly efficient theoretical methods for calculating their

electromagnetic properties,<sup>3,37,38</sup> provide a foundation for advancing the development of metal-based nanophotonic components and devices, an emerging area known as plasmonics.

Coinage metals such as Au and Ag have been of particular interest for plasmonics because they can support nanoparticle plasmon resonances in the ultraviolet, visible and near infrared regions of the spectrum, modified by varying nanoparticle size and shape. Metallic nanoshells, spherical nanoparticles composed of a dielectric core and a concentric metal shell, are nanoparticles whose plasmon resonant energies are particularly sensitive to geometry.<sup>17</sup> In striking contrast to solid metallic nanostructures such as nanosphere or nanorods, which exhibit relatively weak plasmonic tunability dependent on size or aspect ratio, nanoshells exhibit plasmon resonances that are quite critically dependent on inner and outer shell dimensions. This tunability has its origins in the hybridization of the two fixed-frequency plasmon modes supported by the inner cavity and outer surface of the nanoshell.<sup>39</sup> In applications, plasmon resonant energies of nanoshells have been tuned to the near infrared “water window” where tissue and blood are transparent, enabling a range of nanobiomedical innovations.<sup>40,41-43</sup> The plasmon resonant energy of the nanoshell geometry can be extended into the far infrared through plasmon hybridization of one nanoshell encapsulated within another nanoshell, also known as a “nanomatryushka” geometry.<sup>39,44</sup> Because of their high degree of symmetry, many nanoshell properties can be calculated straightforwardly using Mie scattering theory.<sup>15, 45</sup> The agreement between experimental measurements and Mie theory predictions of the plasmon resonant properties of Au nanoshells has been further confirmed quantitatively at the single nanoparticle level.<sup>46</sup>

In addition to nanoparticle geometry, the optical properties of plasmonic nanoparticles can also be strongly influenced by the electronic structure of the constituent metal, which determines the metal's dielectric function.<sup>28, 47</sup> To better understand the role that the metal plays in determining the optical properties of metallic nanoparticles it is necessary to examine and account for the effects of both the free electron and electronic interband transition contributions to the metal's dielectric response.<sup>12</sup> At energies well below their plasmon resonance, Au and Ag nanoparticles can be treated as free-electron systems whose optical properties are determined by the conduction electrons, with only a constant real background polarizability associated with the core electrons. Here we theoretically and experimentally examine the contrasting case of Cu nanoparticles, where the effects of strong interband transitions near the same energies as the plasmon response of the solid metallic nanoparticle can be examined. Geometric control of the plasmon resonant energies in the nanoshell geometry enables selective tuning of plasmon mode energies with respect to the onset of the Cu interband transitions. By varying nanoparticle geometry, we examine how the electronic properties of the metal, through the interband transitions, modify the plasmon resonances of the constituent nanoparticle.

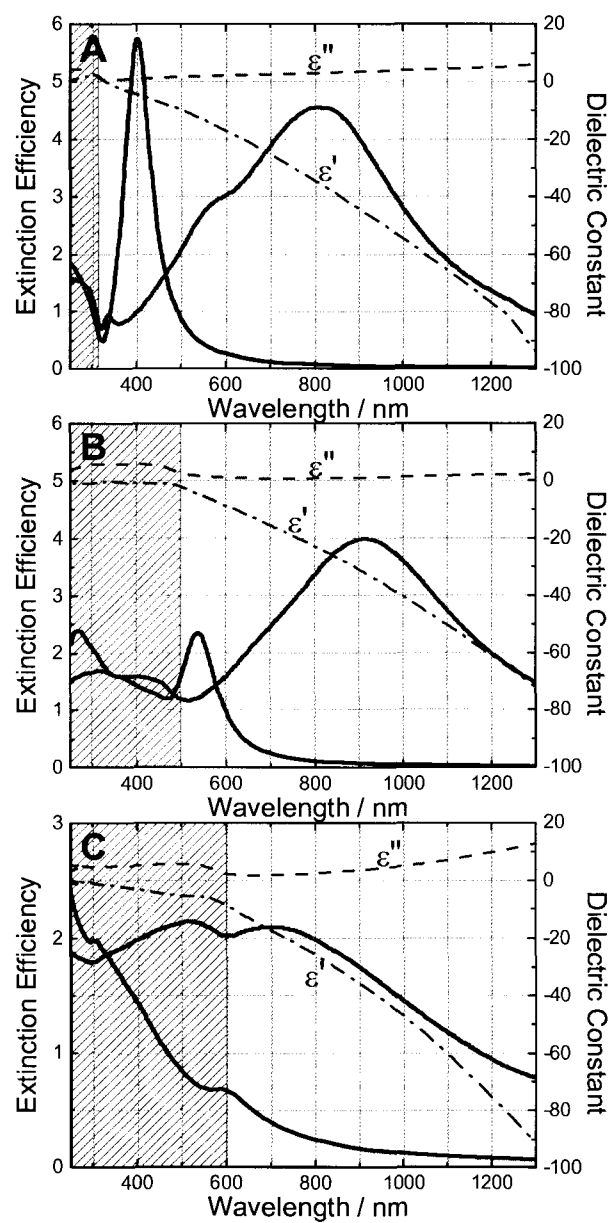


**Figure 3-1** Theoretically calculated far field extinction of a solid nanosphere (black solid curves) and nanoshell (blue solid curves) made of (A) Ag, (B) Au, and (C) Cu. The nanospheres are 20 nm in radius and the nanoshells are 63 nm in core (silica) radius and 10 nm in shell thickness. The refractive index of ethanol ( $n = 1.36$ ) is used as the refractive index of the medium surrounding the particles. Dielectric function (red curves) of (A) Ag, (B) Au, and (C) Cu are also shown.  $\epsilon'$  and  $\epsilon''$  are the real and imaginary parts of the dielectric constants, respectively. The green shaded areas indicate the wavelength regions where interband transitions of the metals occur.

Figure 3-1 shows a comparison of the theoretical extinction spectra of Au, Ag, and Cu solid nanospheres and nanoshells, obtained using Mie scattering theory incorporating the

experimentally obtained dielectric function for Ag, Au, and Cu<sup>48</sup> and standard finite path length corrections.<sup>28, 49</sup> The surrounding dielectric medium was ethanol ( $n = 1.36$ ). The calculated extinction is expressed as an efficiency, which is the ratio of the energy scattered or absorbed by the nanoparticle to the energy incident on its physical cross section. The spectral regions where interband transitions occur are shaded in green. The onset of electronic interband transitions from the valence band to the Fermi level causes a sharp increase in the imaginary part ( $\epsilon''$ ) and a marked change in the slope of the real part ( $\epsilon'$ ) of the dielectric functions. For solid nanospheres 20 nm in radius, the relative spectral locations of the particle plasmon resonance and the constituent metal's interband transitions determine the nanoparticles' optical response, resulting in significant variations between Au, Ag, and Cu nanospheres. The Ag nanosphere has by far the strongest plasmon resonance because the higher energy of the interband transitions ( $\sim 3.8$  eV),<sup>14, 50</sup> relative to the energy of the plasmon resonance leads to minimal damping of the plasmon. In Ag, the onset of interband transitions is visible in the experimental extinction spectrum only as a small increase in absorption starting at approximately 330 nm. The Au nanosphere displays a well-defined plasmon resonance at 530 nm, which is very close to the edge of the interband transitions region ( $\sim 2.5$  eV).<sup>14, 50</sup> The Cu nanosphere has by far the weakest comparative optical response due to the nanosphere plasmon being resonant with the interband transition region ( $\sim 2.1$  eV)<sup>14, 50, 51</sup> of the spectrum. The interband transitions are responsible for a strong damping of the Cu nanosphere plasmon and the strong "background" absorption on top of which a weak plasmon resonance peak is visible.

The tunability of nanoshell plasmons allows the design of nanoparticles with surface plasmon resonances shifted away from the constituent metal's interband transitions. A direct comparison of theoretical extinction spectra for nanoshells composed of a silica core and Ag, Au, and Cu shell layers is also shown in Figure 3-1. All nanoshell calculations were performed with the same inner and outer shell radii  $[r_1, r_2] = [63, 73]$  nm. All nanoshell spectra exhibit dipole plasmon resonances that have been shifted to longer wavelengths relative to those of the corresponding solid nanosphere. The plasmon resonance spectra of the Ag and Au nanoshells in Figure 3-1A and B are relatively similar to each other in amplitude and peak wavelength, a comparison that has been previously noted.<sup>52</sup> The Ag nanoshell resonance also shows an additional, weaker feature at nominally 560 nm attributable to excitation of the nanostructure's quadrupole mode. In marked contrast, the plasmon resonance of a Cu nanoshell of the same size and aspect ratio remains centered at wavelengths corresponding to the onset of interband transitions in Cu (Figure 3-1C). In addition, a dip in the resonance spectrum also appears at this onset energy, resulting in a unique double-peaked resonance lineshape.

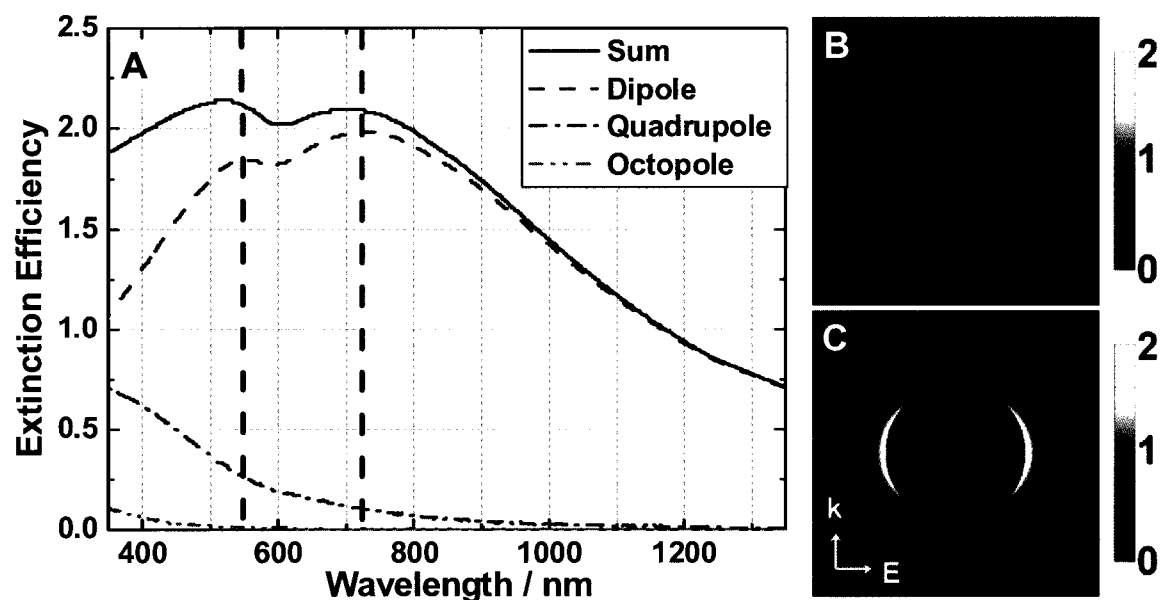


**Figure 3-2** (A) Theoretically calculated far-field extinction of a Cu nanoshell with core radius of 63 nm and shell thickness of 10 nm. Near-field patterns of the dipole resonance excited at (B) 550 nm and (C) 720 nm. The polarization ( $E$ ) and propagation ( $k$ ) vectors are indicated in (C).

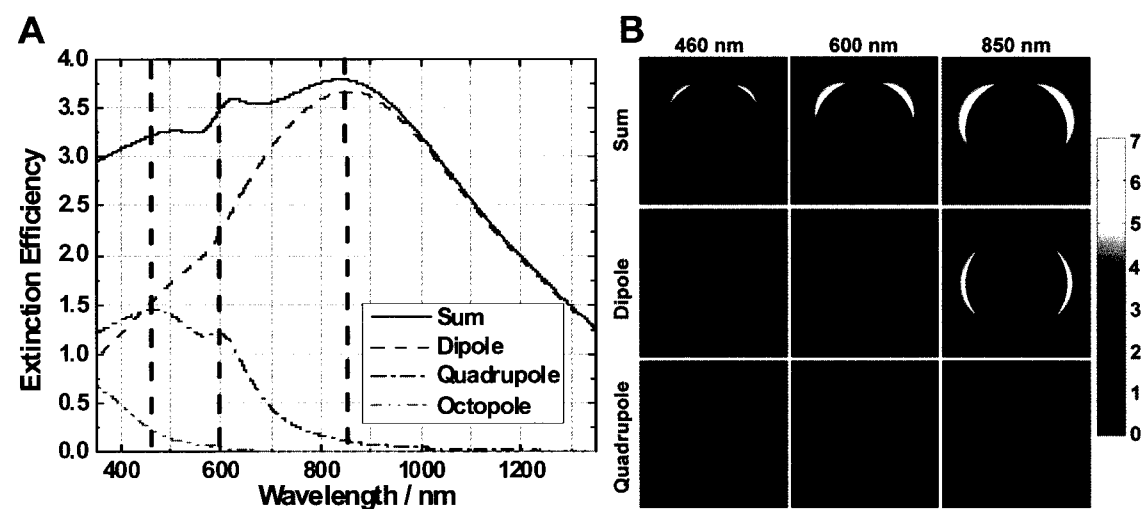


**Figure 3-3** (A) Theoretically calculated far-field extinction of a Cu nanoshell with core radius of 63 nm and shell thickness of 40 nm. (B) Near-field pattern in the plane containing the polarization and propagation vectors as indicated in the Figure 3-2. The color bars indicate the magnitude of the  $|E|^2$ . The columns indicate the excitation wavelengths. The first row includes the first 5 terms in the Mie expansion, the second row contains only the first (dipole) term, and the third row only includes the second (quadrupole) term.

In Figure 3-2 the Cu nanoshell resonance lineshape is analyzed in greater detail. In Figure 3-2A, the total calculated far-field extinction spectrum is analyzed to show the individual dipole, quadrupole, and octopole contributions to the overall spectral response of the nanostructure. The overall extinction is dominated by the dipole plasmon mode, whose lineshape has been strongly modified into this double peaked structure. This analysis clearly shows that the origin of this doubly peaked feature is related to variations in the dielectric function of Cu, and not due to the onset of a quadrupole mode (such as the high energy feature at ~550 nm in the Ag nanoshell response in Figure 3-1A). As illustrated in Figure 3-2B and C, the near-field contours of the plasmon resonance excited at 550 nm and 720 nm, wavelengths corresponding to the two maxima of this resonance, further confirm the dipolar nature of each spectral feature. As the thickness of the Cu nanoshell layer is increased, the quadrupole plasmon mode can be brought into resonance with the interband transitions in Cu. The peak of the dipole resonance is shifted to ~ 850 nm, and the quadrupole and other higher order multiple modes become increasingly pronounced compared to the dipole resonance, due to increasing phase retardation effects.<sup>53-55</sup> In this case, the peculiar peak “inflection” is transferred to the quadrupole plasmon mode (Figure 3-3A). Figure 3-3A analyzes the calculated extinction spectrum of a (63, 103) Cu nanoshell. Here, both the dipole and quadrupole modes contribute significantly to the overall extinction. A double-peaked quadrupole lineshape is now observed as the quadrupole resonance overlaps with the onset of the interband transitions. The quadrupole maximum at 460 nm is more intense than that at 600 nm probably due to the overlap of quadrupole plasmon and the spectral “background” arising from the interband transitions. Figure 3-3B shows the calculated near-field contours of the dipole and

quadrupole plasmon modes excited at the wavelengths associated with these inflections, as indicated in Figure 3-3A. The top row in Figure 3-3B corresponds to the total plasmon extinction in the near field at these three wavelengths of interest, which in this case consists of the sum of the first 5 multipolar terms in the Mie expansion. The asymmetry of the total near field profile is simply due to the relative phase of the various multipolar modes. The second row shows the relative dipole mode intensities in the near field at the three wavelengths of interest, and the third row shows the quadrupole mode. The near field patterns confirm the quadrupolar nature of both spectral features at 460 and at 600 nm for this size and geometry of nanoparticle.

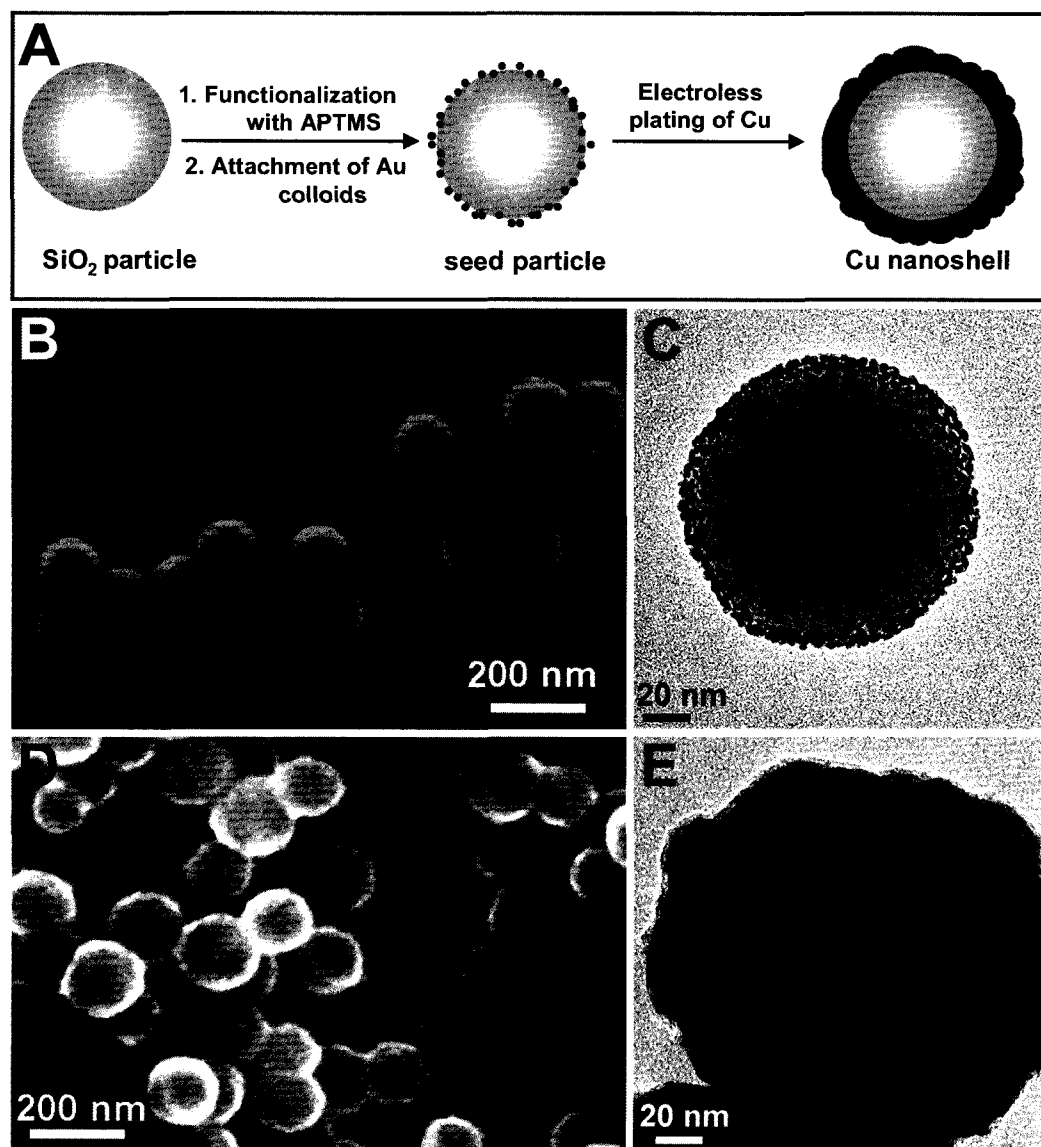


**Figure 3-4** (A) Illustration of the fabrication of Cu nanoshells. SEM (B) and TEM (C) images of the seed particles. SEM (D) and TEM (E) images of Cu nanoshells (63 + 8 nm core radius and 30 + 4 nm shell thickness).

To experimentally investigate the effects of interband transitions on the plasmons, we use a wet chemistry method to fabricate Cu nanoshells with controllable core-shell dimensions. Currently, the most extensively used strategy for nanoshell fabrication involves the seed-mediated electroless plating. By using this method, continuous Au,<sup>17, 56-58</sup> Ag,<sup>52, 59, 60</sup> and even bimetallic nanoshells<sup>61</sup> with controllable core and shell dimensions

have been successfully fabricated using silica or polymer beads as core materials. In addition to the seeded shell growth, more recent approaches based on galvanic replacement reactions<sup>62-64</sup> have also been employed to produce hollow metallic nanoshells using metal nanoparticles as sacrificial cores. Here we exploit a combination of surface seeding and electroless plating methods to fabricate Cu nanoshells using silica nanosphere cores (Figure 3-4). As illustrated in Figure 3-4A, the fabrication of Cu nanoshells involves two major steps. The first step is analogous to the pretreatment step in electroless plating, in which small Au nanoparticles (~2 nm in diameter) are immobilized onto the surface of (3-aminopropyl) trimethoxysilane (APTMS) functionalized silica particles. As illustrated in Figure 3-4C, the coverage of Au nanoparticles on the surface of the silica beads is nominally 30%. In the second step, the immobilized Au colloid act as nucleation sites for electroless Cu plating onto the surface of silica particles, leading to the gradual formation of continuous and complete Cu nanoshells (Figure 3-4D and F). The as-prepared Cu nanoshells can be homogeneously dispersed in ethanol to form colloidal solutions. X-ray powder diffraction results (Supporting Information) indicate the absence of oxide layers on the surface of the as-prepared Cu nanoshells during and after the shell growth.

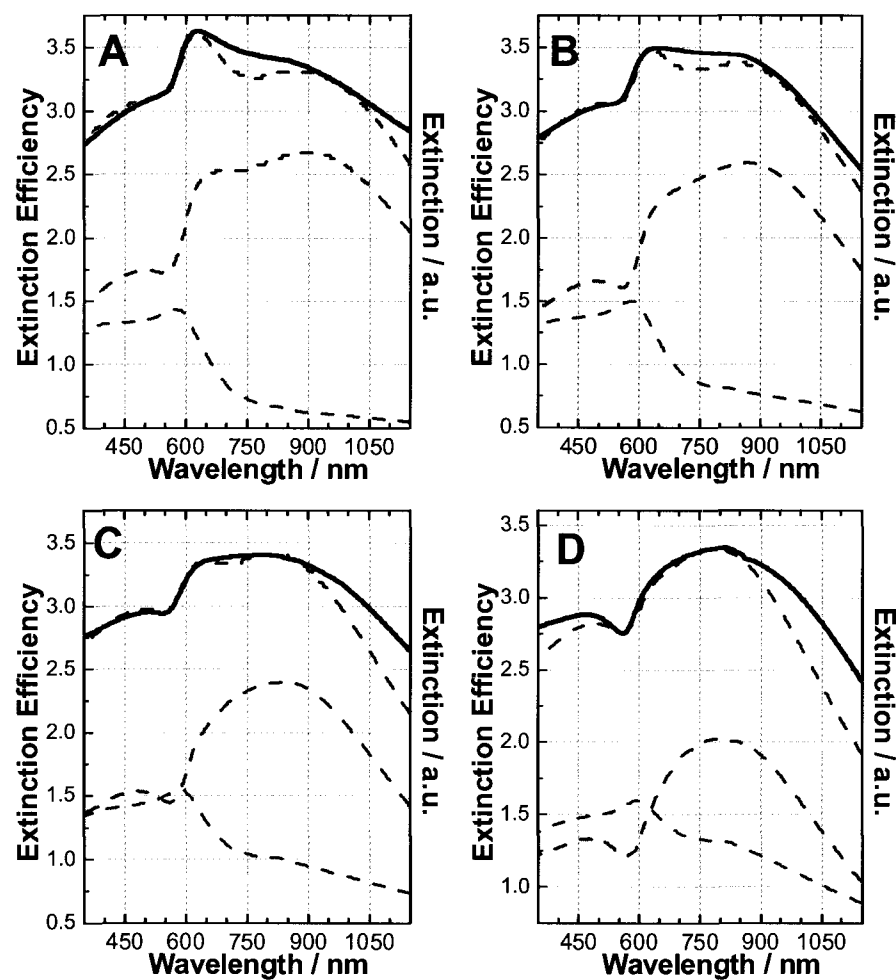


**Figure 3-5** Extinction spectra of Cu nanoshells with core radius of  $63 \pm 8$  nm and shell thickness of (A)  $52 \pm 7$  nm, (B)  $45 \pm 6$  nm, (C)  $38 \pm 5$  nm, and (D)  $30 \pm 4$  nm. The solid curves are the experimentally measured extinction spectra of Cu nanoshells dispersed in ethanol. The dash curves are the theoretically calculated extinction (red), absorption (green), and scattering (blue) of the Cu nanoshells.

Figure 3-5 shows the extinction spectra of experimentally fabricated Cu nanoshells with core radius of  $63 \pm 8$  nm and several varying shell thicknesses. The core-shell dimensions of the Cu nanoshells are determined according to SEM images. The standard deviations of the core size and shell thickness are also included for the theoretical calculations. The experimental plasmon response is in each case compared with the response obtained using Mie scattering theory, and the relative contributions of absorption and scattering to the overall extinction spectra of the nanoparticles are shown. The positions and

lineshapes of the plasmon peaks in the measured extinction spectra are in good agreement with Mie scattering theory. Three discernable peaks are observed. The peak in the range of 800-900 nm is identified as the dipole resonance, and the peak inflections observed at  $\sim 620$  nm and  $\sim 470$  nm correspond quite well to the predicted peak splitting discussed earlier (Figures 3-1 and 3-2). As the shell thickness increases, the quadrupole resonance becomes increasingly pronounced compared to the dipole resonance, and the dipole peak redshifts only slightly. These effects are due to phase retardation which increases with the particle size.<sup>55</sup>

In conclusion, the effects of interband transitions on the optical properties of metallic nanoparticles have been observed and investigated in the Cu nanoshell geometry. When a dipole or quadrupole plasmon overlaps the interband transition threshold, a double peaked plasmon resonance appears. The measured extinction spectra of experimentally fabricated Cu nanoshells are in good agreement with Mie scattering theory, and exhibit this behavior for a variety of shell thicknesses. In photonic device applications, Cu may potentially be desirable over Au or Ag due to its compatibility with Si based processing. Cu nanoshells are of significant interest for potential large-scale or large-area applications relative to their Au and Ag counterparts due to the significantly reduced relative cost of the constituent metal. In a more general sense, developing a better understanding of the role of electronic structure in the optical properties of metallic nanostructures may lead to increased interest in the development of plasmonic nanostructures based on other materials systems, incorporating additional properties and functionalities.

## **Chapter 4. Metallic nanoshells with semiconducting Cu<sub>2</sub>O cores**

As was seen in the previous chapter, the plasmonic response of a structure can be strongly modified when other optical processes occur simultaneously in the materials making up the shell. In this chapter, we examine the optical properties of Au nanoshells with semiconducting Cu<sub>2</sub>O cores. Cu<sub>2</sub>O is itself a fascinating material of particular importance for studying excitonic physics. In this work, Cu<sub>2</sub>O is interesting because the dielectric constant is significantly higher than silica and it is lossy in the visible and near-infrared. Increasing the dielectric constant of the core, for example replacing silica with Cu<sub>2</sub>O, results in the cavity plasmon resonance shifting to lower energies. In this respect, Cu<sub>2</sub>O is particularly interesting as the resulting cavity plasmon is nearly degenerate with the sphere plasmon for a nanoshell immersed in H<sub>2</sub>O. In the far field, we find that the high permittivity results in a dramatic increase in the absorption efficiency relative to the scattering efficiency, a significant redshift of the plasmon energy, a reduction in the plasmon linewidth. In the near field, the Cu<sub>2</sub>O core results in a strong enhancement of the electromagnetic field inside the core. We further explore the effect of the core dielectric on nanoshell plasmons by comparing Cu<sub>2</sub>O with two core materials previously used to fabricate Au nanoshells: silica, which has a much lower dielectric constant, and iron oxide, which has a much higher dielectric constant. We complete this discussion by examining the behavior of the near and far field as a continuous function of core dielectric for several nanoshell geometries. The Cu<sub>2</sub>O nanoshell synthesis presented here was performed by Rizia Bardhan, while I contributed the theoretical analysis. The work presented in this chapter is currently being prepared for publication.

Nanoshells, nanoparticles with dielectric cores and metallic shells, have elicited increasing scientific and technological interest due to their ability to manipulate light in unique ways. Their optical properties are governed primarily by the surface plasmons supported by this structure, whose resonance frequencies are tuned by varying the internal nanoparticle geometry. The surface plasmons give rise to intense local electromagnetic fields at the nanoshell surface, which have been harnessed for several photonic,<sup>10, 56</sup> spectroscopic<sup>27, 65</sup> and biomedical<sup>22, 66</sup> applications. At the plasmon resonance, these nanoparticles also exhibit large far field scattering and absorption cross sections. Nanoshell plasmons have also been shown to dramatically affect radiative transitions in materials adjacent or inside of a metallic nanostructure.<sup>4, 6, 9, 11, 22, 67</sup> Analogous to the Purcell effect in cavities and waveguides, emission from an adjacent excited atom, molecule, or semiconductor can decay directly into a resonant plasmon, modifying the available photon density of states and changing its radiative decay rate.<sup>4, 6, 11, 21</sup> The plasmon then radiates the emission to the far field. This is essentially a nanoantenna effect, where the nanoparticle serves to couple the emission of the adjacent fluorescent medium to the far field. The scattering cross section of the nanoshell is critically important to the efficiency of this process.

The plasmon resonance frequencies of nanoshells is a function of the dimensions and permeability of the core, the shell and the embedding medium.<sup>16, 68</sup> In addition to tuning the resonance energy, the core and shell properties also dramatically influence nanoshell absorption and scattering efficiencies. For simpler nanoparticles like nanospheres or nanorods, the amount of light absorbed or scattered by the nanoparticle is a function of nanoparticle size. While smaller nanoparticles are predominantly absorptive, the

absorption to scattering ratio decreases with increasing nanoparticle size, where ultimately larger particles are better light scatterers than light absorbers. With the layered nanoshell geometry, however, this relationship is more complex. Recently we showed that the absorption and scattering efficiencies of gold-silica-gold layered nanostructures can be modified, for a fixed nanostructure size, by tailoring the thickness of the intermediate dielectric layer.<sup>69</sup> In this study we show that by changing the core material to a higher permeability semiconductor cuprous oxide ( $\text{Cu}_2\text{O}$ ), the absorption and scattering cross sections of the nanoshell can be significantly altered. The unique ability to manipulate the optical properties of this nanoparticle by varying either internal geometry or material makes nanoshells extremely attractive for a wide variety of applications.

$\text{Cu}_2\text{O}$ , a semiconductor with a bandgap of 2.17 eV, is an ideal material for studying exciton physics. In bulk  $\text{Cu}_2\text{O}$ , the lowest-energy “yellow” exciton series is a prototypical example of Wannier excitons, with energy levels following a simple hydrogenic model for  $n \geq 2$ <sup>70, 71</sup> and oscillator strengths for  $n \geq 3$ .<sup>72</sup> The 1s state is distinct because its excitonic Bohr radius (0.53 nm) is comparable to the lattice constant (0.43 nm), resulting in several interesting properties. Electron-hole exchange interactions split the 1s exciton into a triply degenerate orthoexciton with total orbital angular momentum  $J = 1$ , and a paraexciton 12 meV below the orthoexciton with a total orbital angular momentum  $J = 0$ .<sup>71-74</sup> Due to the inversion symmetry of  $\text{Cu}_2\text{O}$ , direct creation of 1s excitons by one-photon optical transitions is only quadrupole allowed for the orthoexcitons and completely forbidden for the paraexcitons. In contrast, two-photon absorption processes may provide a route to populating these states. The small Bohr radius also results in a

large binding energy, approximately 150 meV for the paraexciton and 140 meV for the orthoexciton, attributable to the lack of Coulomb screening by the lattice. Because these excitons are strongly bound, they retain their bosonic character up to a relatively high temperature and density, providing a promising system for the study of excitonic Bose-Einstein condensation (BEC).<sup>72,75</sup> In addition to BEC, these excitons have also been well studied for numerous physical effects. The nearly ideal excitonic structure allows detailed studies of the manipulation of the band structure with magnetic, electrical and optical fields. This can be exploited to populate and probe optically forbidden exciton states,<sup>76-78</sup> and has led to the observation of dynamical Stark shifts in the exciton spectrum.<sup>79</sup> Exciton physics is not the only area in which Cu<sub>2</sub>O has attracted significant interest. Cu<sub>2</sub>O is also a promising material for third harmonic generation in the near- and mid-IR due to its significant non-resonant third order susceptibility ( $\chi^{(3)}$ ) combined with a lack of competing second order processes and minimal absorption of the generated light.<sup>80</sup> By encapsulating Cu<sub>2</sub>O in a nanoscale Au shell, the nanoshell plasmons generated at the Cu<sub>2</sub>O/Au interface can be used to effectively control the coupling of these excitons to light. This can be achieved both by dramatically enhancing the excitation field in the semiconductor, particularly important for two-photon absorption, and by tuning the radiative decay rate. More directly, coupling between plasmons and excitons can lead to the formation of hybrid plasmon-exciton, or plexciton, states. This has been previously observed for Frenkel excitons in J-aggregates adsorbed to the surface of a nanoshell.<sup>81</sup> The optically bright nanoshell plasmon modes can couple to the optically dark paraexcitons of Cu<sub>2</sub>O, providing a simple and feasible route for detecting these optically

forbidden exciton states. The nanoshell plasmon resonance also results in strong field enhancements which can dramatically increase the nonlinear response of the  $\text{Cu}_2\text{O}$  core.

In this study, we experimentally fabricate nanoshells consisting of a  $\text{Cu}_2\text{O}$  core coated with a thin Au shell, ( $\text{Cu}_2\text{O}/\text{Au}$ ) and, in conjunction with theoretical models, investigate the unique plasmonic properties of these nanoshells. The nanoshells were fabricated in the sub-100 nm and sub-150 nm size regime and have tunable plasmon resonances from the visible to the NIR region of the spectrum. Due to the high permittivity of  $\text{Cu}_2\text{O}$ , the plasmon resonance of  $\text{Cu}_2\text{O}/\text{Au}$  nanoshells were observed to red shift by  $\sim 100\text{-}130$  nm compared to nanoshells with a lower permittivity core material, such as  $\text{SiO}_2$  core ( $\epsilon \sim 2.04$ ) Au shell ( $\text{SiO}_2/\text{Au}$ ) nanoshells of equivalent dimensions. Theoretical analysis reveals that the larger dielectric constant of  $\text{Cu}_2\text{O}$  results in a nanoshell with high absorption efficiency compared to dielectric core materials such as  $\text{SiO}_2$ . The presence of the  $\text{Cu}_2\text{O}$  core material results in a strong enhancement of the electromagnetic field inside the nanoparticle. Due to their compact size, tunability in the NIR and larger absorption cross-sections,  $\text{Cu}_2\text{O}/\text{Au}$  nanoshells should also be highly efficient nanoparticles for photothermal heating applications in biomedicine, where efficient conversion of absorbed light to heat is required.

#### **4.1 Results and Discussion**

The  $\text{Cu}_2\text{O}/\text{Au}$  nanoshells were fabricated by a stepwise procedure by first synthesizing  $\text{Cu}_2\text{O}$  nanoparticles in the size range of  $15 \pm 0.5$  nm to  $350 \pm 150$  nm in radius in aqueous media at ambient temperature. The  $\text{Cu}_2\text{O}$  nanoparticles were fabricated by reducing copper (II) salts with ascorbic acid in the presence of sodium hydroxide and poly

(ethylene) glycol dithiol (HS-PEG-SH). This synthesized is adapted by modifying a protocol previously reported.<sup>82</sup> Briefly, 4 ml of 0.01 M aqueous CuSO<sub>4</sub> solution were mixed with 16 mL of PEG dithiol (MW 1530) at various concentrations under vigorous stirring at room temperature. Subsequently, 13 mL of 0.115 M NaOH and 10.5 mL of 0.005 M ascorbic acid were mixed together in a separate vessel and quickly added to the CuSO<sub>4</sub> - PEG dithiol solution mixture. The reaction was proceeded for an additional 2 minutes under vigorous stirring following which it was quenched by blowing an inert gas (N<sub>2</sub> or Ar) into the reaction mixture for 20 minutes. Depending on the particle size, the solution turns from colorless to bright yellow (for smaller Cu<sub>2</sub>O nanoparticles) or orange (for larger Cu<sub>2</sub>O nanoparticles) in color. The nanoparticles were purified and excess PEG dithiol was removed by centrifuging the nanoparticles between 5500 – 7000 rpm depending on particle size. Representative scanning electron microscope (SEM) images of the Cu<sub>2</sub>O nanoparticles verify their morphology and dimensions (Figure 4-1). X-ray powder diffraction spectra confirmed the composition of the Cu<sub>2</sub>O nanoparticles. By simply varying the concentration of HS-PEG-SH, which acts as a stabilizing polymer, while keeping the concentration of the other reagents constant, the size of the Cu<sub>2</sub>O nanoparticles were straightforwardly tuned. It is noticeable that the polydispersity is as low as ~ 3% for the nanoparticle sizes  $\leq 200$  nm; however, for the larger nanoparticles polydispersity increases beyond 10%. This observation indicates that at higher HS-PEG-SH concentrations, more nucleation sites are initiated leading to a higher rate of growth kinetics resulting in a larger size distribution. As the size of the nanoparticle increases, particularly for sizes  $\geq 200$  nm, more particles exhibit truncated cubic rather than near-spherical shapes (Figure 4-1). The preferential adsorption of ions in a solution to different

crystalline faces directs the development of nanoparticles into unusual shapes by controlling the growth kinetics along the different crystal axes.<sup>83</sup> For Cu<sub>2</sub>O, cubic shape is known to form when the crystalline growth is along the (111) plane.<sup>84</sup> The observed shapes imply that a fraction of the PEG-dithiol molecules may be adsorbing on the (111) plane and hence assisting in the morphological development of the Cu<sub>2</sub>O nanoparticles along the <111> direction. In addition, the HS-PEG-SH molecules also terminate the Cu<sub>2</sub>O nanoparticles with thiol groups which can attach to Au without the need of further functionalization for Au coating.

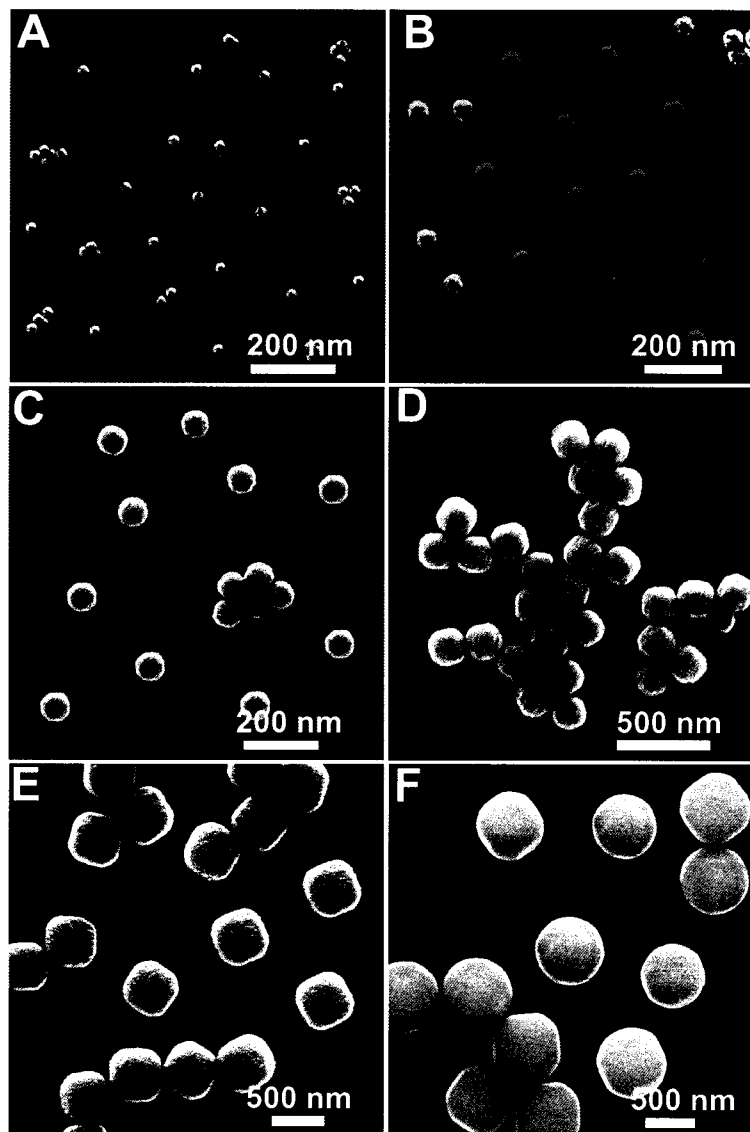


**Figure 4-1** SEM images of Cu<sub>2</sub>O nanoparticles of different sizes. The radii of the nanoparticles are (A)  $15 \pm 0.5$  nm, (B)  $30 \pm 1$  nm, (C)  $50 \pm 2$  nm, (D)  $100 \pm 5$  nm, (E)  $250 \pm 30$  nm, and (F)  $350 \pm 50$  nm.

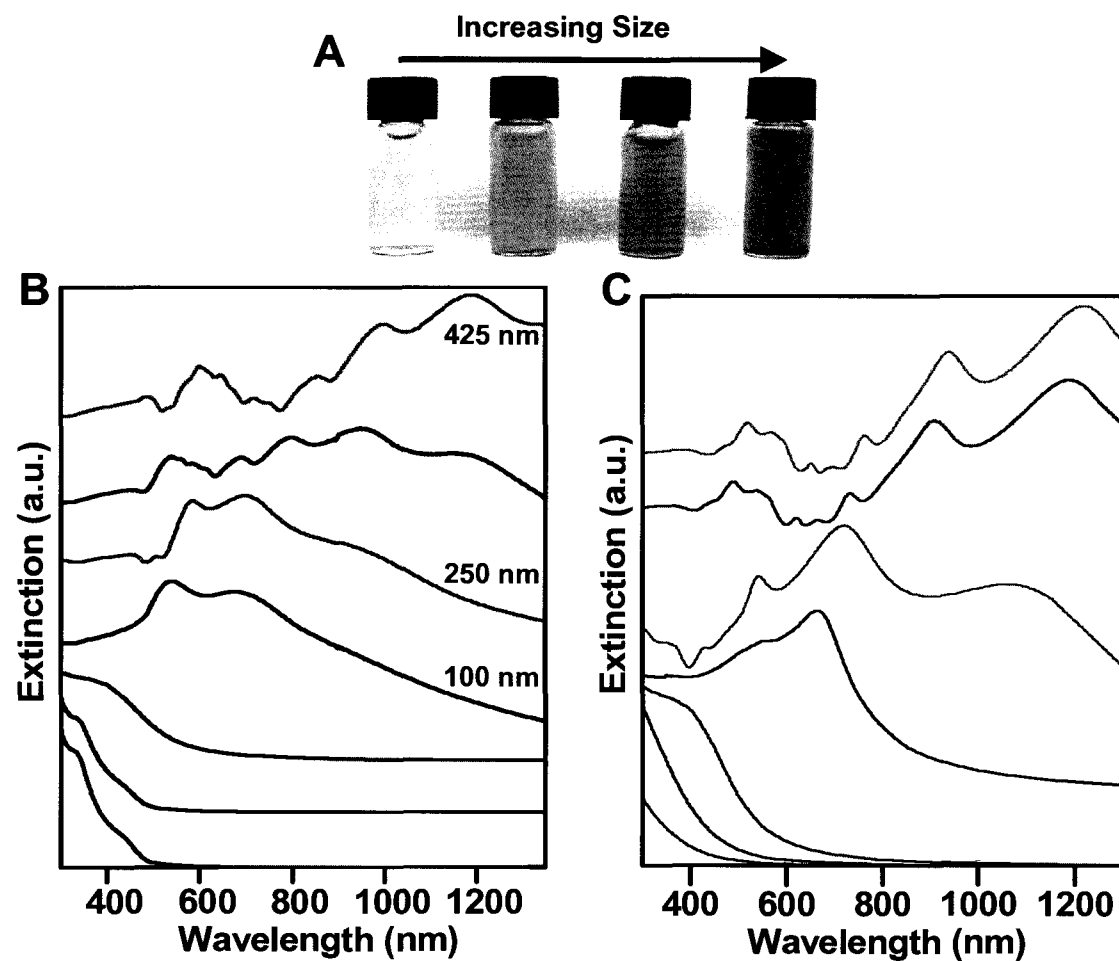


**Figure 4-2** (A) Optical image of Cu<sub>2</sub>O nanoparticles dispersed in aqueous media of increasing sizes. (B) Experimental absorption spectra of the Cu<sub>2</sub>O nanoparticles dispersed in aqueous media. The radius of the nanoparticles corresponding to the spectra is indicated on the right. Spectra are offset for clarity. (C) Calculated absorption spectra of the Cu<sub>2</sub>O nanoparticles in aqueous media ( $n = 1.33$ ). The spectra are color coordinated with part (B) and offset for clarity.

The experimental and theoretical optical properties of the Cu<sub>2</sub>O nanoparticles demonstrate the shape dependent optical response of these nanoparticles (Figure 4-2). Optical images (Figure 4-2A) of the Cu<sub>2</sub>O nanoparticles dispersed in aqueous media clearly shows as the nanoparticle sizes increase the solution changes from bright yellow to orange, similar to that reported previously for Cu<sub>2</sub>O nanostructures.<sup>82</sup> Experimental extinction spectra of the Cu<sub>2</sub>O nanoparticles of different sizes dispersed in aqueous media

demonstrate the different peaks that arise as the size of the nanoparticles increase (Figure 4-2B). The radius of the nanoparticles corresponding to each optical spectrum is indicated on the right. The extinction spectra of the smaller nanoparticles ( $\leq 100$  nm) exhibit strong Rayleigh scattering and a small peak at 440 nm. As the nanoparticle sizes increase to 200 nm, new peaks are observed in the visible near 530 nm and in the near-infrared near 700 nm. With increasing size of the  $\text{Cu}_2\text{O}$  nanoparticles, the peaks in the visible and the near-infrared red shifts and additional features are observed in the near and mid-infrared. These additional extinction peaks observed for the larger nanocrystals are due to scattering at the well known Mie resonances of dielectric particles.<sup>18, 85</sup>

The theoretical extinction spectra of the  $\text{Cu}_2\text{O}$  nanoparticles (Figure 4-2C) were obtained utilizing Mie theory assuming a spherical geometry with diameters matching the experimentally obtained nanoparticle sizes. The calculated extinction spectra correspond well to the measured spectra for all the nanoparticle sizes. Small disparities between calculated and experimental spectra are plausibly due to polydispersity, the combination of spherical and truncated cubic shapes in the nanoparticle solutions, and small variations in the dielectric function of the fabricated particles from the values for bulk  $\text{Cu}_2\text{O}$  obtained from literature.<sup>86</sup> Nanoparticles have been reported to have higher band gap energy compared to the bulk material which is attributed to impurities and defects in crystal structure.<sup>84</sup> The  $\text{Cu}_2\text{O}$  nanoparticles also form self-assembled ordered arrays when a droplet of the nanoparticle solution is allowed to dry in ambient air at room temperature on a silicon or quartz substrate.

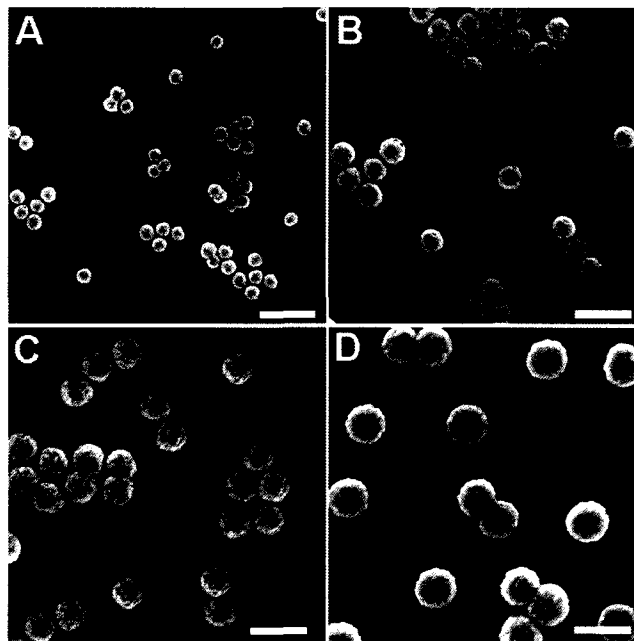


**Figure 4-3** SEM images of  $\text{Cu}_2\text{O}/\text{Au}$ -NS of different sizes. (A)  $[r_1, r_2] = [15, 32]$  nm, (B)  $[r_1, r_2] = [30, 46]$  nm, (C)  $[r_1, r_2] = [40, 54]$  nm, (D)  $[r_1, r_2] = [50, 65]$  nm. The scale bar is 200 nm.

The  $\text{Cu}_2\text{O}/\text{Au}$  nanoshells were fabricated by seed mediated electroless plating of Au onto  $\text{Cu}_2\text{O}$  nanoparticles. Briefly, monodisperse  $\text{Cu}_2\text{O}$  nanoparticles were decorated with small gold colloid (2- 3 nm) A continuous gold shell was grown around the  $\text{Cu}_2\text{O}$  nanoparticles by The fabricated  $\text{Cu}_2\text{O}/\text{Au}$  nanoshells were centrifuged several times and finally redispersed in aqueous media to form desired particle concentrations.

$\text{Cu}_2\text{O}/\text{Au}$  nanoshells are fabricated by seed mediated electroless plating of Au onto the thiol terminated  $\text{Cu}_2\text{O}$  nanoparticles.<sup>17, 26</sup> Small Au nanoparticles ( $\sim 2$  nm in diameter), prepared by the method reported by Duff et al.,<sup>87</sup> are immobilized onto the surface of the  $\text{Cu}_2\text{O}$  cores. The immobilized Au nanoparticles act as nucleation sites for electroless plating of Au onto the surface of core particles, which gradually results in the formation

of a continuous and complete metal shell layer upon reduction. The plating solution was prepared by mixing 50 mg of  $K_2CO_3$  with 200 mL of  $H_2O$  and 3 mL of a 1 %  $HAuCl_4$  solution and allowed to age for 24 hours before using. The shell is grown by reducing  $Au^+$  from this plating solution onto the attached small colloid in the presence of  $CO_{(g)}$ .<sup>17,</sup>  
<sup>26</sup> Further metal deposition onto the nanostructure increases the thickness of the Au layer. SEM images of  $Cu_2O/Au$  nanoshells fabricated on cores ranging in size from a radius of 15 nm to 50 nm are shown in Figure 4-3. While  $Cu_2O$  nanoparticles can be synthesized in different shapes,<sup>82,88</sup> the growth of a uniform Au layer on the nanoparticles modifies the overall shape. The Au shell grows as a polycrystal on the  $Cu_2O$  nanoparticle cores and hence results in a spherical morphology with minor surface roughness. This facile synthesis route allows the fabrication of uniform, monodisperse, and non-flocculated core-shell nanostructures in sub-150 nm and sub-100 nm size regimes. The Au coating also allows dispersibility in aqueous media and provides a biocompatible surface, which can be straightforwardly conjugated with functional molecules.

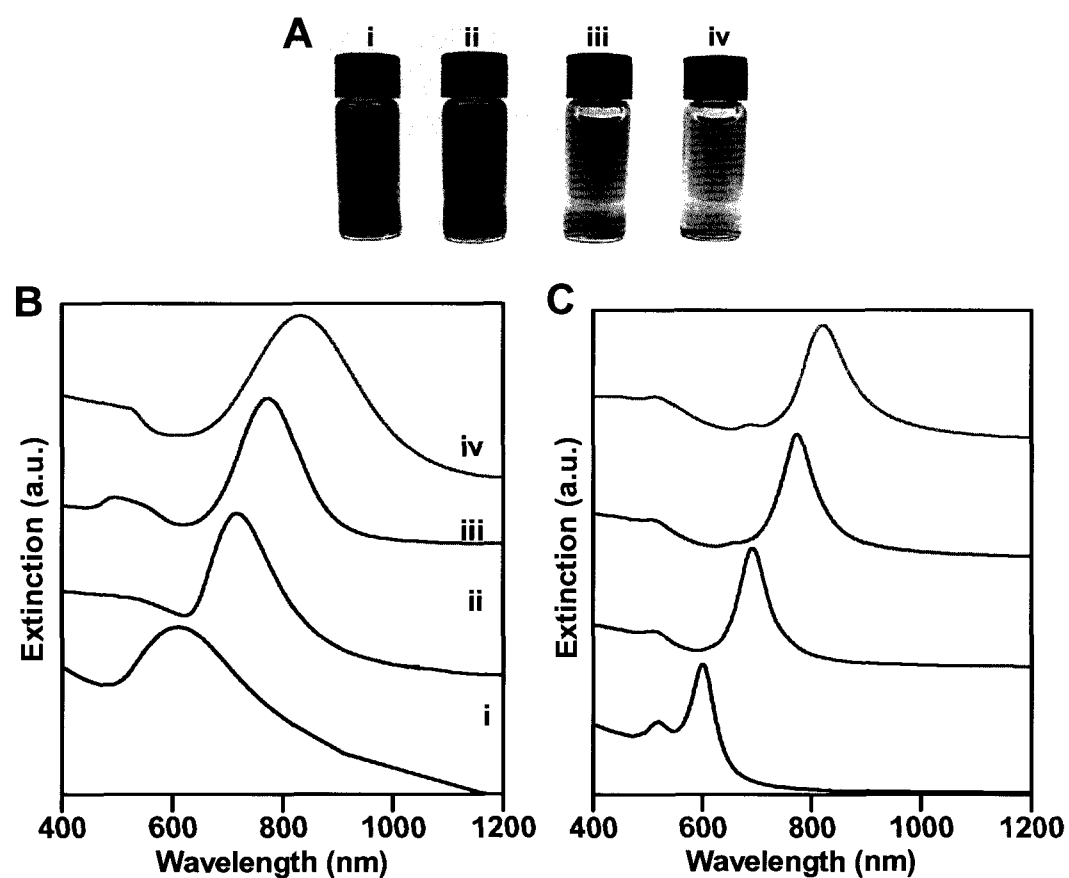


**Figure 4-4** (A) Optical image of Cu<sub>2</sub>O/Au-NS of different sizes. (i)  $[r_1, r_2] = [15, 32]$  nm, (ii)  $[r_1, r_2] = [30, 46]$  nm, (iii)  $[r_1, r_2] = [40, 54]$  nm, and (iv)  $[r_1, r_2] = [50, 65]$  nm. (B) Experimental extinction spectra of Cu<sub>2</sub>O/Au-NS dispersed in aqueous media of different sizes: (i)  $[r_1, r_2] = [15, 32]$  nm,  $\lambda_{\max} = 610$  nm, (ii)  $[r_1, r_2] = [30, 46]$  nm,  $\lambda_{\max} = 705$  nm (iii)  $[r_1, r_2] = [40, 54]$  nm,  $\lambda_{\max} = 780$  nm and (iv)  $[r_1, r_2] = [50, 65]$  nm,  $\lambda_{\max} = 830$  nm. Spectra are offset for clarity. (C) Calculated extinction spectra of the Cu<sub>2</sub>O/Au-NS in aqueous media. The spectra are color coordinated with part (B) and offset for clarity. The calculations were performed assuming spherical core and shell geometry.

The experimental and calculated optical properties of the Cu<sub>2</sub>O/Au nanoshells are represent the morphological development of the Cu<sub>2</sub>O after Au shell growth (Figure 4-4). The optical images of Cu<sub>2</sub>O/Au nanoshells dispersed in aqueous media (Figure 4-4A) indicates a change in the solution color from purple to blue as the size of the Cu<sub>2</sub>O/Au nanoshells increases. The experimentally observed extinction spectra of the Cu<sub>2</sub>O/Au nanoshells dispersed in aqueous media with different core/shell ratios corresponding to

the SEM images (Figure 4-3) are illustrated in Figure 4-4B. The extinction spectra spans from the visible to the NIR region of the optical spectrum with the smallest size  $[r_1, r_2] = [15, 32]$  nm showing a plasmon resonance at 610 nm. With increasing nanoshell sizes, the plasmon resonance red shifts to 705 nm, 780 nm, and 830 nm respectively (Figure 4-4A). In the quasistatic limit, where the size of the nanoshell is much smaller than the spatial wavelength of light, the plasmon resonance energies of a nanoshell are determined by their aspect ratio  $r_1 / r_2$ .<sup>89</sup> As the aspect ratio increases the plasmon resonance shifts to longer wavelengths. As the nanoshell size becomes significant compared to the wavelength of light at the plasmon resonance, phase retardation causes an additional redshift with increasing nanoparticle size.<sup>16</sup> In Figure 4-4, the shell thickness is held nearly constant while the core size is increased, resulting in an increasing aspect ratio and concomitant shift of the plasmon resonance to longer wavelengths as the size of the Cu<sub>2</sub>O/Au nanoshells increases. The calculated extinction spectra of the Cu<sub>2</sub>O/Au nanoshells corresponding to those observed experimentally were obtained using Mie theory assuming a spherical core and spherical shell geometry (Figure 4-4C). The calculated spectra and peak positions correspond well with the experimental extinction spectra suggesting that Cu<sub>2</sub>O nanoparticles  $\leq 100$  nm are mostly spherical and the small fraction of truncated cubic shapes present do not affect the ensemble plasmon line shape or peak position. For the smallest fabricated Cu<sub>2</sub>O/Au nanoshells, with  $[r_1, r_2] = [15, 32]$  nm, the observed plasmon line width is larger than those obtained theoretically, probably due to inhomogeneities in the Au layer thickness and some aggregation of the nanoshells after the growth of the Au layer.

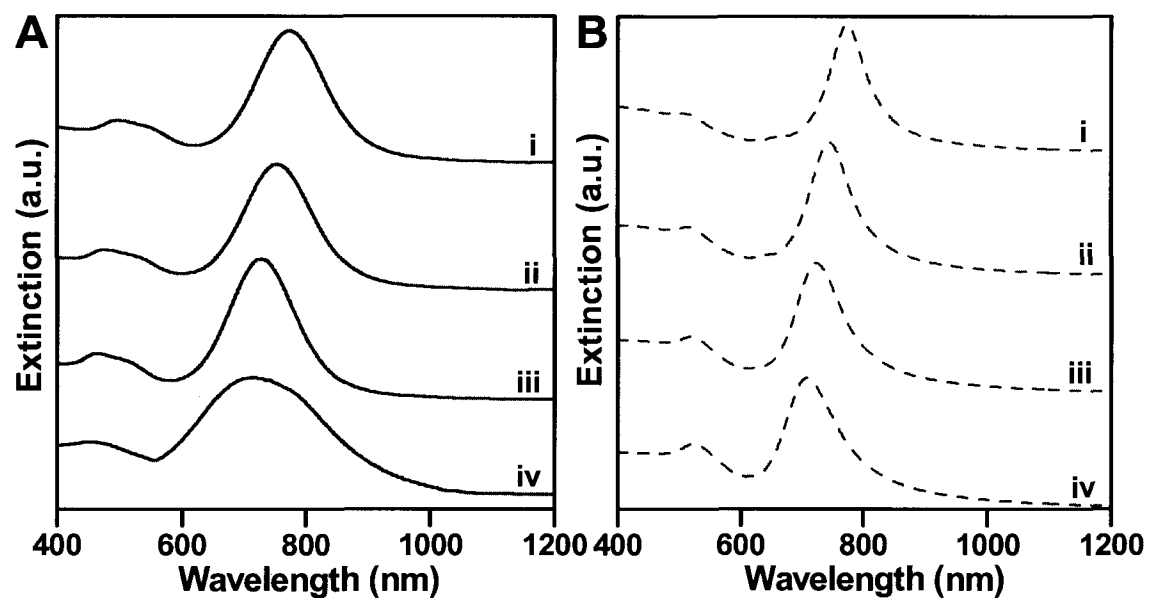


**Figure 4-5** (A) Experimental extinction spectra of  $\text{Cu}_2\text{O}/\text{Au}$ -NS for core radius  $r_1 = 40 \pm 2$  nm with varying Au shell thicknesses: (i)  $r_2 = 54 \pm 5$  nm, (ii)  $57 \pm 5$  nm, (iii)  $60 \pm 7$  nm and (iv)  $63 \pm 11$  nm. (B) Calculated extinction spectra of  $\text{Cu}_2\text{O}/\text{Au}$ -NS of similar sizes as observed experimentally. The calculations were performed assuming a spherical core and shell geometry.

The tunability of the plasmon resonance was also observed experimentally by varying the Au shell thickness for a fixed core size. The experimental extinction spectra of  $\text{Cu}_2\text{O}/\text{Au}$  nanoshells with the same core radius  $40 \pm 2$  nm and varying the shell thicknesses, for a total outer radius of  $54 \pm 5$  nm,  $57 \pm 5$  nm,  $60 \pm 7$  nm, and  $63 \pm 11$  nm, are shown in Figure 4-5A. Spectra calculated using Mie theory correspond well to the experimental extinction spectra (Figure 4-5B). With increasing Au shell thickness the aspect ratio  $r_1 / r_2$  increases similar to that observed in Figure 4-4, the plasmon resonance peak blue shifts to shorter wavelengths from 780 nm to 710 nm.

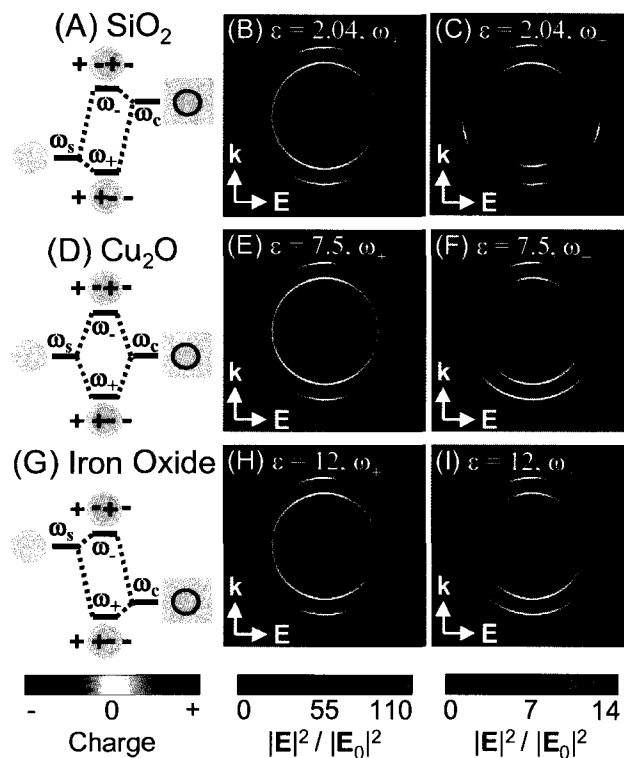


**Figure 4-6** Plasmon hybridization diagram (left) and the surface charge overlaid on the near field intensity enhancement at the bonding (middle) and antibonding (right) plasmon resonance for Au nanoshells with (A-C) SiO<sub>2</sub>, (D-F) Cu<sub>2</sub>O, or (G-I) iron oxide cores.

Conceptually, these trends can be straightforwardly understood in terms of plasmon hybridization, an analytical tool useful for understanding the resonant modes of complex metal nanostructures.<sup>39</sup> In this model, plasmon modes supported by a solid sphere and a hollow spherical cavity interact to form hybrid nanoshell plasmon modes in an analogous fashion to molecular orbital hybridization theory. This interaction is shown schematically in Figure 4-6 along with the resulting dipolar ( $\omega_+$ ) bonding and antibonding ( $\omega_-$ ) plasmon modes. In vacuum, the sphere plasmons are at a lower energy than the cavity plasmons. The resonance energy of these primitive plasmons depend on the surrounding environment; increasing the medium ( $\epsilon_m$ ) or core ( $\epsilon_c$ ) dielectric constant shifts the sphere or cavity plasmon, respectively, to longer wavelengths. The medium is often determined by the application. For example, in biological applications, the particles will generally be

immersed in an aqueous environment with  $\epsilon_m \sim 1.8$ . The choice of core material is often less restrictive, in which case it provides an additional tool to change properties of the plasmon resonance in metallic nanoshells beyond what is possible by geometry alone. In air ( $\epsilon_m = 1$ ), the sphere and cavity resonance energies are degenerate for a cavity dielectric  $\epsilon_c \sim 5.5$ , while for water ( $\epsilon_m = 1.77$ ) the resonances are at the same energy for  $\epsilon_c \sim 8$ .

Changes in the plasmonic response of nanoshells due to changing the core dielectric arise can be understood in terms of four effects: (i) the core dielectric screens the charge on the inner surface of the nanoshell, resulting in an increased imbalance in the surface charge on the inner and outer surface of the Au shell, (ii) plasmon hybridization between the sphere and cavity plasmons, (iii) the change in the relative size of the nanoshell to the wavelength of light at the plasmon resonance, and (iv) energy dissipation in the core if the imaginary part of the core dielectric is non-zero. As the core permittivity increases, it polarizes more strongly in opposition to the electric field imposed by the shell, reducing the overall surface charge on the inner surface of the Au shell. The increased imbalance of the surface charge on the inside and outside surfaces of the shell generates a larger field across the metal. At the bonding dipole resonance, where the dipole moments of cavity and sphere modes are aligned, the polarization of the core, which is opposes the cavity and sphere plasmons, results in a weaker overall dipole moment. At the antibonding dipole resonance, where the dipole moments of the cavity and sphere plasmons cancel, the polarization of the core results larger total dipole moment. The polarization of the core also results in a nearly uniform electric field in the core. Essentially, changing the core dielectric allows the location of local electromagnetic

fields to be moved. In terms of plasmon hybridization, the high permittivity core shifts the plasmon resonance of the cavity-like mode to lower energy resulting in an increase in the admixture of the cavity plasmons in the bonding mode since the energy of the sphere and cavity modes are closer. Hence, despite this mode maintaining a strong dipole moment, due to interaction with the cavity plasmons the energy is primarily lost to absorption because the cavity mode does not radiate effectively. This effect also occurs for the antibonding plasmon mode. Due to the larger admixture of the sphere-like plasmons, the dipole moment increases allowing it to interact with light. Changing the primitive cavity plasmon resonance energy also results in a shift in the hybridized nanoshell plasmons. For all but the smallest nanoshells fabricated in this work, phase retardation effects due to the finite size of the particle compared to the wavelength of light at the plasmon resonance plays a significant role. The shift in the plasmon resonance wavelength due to changes in the core dielectric can significantly alter the relative particle size compared to the wavelength.

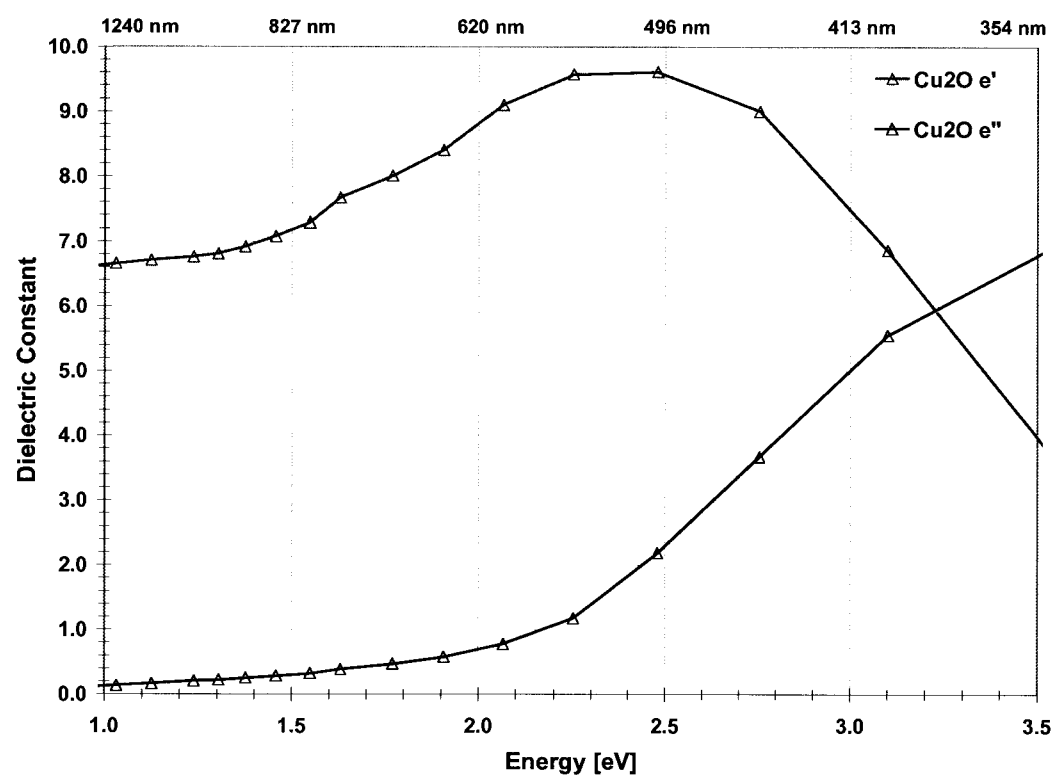


**Figure 4-7** Real ( $\epsilon'$ ) and imaginary ( $\epsilon''$ ) parts of the complex dielectric function of  $\text{Cu}_2\text{O}$  obtained from ref. 26.

To understand the effect changing the core dielectric has on the nanoshell plasmons in more concrete terms, we can compare  $\text{Cu}_2\text{O}$  to two previously studied oxides with a much lower and much higher dielectric constant:  $\text{SiO}_2$  and iron oxide. For  $\text{SiO}_2/\text{Au-NS}$ , shown in Figure 4-11(A), the cavity plasmon resonance energy is significantly higher than the sphere plasmon. For  $\text{Cu}_2\text{O}$  in the NIR, the dielectric constant ranges from 6.8 to 8.4 (Figure 4-7). This results in nearly equal cavity and sphere plasmon resonance energies as illustrated in Figure 4-6D. Recently developed iron oxide core nanoshells, with an effective  $\epsilon_c \sim 12$ , provide an example of the third possible case (Figure 4-6G) where the cavity plasmon is at much lower energy than the sphere plasmon.

The local electromagnetic field intensity enhancement  $|\mathbf{E}|^2 / |\mathbf{E}_0|^2$ , where  $|\mathbf{E}_0|^2$  is the intensity of the applied field, and surface charges on the inner and outer surface of the shell at the dipole bonding and anti-bonding resonances can be readily evaluated using Mie theory. Several conclusions can be drawn just from looking at the distribution of the local fields and surface charges, shown in the right two columns of Figure 4-6 for an  $[r_1, r_2] = [40, 54]$  nm nanoshell with a  $\text{SiO}_2$ ,  $\text{Cu}_2\text{O}$ , or iron oxide core. For low core dielectrics, there is very little field inside the particle at the bonding (symmetric) dipole mode (Figure 4-6B), while the antibonding mode (Figure 4-6C) is very weak due to almost perfect cancellation of the oppositely aligned sphere and cavity plasmon dipole moments. As the core dielectric is increased, a significant field in the core region appears due to the polarization of the sphere as can be seen at the bonding dipole resonance for  $\text{Cu}_2\text{O}$  (Figure 4-6E) and iron oxide (Figure 4-6H). While the maximum value of the field enhancement in the core is smaller than on the outer surface of the nanoshell, the volume over which it extends is significantly larger. This is important because the total signal observed for optical processes driven by the enhanced near fields is proportional to the enhancement integrated over the volume containing the material being probed, which is far larger for the field in the core than on the surface of the nanoshell. For  $\text{Cu}_2\text{O}$  and iron oxide, the larger core dielectric results in a dramatic increase in the strength of the antibonding resonance. The opposite phase of the charge on the inner and outer surface of the nanoshell at the antibonding resonance results in a field within the metal shell as can be seen in Figure 4-6F and I. The field on the outer surface of the nanoshells is also increases significantly, exceeding 10% of the intensity observed at the bonding resonance. For large  $\epsilon_c$ , the field enhancement at the antibonding resonance is weak

compared to the bonding resonance only because they are strongly damped by the Au interband transitions.

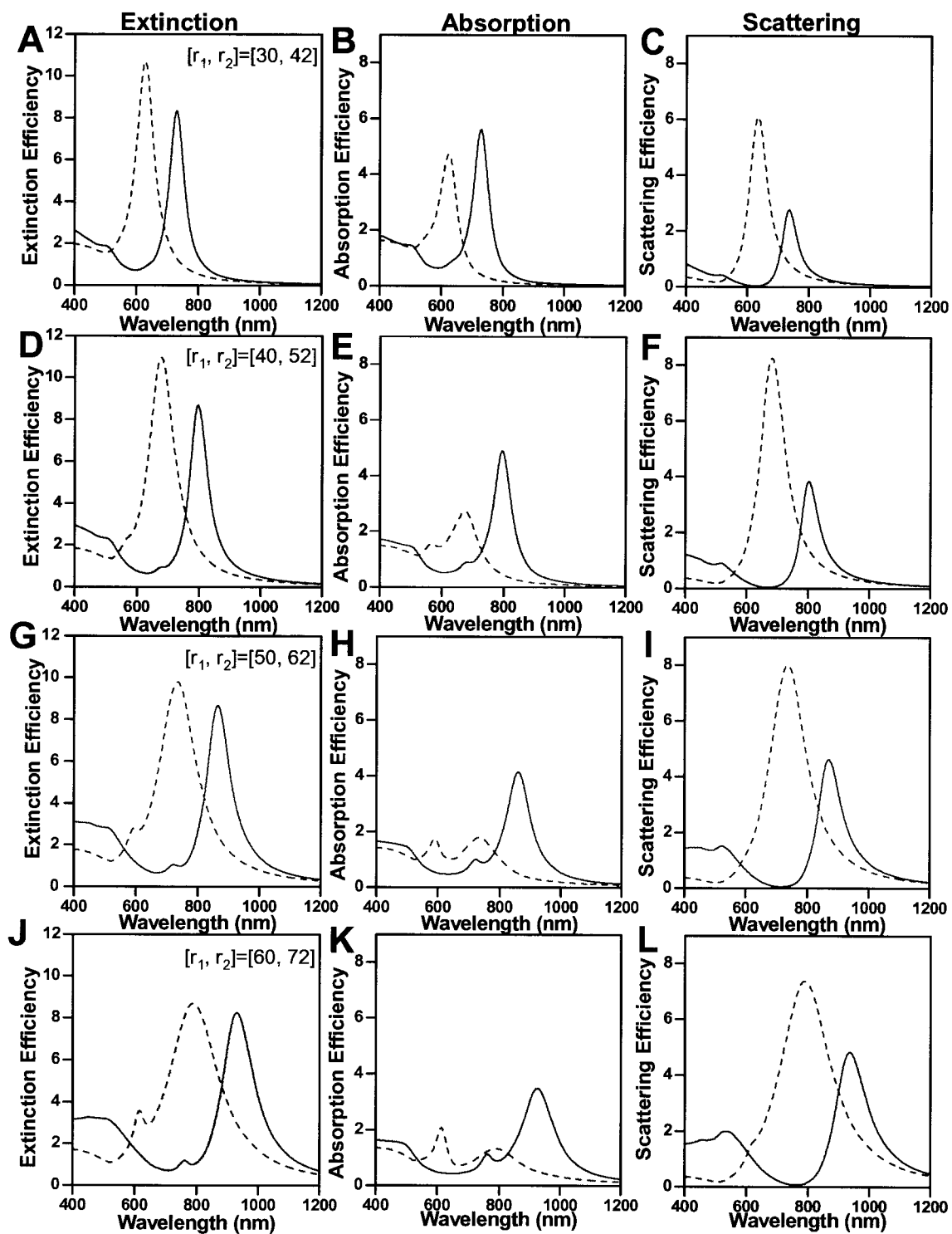


**Figure 4-8** Calculated extinction, absorption, and scattering efficiency spectra of  $\text{Cu}_2\text{O}/\text{Au}$ -NS (solid) compared with  $\text{SiO}_2/\text{Au}$ -NS (dash) nanostructures of different sizes. (A-C)  $[r_1, r_2] = [30, 42]$  nm, (D-F)  $[r_1, r_2] = [40, 52]$  nm, (G-I)  $[r_1, r_2] = [50, 62]$  nm, (J-L)  $[r_1, r_2] = [60, 72]$  nm. The calculations are performed assuming a spherical core encapsulated in a spherical shell.

Spectrally, three significant differences are apparent in the theoretical extinction, absorption, and scattering spectra of Cu<sub>2</sub>O/Au nanoshells (solid) compared with SiO<sub>2</sub>/Au nanoshells (dashed) of four different sizes,  $[r_1, r_2] = [30, 42]$  nm,  $[40, 52]$  nm,  $[50, 62]$  nm, and  $[60, 72]$  nm, shown in Figure 4-8. First, the peaks in the extinction spectra of the Cu<sub>2</sub>O/Au nanoshells, arising from the plasmon resonances, are shifted  $\sim 100$ -130 nm to longer wavelengths compared to the SiO<sub>2</sub>/Au nanoshells of equivalent dimensions for all the sizes calculated here. Second, the overall scattering efficiency of SiO<sub>2</sub>/Au nanoshells is higher than Cu<sub>2</sub>O/Au nanoshells for similar dimensions, despite the extinction being only slightly weaker. This is consistent with the observation in Figures 4-6B and 4-6E that the near fields shift inside the particle. Finally, the line width is also reduced slightly in the case of Cu<sub>2</sub>O/Au nanoshells.

From the prospective of the plasmon hybridization model, there are two important reasons for the observed spectral changes between SiO<sub>2</sub> and Cu<sub>2</sub>O core nanoshells with the same geometry. First, the bonding dipole mode shifts to longer wavelengths because the cavity plasmon mode has shifted to lower energies. Scattering is essentially due to radiative decay of the plasmons. Much like antennas in the RF, nanoparticles that are much smaller than the wavelength of light do not efficiently radiate electromagnetic energy. The decrease in the relative size of the nanoshell compared to the wavelength as the plasmon shifts to longer wavelengths therefore leads to a decrease in the relative importance of scattering compared to absorption in the far field extinction spectra when the core dielectric is changed from SiO<sub>2</sub> to Cu<sub>2</sub>O.<sup>27, 90</sup> This effect can also be seen by comparing the scattering and absorption efficiency of the  $[30, 42]$  nm nanoshell (Figure 4-8B, C) to the  $[60, 72]$  nm nanoshell (Figure 4-8K, L). As the nanoshell size increases,

the absorption decreases while the scattering rapidly increases. For the SiO<sub>2</sub> core nanoshell, this effect is so strong that absorption at the bonding dipole resonance almost vanishes compared to scattering for the [60, 72] nm nanoshell. This is also responsible for the decreased linewidth in Cu<sub>2</sub>O nanoshells; a decrease in the radiative damping results in a decrease in the rate of energy loss from the plasmon resonance which manifests itself as a decreased linewidth. Second, the relative energy of the sphere and cavity plasmons changes the interaction strength and hence the admixture of each primitive plasmon in the overall nanoshell plasmons. As the cavity plasmon resonance energy shifts to lower energy, approaching the sphere plasmon resonance, the admixture of the cavity plasmon in the low-energy bonding nanoshell plasmon increases, while the admixture of the sphere plasmon in the high-energy antibonding nanoshell plasmon increases. The sphere-like plasmons couple much more strongly to light than the cavity-like plasmons. As a result, the increasing admixture of cavity-like plasmon results in a decrease in the scattering cross section at the bonding dipole resonance as the core dielectric is increased. Conversely, the increasing admixture of the sphere-like plasmons in the antibonding nanoshell dipole mode increases, resulting in the appearance of a significant peaks at wavelengths shorter than 600 nm in the scattering spectrum of the [50, 62] nm and [60, 72] nm nanoshells shown in Figures 4-8I and 4-8L.

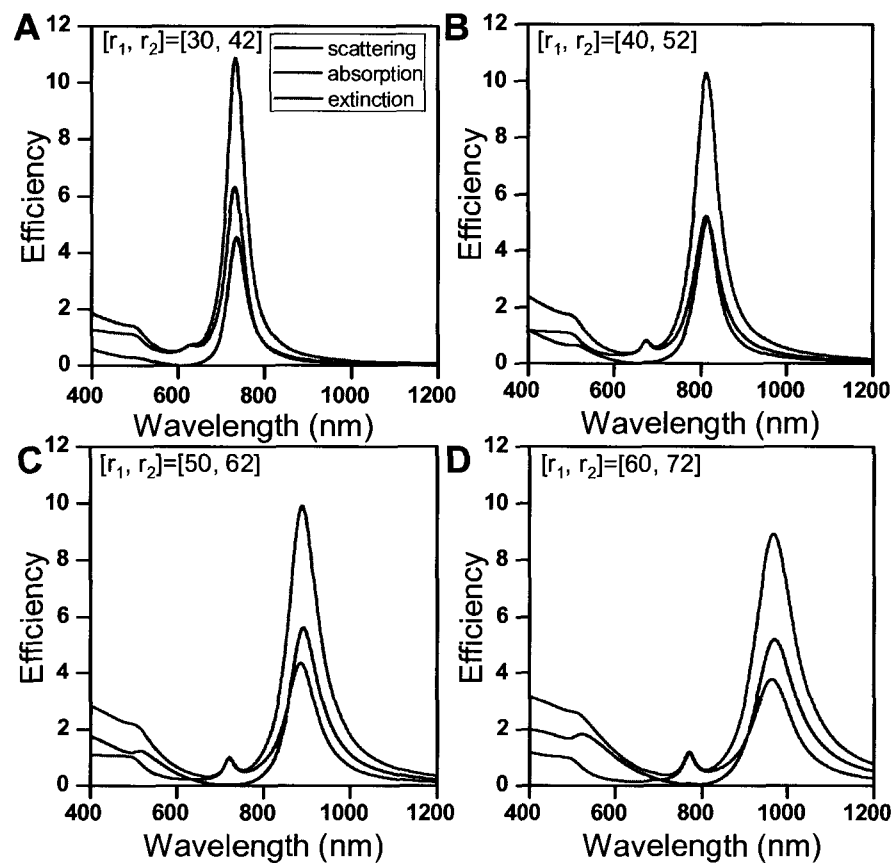


**Figure 4-9** Calculated extinction (blue), absorption (red) and scattering (black) spectra of  $\text{Cu}_2\text{O}/\text{Au}$  nanoshells of different sizes. Calculation performed using Mie theory assuming a spherical core and spherical shell with a constant real permittivity of 8 for the cores.

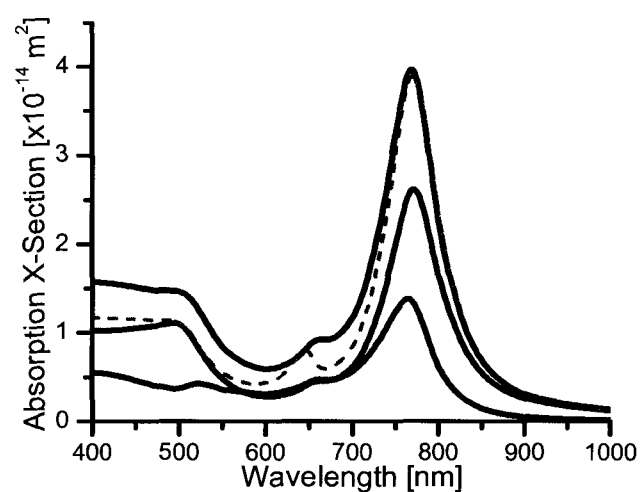


**Figure 4-10** Total optical absorption cross section for an  $[r_1, r_2] = [40, 52]$  nm  $\text{Cu}_2\text{O}/\text{Au}$ -NS (solid black line), separated into the contribution from the core (solid red line) and shell (solid blue line). The total absorption cross section for a nanoshell of the same dimensions but a constant real  $\epsilon_c = 7.6$  is shown for comparison (dashed orange line).

Losses due to absorption in the semiconducting  $\text{Cu}_2\text{O}$  core, absent in a transparent dielectric like  $\text{SiO}_2$ , might be expected to contribute to the increased absorption efficiency. Calculated extinction, scattering and absorption efficiencies of  $\text{Cu}_2\text{O}/\text{Au}$  nanoshells using constant real permittivity of 8 for the cores demonstrates that the absorption and scattering efficiencies are comparable for both the constant dielectric and the frequency dependent dielectric function (Figure 4-9). Surprisingly, despite the small change in the overall extinction, separating the absorption into the contribution from Joule losses in the core and shell indicates that more than a quarter of the energy is absorbed in the core when the complex frequency dependent dielectric function of  $\text{Cu}_2\text{O}$  is employed (Figure 4-10). This is essentially because the observed spectra arise from the plasmon resonance, which is a coherent motion of the conduction electrons in the shell. As the number of electrons is unaffected by the imaginary part of the core dielectric, the overall extinction can only be weakly effected by absorption in the core.

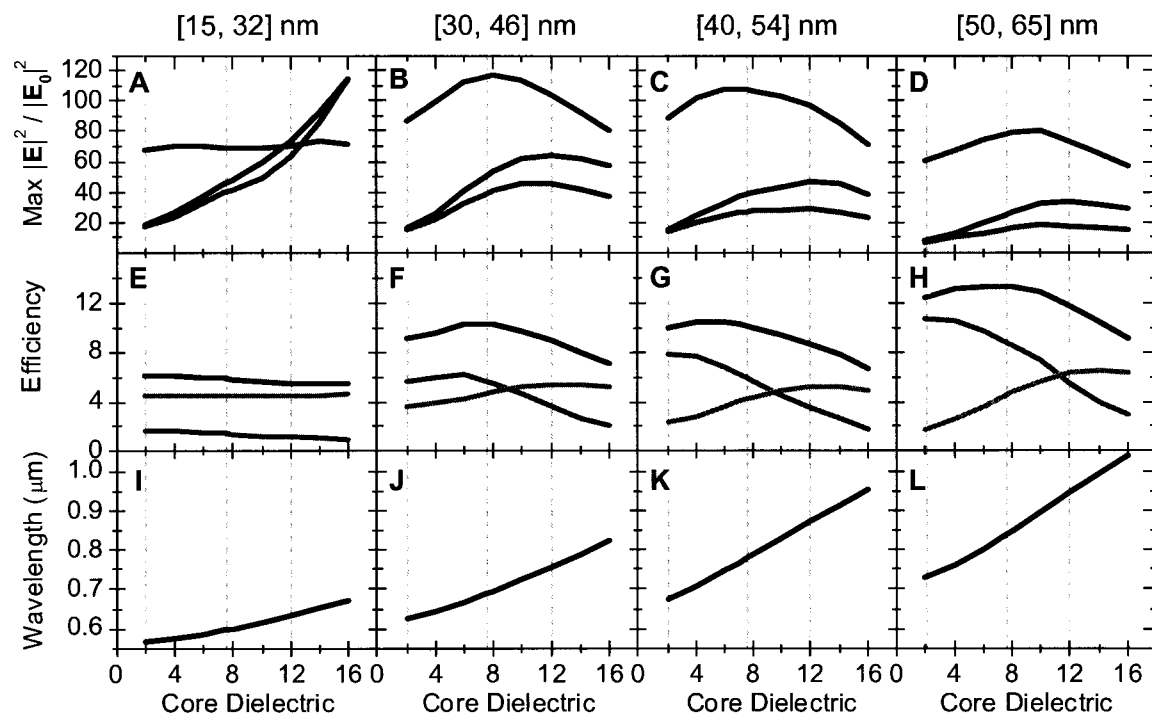


**Figure 4-11** Effect of the core dielectric on (A-D) the peak near field intensity enhancement in the (—) core, (—) shell and (—) medium, and (E-H) far field (—) scattering, (—) absorption and (—) extinction at the (I-L) dipole plasmon resonance for nanoshells of four aspect ratios: (A,E,I)  $r_1 / r_2 = 15 \text{ nm} / 32 \text{ nm} = 0.47$ , (B,F,J)  $r_1 / r_2 = 30 \text{ nm} / 46 \text{ nm} = 0.65$ , (C,G,K)  $r_1 / r_2 = 40 \text{ nm} / 54 \text{ nm} = 0.74$ , and (D,H,L)  $r_1 / r_2 = 50 \text{ nm} / 65 \text{ nm} = 0.77$ . The dielectric function of the three oxides considered here are indicated by dashed vertical lines:  $\text{SiO}_2$  at  $\epsilon_c = 2.04$ ,  $\text{Cu}_2\text{O}$  at  $\epsilon_c = 7.5$ , and iron oxide at  $\epsilon_c = 12$ .

A more complete understanding of the effect of changing the core dielectric can be obtained by examining the behavior of the near field in the core, shell, and medium and the far field at the bonding dipole peak as a function of core dielectric, shown in Figure 4-11 for the same four experimentally fabricated nanoshell geometries shown in Figure 4-4. The near field in the core, shell, and medium as well as the far field scattering, absorption, and extinction efficiencies will all peak at slightly different wavelengths. On the scale shown in Figure 4-11J-L, this difference is on the order of the thickness of the plotted lines and therefore only the wavelength where the maximum near field on the outer surface of the nanoshell occurs is shown.

For the  $[r_1, r_2] = [15, 32]$  nm nanoshell, the behavior of the near field intensity enhancement as a function of core dielectric, shown in Figure 4-11A, is quite straightforward. For this nanoshell, the sphere and cavity plasmons interact weakly due to the low aspect ratio  $r_1/r_2 = 0.47$ . The enhancement on the outer surface of the nanoshell is only weakly dependent on the core dielectric. This can also be seen in the far field efficiencies shown in Figure 4-11E. Unlike the fields on the outer surface, the fields inside the core increases almost linearly with dielectric constant.

Phase retardation effects due to the spatial variation in the phase of the incident field over the particle and non-trivial propagation time of the electromagnetic field across the particle play a significant role in determining the optical response of the particles considered here. Increasing the core dielectric allows the bonding plasmon resonance to be tuned to longer wavelengths without changing the overall size of particle. As a result, the size of the nanoshell compared to the wavelength of light at the bonding resonance can be tuned. Consequently, retardation effects due to the variation of the incident field across the particle decrease in importance as the core dielectric is increased. Quantitatively, the relative size of the particle to the wavelength can be represented by the natural definition of the size parameter used in Mie theory  $x = ka = 2\pi r_2 / (\epsilon_m^{1/2} \lambda)$ , where  $\epsilon_m^{1/2} \lambda$  is the wavelength of light in the medium. From the peak wavelengths shown in Figure 4-11I for the  $[15, 32]$  nm nanoshell, the size parameter at the dipole resonance ranging from  $x = 0.27$  to  $0.23$  as the core dielectric is increased from  $\epsilon_c = 2$  to  $\epsilon_c = 16$ . This indicates that the nanoshell is small compared to the wavelength of light over the entire range of dielectrics and therefore phase retardation effects will be minimal. For the three larger nanoshells, the size parameter is significantly larger over

this same range:  $x = 0.35$  to  $0.26$  for the  $[30, 46]$  nm nanoshell,  $x = 0.38$  to  $0.27$  for the  $[40, 54]$  nm nanoshell, and  $x = 0.42$  to  $0.30$  for the  $[50, 65]$  nm nanoshell. Just like a radio antenna, the nanoshells only radiate efficiently when the size of the structure is significant compared to the wavelength. This allows the relative contribution of absorption and scattering to the overall extinction to be controlled. Tuning the plasmon resonance wavelength by varying  $r_1 / r_2$  for a fixed  $r_2$  allows some control over the relative absorption and scattering. However, this offers only limited control as varying the shell thickness itself changes the relative contribution of absorption and scattering and practical limitations on the shell thicknesses achievable using seeded growth techniques limit the tuning range available for a given core size. Tuning the plasmon resonance wavelength by varying the core dielectric is therefore quite attractive as it allows these difficulties to be overcome. For a  $[r_1, r_2] = [15, 32]$  nm nanoshell, the scattering efficiency (Figure 4-11E) is small compared to the absorption and almost vanishes for large  $\epsilon_c$ . This is exactly what is expected for a particle small compared to the wavelength at which the bonding dipole resonance occurs (Figure 4-11I), with  $x \leq 0.27$  over the entire range of dielectrics considered and decreasing with increasing core dielectric. For the  $[r_1, r_2] = [30, 46]$  nm nanoshell, the dipole plasmon resonance is shifted to longer wavelengths (Figure 4-11J) as compared to the  $[15, 32]$  nm nanoshell due to the larger aspect ratio  $r_1 / r_2 = 0.65$ . Nonetheless, the overall size has increased sufficiently that, for low dielectric constants, the nanoshell size is now significant compared to the wavelength ( $x = 0.35$ ). As a result, the scattering efficiency is significant, exceeding the absorption efficiency (Figure 4-11F) for  $\epsilon_c < 9.1$ . The behavior of the scattering, absorption, and extinction efficiencies as a function of core dielectric is no longer monotonic as a

function of core dielectric as was the case for a smaller nanoshell for two reasons. First, because an increase in the scattering cross section results in an increase in the rate at which energy is dissipated from the nanoshell, the plasmon is damped resulting in an increased linewidth and reduced peak intensity of the plasmon. This can result in an overall decrease in the extinction as scattering becomes stronger. The larger nanoshells follow a similar trend, with the absorption and scattering efficiencies crossing at similar sizes relative to the wavelength (size parameter of 0.30, 0.31 and 0.33 for the [30, 46] nm, [40, 54] nm, and [50, 65] nm nanoshells, respectively). At  $\epsilon_c = 16$ , the relative contribution of absorption and scattering to the overall extinction for the three larger nanoshells is quite similar to the smallest nanoshell at  $\epsilon_c = 2$  because the size parameter is nearly the same in these cases. A similar effect has previously been observed in multilayer Au-Silica-Au nanoshell structures. In this case, changing the intermediate silica layer thickness allowed the resonance wavelength to be tuned without varying the overall particle size, resulting in a variation in the relative contribution of absorption and scattering to the overall extinction.<sup>69</sup>

In addition to phase retardation, the relative absorption and scattering cross sections are controlled by the charge difference between the inner and outer surface of the Au shell and plasmon hybridization between the sphere and cavity plasmons. The higher permittivity of the Cu<sub>2</sub>O core allows it polarizes more strongly, reducing the charge on the inner surface of the Au shell. The increased imbalance of charge between the inside and outside surfaces of the shell generates a larger field across the metal. Since the metal is highly absorptive, this results in higher absorption efficiencies. The stronger absorption can also be understood in terms of plasmon hybridization. The high permittivity core

shifts the plasmon resonance of the cavity-like mode to lower energy resulting in an increase in the admixture of the cavity plasmons in the bonding mode since the energy of the sphere and cavity modes are closer.

#### **4.2 Conclusions**

We have engineered a plasmonic nanostructure, by utilizing a straightforward fabrication technique, consisting of a high permittivity semiconductor core encapsulated in a thin Au shell. The plasmon resonance of the Cu<sub>2</sub>O/Au nanoshells can be tuned from the visible to the NIR by simply modifying the core and shell dimensions. Compared to a dielectric core material such as SiO<sub>2</sub>, the optical response of Cu<sub>2</sub>O/Au nanoshells can be tuned farther into the NIR for equivalent nanoshell dimensions. This suggests that Cu<sub>2</sub>O/Au nanoshells would span a broader range of the spectrum compared to SiO<sub>2</sub>/Au nanoshells for smaller nanoparticle sizes. This property could be potentially useful in biomedical applications where smaller nanoparticle sizes resonant in the NIR are necessary. Altering the permittivity of the core material also allows optimization of the far field properties for specific applications. For photothermal applications such as cancer therapy and gene therapy Cu<sub>2</sub>O/Au nanoshells with their enhanced absorption efficiency would be more practical. On the contrary, for photoemission applications such as bioimaging and biological sensing SiO<sub>2</sub>/Au nanoshells with their high scattering efficiency would be more useful. In addition, the near field properties of Cu<sub>2</sub>O/Au nanoshells may tremendously impact the non-linear and excitonic response of Cu<sub>2</sub>O.

## Chapter 5. Profiling the Near Field of a Nanoshell with Raman-Based Molecular Rulers

Individual metallic nanoparticles and their assemblies have remarkably vivid optical properties that arise due to the direct excitation of their collective electronic, or plasmon, resonances by incident light. When illuminated at wavelengths within the linewidth of the plasmon resonance, an intense optical frequency evanescent field is excited at the nanoparticle surface. This near field, or fringing field, may be of significantly greater intensity than the incident optical wave that excited the nanostructure, a characteristic that gives rise to a range of physically interesting and technologically important phenomena. These include surface enhanced Raman scattering (SERS),<sup>8, 91-94</sup> surface plasmon resonance (SPR) sensing for detection of chemical and biomolecular species,<sup>62, 95, 96</sup> nanoscale lithography,<sup>97, 98</sup> even the photothermal destruction of cancer cells in biomedicine.<sup>43, 99</sup> Developing precise methods for the quantitative measurement of the spatial extent of this nanoscale optical field is of direct interest in the optimization of all these applications.

Previously reported methods for measuring the spatial extent of the fringing field on various nanoscale metallic structures have utilized fluorescence,<sup>100-105</sup> tip enhanced SERS,<sup>106</sup> and SPR shifts as spatially dependent signals in various geometries.<sup>107, 108</sup> These are indirect methods which have shown qualitative agreement with an anticipated spatial decay of the fringing field, but were performed without direct comparison to a known near field profile. Here we report a direct and self-consistent approach to mapping the

fringing field of a metallic nanoparticle which utilizes the surface enhanced Raman scattering (SERS) signals from specially designed bifunctional Raman-active molecular rulers adsorbed onto a nanoparticle surface. The measurement is performed on nanoshells, dielectric core-metallic shell nanostructures whose plasmon resonance frequency and near field optical properties are controlled by the inner and outer dimensions of the metallic shell layer to a quantitative degree of precision.<sup>35, 109</sup> When the plasmon resonance of a nanoshell is tuned to the excitation laser and Raman shifted wavelengths, strong SERS enhancements from individual nanoshells coated with a monolayer of Raman-active molecules can be obtained.<sup>30, 35</sup>

The spherical symmetry of nanoshells permits straightforward modeling of their electromagnetic near and far fields using Mie scattering theory. It has recently been observed that single nanoshell substrates give rise to SERS signal levels similar to those obtained from “hot spots”, the tiny junctions between metallic nanoparticles that produce enormous electromagnetic field enhancements across minute sample volumes.<sup>30, 110</sup> With nanoshells, this signal arises from a lower near field intensity over a far greater nanoparticle surface area, creating a much larger effective sensing volume.<sup>111, 112</sup> Therefore the development of a measurement technique for evaluating the SERS-specific near field profile is highly relevant in the design of future plasmonic SERS substrates which may have high intensity near field enhancements on open surfaces,<sup>113, 114</sup> a geometry far more convenient for large molecule or biosensing than nanoparticle junctions.

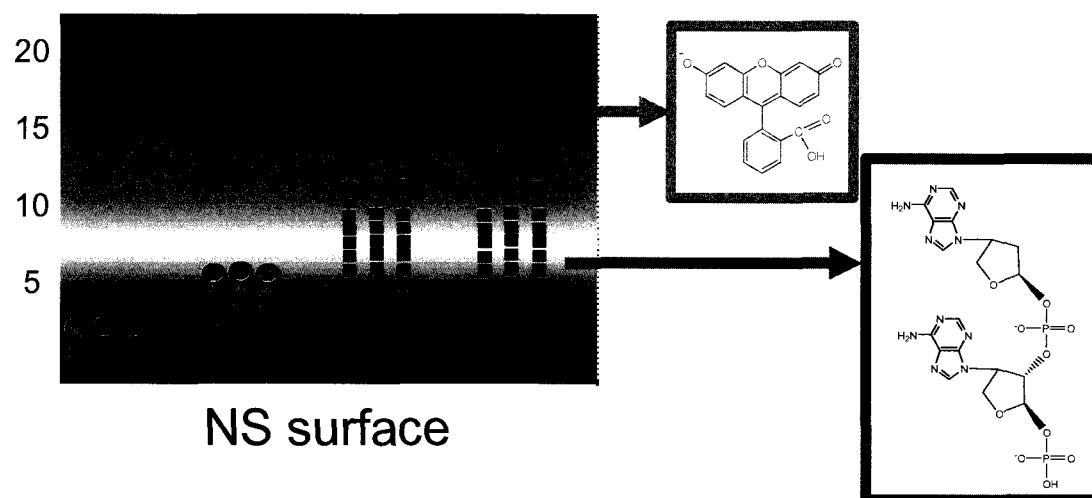


**Figure 5-1.** Schematic diagram showing the bifunctional Raman-active molecular rulers at varying distances from the nanoshell surface ( $y$ -axis). Both the terminal fluorescein and adenine strand moieties used as building blocks are shown. The SERS spectrum for each molecular component of the ruler provides an independent SERS spectrum dependent on the nanoparticle's near field, as described in text.

The bifunctional DNA-based adsorbate molecule that serves as the SERS-active molecular ruler in this experiment is shown in Figure 5-1. The molecular ruler consists of single-stranded DNA with a terminal fluorescein functional group. A thiol group at the opposite end of the molecule from the fluorescein terminus allows for attachment of the molecule to the Au surface. This molecular ruler provides two easily detected, independent SERS signals, one from the Stokes emission of the terminal fluorescein moiety and the other from the Stokes emission of the adenine groups of the DNA chain. As the length of the adenine chain is increased, the fluorescein group extends further from the Au surface, and its SERS signal decreases with growing distance from the nanoparticle surface. Simultaneously, as the adenine chain length is increased, the SERS signal from the constituent adenine groups of the chain increases as the adenine chain spans an increasing portion of the fringing field. Therefore, the fluorescein and adenine

moieties serve as two independent electromagnetic reporters on the same molecular ruler, each responding to the electromagnetic field at their respective resonant frequency.

Synthesis and optical properties of nanoshells have been discussed elsewhere in detail.<sup>17,</sup>

<sup>52</sup> To prepare the nanoshell substrates for the measurements, a saturation coverage of each of the various lengths of the fluoresceinated poly-adenine bifunctional molecular ruler was covalently attached via the thiol moiety onto the surfaces of nanoshells. In this set of experiments, thiolated ss-DNA consisting of 2, 6, 12, and 18 bases of adenine (Oligos etc., Wilsonville, OR for the 2-adenine base molecule and Integrated DNA Technologies, Coralville, IA for the 6, 12, and 18 base molecules) with a fluorescein terminal moiety was used. For all molecules the 5' thiol modification was attached via a 6 carbon methylene spacer to the poly-adenine chain and the 3' terminal fluorescein moiety was attached to the other end of the poly-adenine chain via a 6 carbon methylene spacer.

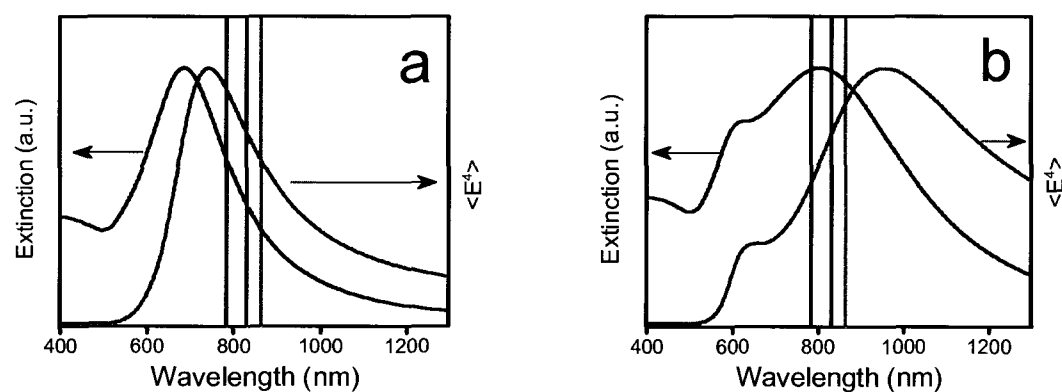


**Figure 5-2** Extinction spectra (black) and the calculated surface average  $\langle |E|^4 \rangle$ -field spectrum (red) for the two sizes of nanoshells. (a)  $[r_1, r_2] = [43, 58]$  nm nanoshells (b)  $[r_1, r_2] = [70, 91]$  nm nanoshells. The excitation laser wavelength at 785 nm (purple vertical line) and the emission peak for adenine (red vertical line) and fluorescein (green vertical line) analyzed are shown.

Nanoshells of two different geometries and plasmon resonant properties were used to test the validity of this experimental approach. Figure 5-2 shows the far field extinction spectra and the surface averaged near field spectra  $\langle |\mathbf{E}|^4 \rangle$  calculated using Mie scattering theory at a distance of 0.1 nm above the nanoparticle surface for the two sets of nanoshells synthesized for these experiments. One set of nanoshells (Figure 5-2(a)) was designed with inner and outer shell radii of dimensions  $[r_1, r_2] = [43, 58]$  nm such that the near field maximum of the nanoshells was tuned to the excitation laser at 785 nm. The other set of nanoshells (Figure 5-2(b)) was designed with  $[r_1, r_2] = [70, 91]$  nm such that the far field extinction was tuned to the excitation laser.

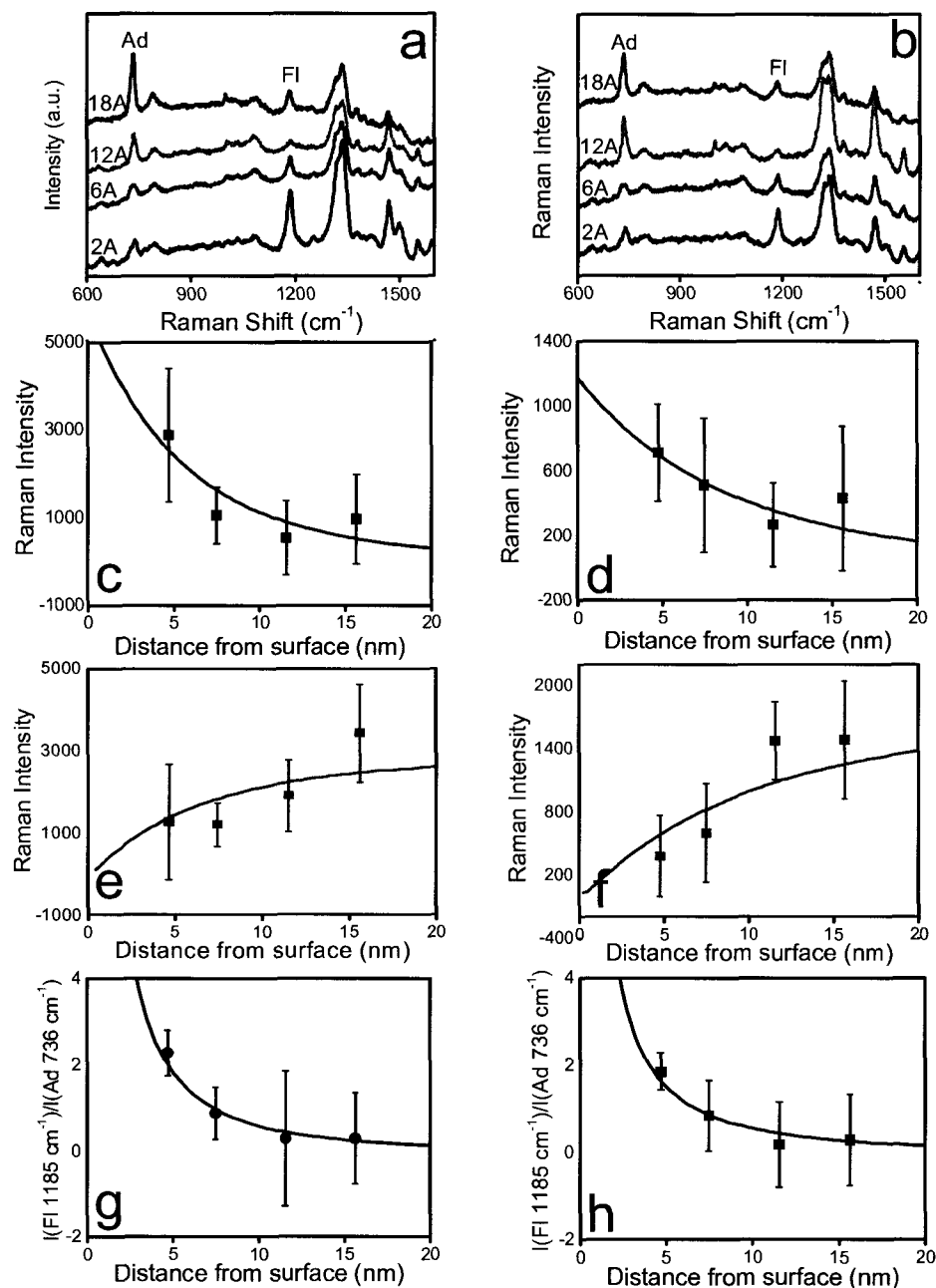


**Figure 5-3** (a) SERS spectra for DNA-fluorescein adsorbate layer on  $[r_1, r_2] = [43, 58]$  nm nanoshells and (b) same as (a) but for  $[r_1, r_2] = [70, 91]$  nm nanoshells. Spectra correspond to DNA strands of 2, 6 12 and 18 adenines, respectively. (c) SERS intensity of  $1185 \text{ cm}^{-1}$  fluorescein peak (counts / 60 s). (■): Experimental values; solid lines: theoretically calculated values for  $[r_1, r_2] = [43, 58]$  nm nanoshells (d) same as (c) for  $[r_1, r_2] = [70, 91]$  nm nanoshells (counts/30s) (e) same as (c) for  $736 \text{ cm}^{-1}$  adenine peak (f) same as (d) for  $736 \text{ cm}^{-1}$  adenine peak. (g) The ratios of SERS intensities ( $I(\text{fluorescein}@1185 \text{ cm}^{-1})/I(\text{adenine}@736 \text{ cm}^{-1})$ ) as a function of distance from the nanoshell surface on  $[r_1, r_2] = [43, 58]$  nm nanoshells. (■): Experimental values; solid lines: theoretically calculated values (h) same as (g) for  $[r_1, r_2] = [70, 91]$  nm nanoshells.

The bifunctional molecular rulers for each of the DNA chain lengths were covalently bound to the surfaces of the two types of nanoshells, and the SERS spectrum was acquired. In this way, a sequence of SERS spectra for varying adenine chain length was obtained for each nanoshell geometry, and is shown in Figure 5-3(a,b). The Raman experiments were performed on functionalized Au nanoshells suspended in buffered aqueous solution (pH 9) using a Renishaw inVia microRaman spectrometer with an excitation laser wavelength at 785 nm. At this pH, thiolated ss-DNA has been observed to extend upright when bound to metallic nanoparticle and film surfaces.<sup>115</sup> The spectra were collected using a 63x water immersion objective with a 0.9 N.A., over a rectangular area approximately  $30\ \mu\text{m} \times 3\ \mu\text{m}$ . For each sample 12 spectra were collected from different areas of the sample. In both sets of spectra, the ring breathing mode of adenine<sup>116-119</sup> at  $736\ \text{cm}^{-1}$ , and the C-CH bending mode of the fluorescein<sup>120</sup> at  $1185\ \text{cm}^{-1}$  are clearly observable. The remaining peaks in the spectra can be attributed to adenine or fluorescein but are not used in the present analysis because either the adenine and fluorescein peaks strongly overlap (e.g. the double peak at  $1335\ \text{cm}^{-1}$ ) or the peaks are not clearly observed in all spectra.

The intensities of the  $1185\ \text{cm}^{-1}$  mode of fluorescein and the  $736\ \text{cm}^{-1}$  mode of adenine, as a function of adenine chain length, are shown in Figure 5-3(c,d). Here the experimental SERS intensities of the fluorescein peak are plotted as a function of distance from the nanoparticle surface, where the distances from the nanoshell surface along the  $x$ -axis are determined for a stretched configuration of DNA.<sup>115, 121</sup> The theoretical fit (solid line) is the SERS response calculated using Mie scattering theory. The nanoparticle surface-averaged SERS signal is calculated as

$$G_{SERS} = \left\langle \left| E_{incident}(\omega_L) + E_{NS}(\omega_L) \right|^2 \left| E_{NS}(\omega_S) \right|^2 \right\rangle, \quad (5-1)$$

where  $E_{incident}(\omega_L) \ll E_{NS}(\omega_L)$ , are the incident and near field enhancement at the laser excitation frequency  $\omega_L$ , and  $E_{NS}(\omega_S)$  is the field enhancement at the respective Stokes mode of the molecule (as indicated in Figure 5-2). The average is over the nanoparticle surface. The analogous Stokes modes for adenine are also extracted from the SERS spectra, and are shown in Figure 5-3(e,f) for both nanoshell geometries. In this case, the theoretical curve is also obtained using Mie scattering theory, and consists of the integrated surface-averaged signal

$$\int_{r_2}^{r_2+d} G_{SERS} dr' \quad (5-2)$$

as a function of distance  $d$  from the nanoparticle surface, directly analogous to the sum of the SERS signals from each adenine moiety at each respective chain length. The error bars in Figure 5-3(c-h) are based on the standard deviation in peak heights from a set of 12 independent measurements on each nanoshell geometry. The spread in measurement values is due in part to a variation in the number of DNA molecules adsorbed on the nanoshells,<sup>122</sup> as well as a variability in the number of nanoshells in the beam during each measurement, and variations in molecular conformation of the DNA tether. Figure 5-3(a,b) are an average of the spectra collected for each sample.

A ratio of the fluorescein  $1185 \text{ cm}^{-1}$  and adenine  $736 \text{ cm}^{-1}$  Stokes mode intensities provides a measurement of the near field at a nanoshell surface that is independent of variations in nanoparticle surface coverage by the bifunctional DNA molecules since both functional groups are present on each molecule to a high degree of purity. The ratio of these signals is shown in Figure 5-3(g,h). Here the data are in excellent agreement with

the ratio of the corresponding fluorescein  $1185\text{ cm}^{-1}$  and adenine  $736\text{ cm}^{-1}$  theoretical curves: Figure 5-3(g) corresponding to Figure 5-3(c) / Figure 5-3(e), and Figure 5-3(h) corresponding to Figure 5-3(d) / Figure 5-3(f).

The  $G_{SERS}$  used to fit the fluorescein SERS profile in Figure 5-3(c,d) (Eq. 5-1), the integral in Figure 5-3(e,f) (Eq. 5-2), and the SERS intensity ratios in Figure 5-3(g,h), are plotted directly in Figure 5-4 for both sizes of nanoshell substrates:  $[r_1, r_2] = [43, 58]$  nm (Figure 5-4(a)) and  $[r_1, r_2] = [70, 91]$  nm (Figure 5-4(b)).  $G_{SERS}$  for the nanoshell with its near field maximum tuned to the excitation laser (Figure 5-4(a)) is almost twice as large as  $G_{SERS}$  for the nanoshells with the far-field extinction tuned to the excitation laser (Figure 5-4(b)). The inset plots show the surface enhanced field distribution evaluated 0.1 nm above the nanoshell surface at the excitation frequency  $\omega_L$  (left) and Raman shifted frequency  $\omega_S$  (right) in both Figure 5-4(a) and (b). In Figure 5-4(a), the field distribution at the excitation frequency appears to be large compared to the field distribution at the Raman shifted frequency, correlating well with the near field calculated for a nanoshell of these dimensions (Figure 5-2(a)). A similar correlation between the near field intensity and the predicted SERS response is seen for the second set of nanoshells (Figures 5-2(b) and 5-4(b)). The difference in spatial distribution of the near field on the nanoshell surface which is seen in parts a and b of Figure 5-4 is due to the larger particle size analyzed in Figure 5-4(b).

Interestingly, although the surface average SERS response for the smaller  $[r_1, r_2] = [43, 58]$  nm nanoshells is almost twice as large as the bigger  $[r_1, r_2] = [70, 91]$  nm nanoshells (Figure 5-4), the overall SERS signal measured from the bigger shells is

much larger. This can be explained by considering that the overall surface area available for attaching analyte molecules is larger for the bigger nanoshells. Thus for ensemble measurements over a large number of nanoshells, there is an optimum nanoshell size determined by achieving the largest near-field enhancements and maximizing the overall surface area available for attachment of the Raman active molecule.

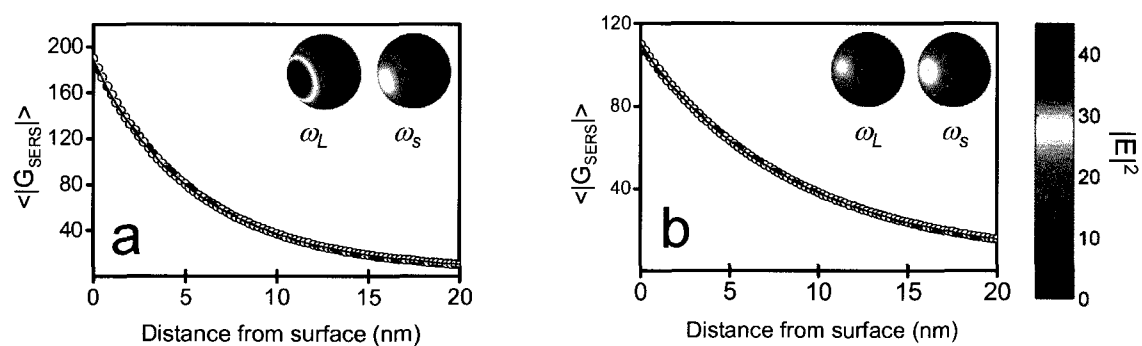


**Figure 5-4** Surface average  $\langle |G_{SERS}| \rangle$  as function of distance from nanoparticle surface for (a)  $[r_1, r_2] = [43, 58]$  nm nanoshells and (b)  $[r_1, r_2] = [70, 91]$  nm nanoshells. Circles ( $\circ$ ) are calculated using Mie theory, solid line ( $\text{—}$ ) is a fit to a dipole model, and dashed line ( $\text{- -}$ ) is a fit to an exponential decay. **Inset:** The field intensity enhancement at the excitation and emission wavelength for the two nanoshells. The intensity color bar is the same for all the surface plots.

The spatial profile of  $G_{SERS}$  is shown in Figure 5-4 for both nanoshell geometries. This dependence agrees with a decay profile based on the radiating fields of a simple dipole,<sup>123</sup> however, unlike previous studies that focused on small ( $\sim 10$  nm) radius metallic structures, here the quasistatic response ( $1/r^3$ ) alone is insufficient to describe the response of the nanoparticle substrates used here.<sup>105, 124</sup> For nanoshells in this size range, it is necessary to include terms in the near field slower than  $(r-r_0)^{-3}$ . Retaining the near field, induction, and radiation terms from the expression for a classical dipole radiator,  $G_{SERS}$  can be expressed in the following form:

$$G_{SERS} \propto \frac{a}{(r-r_0)^4} + \frac{b}{(r-r_0)^8} + \frac{c}{(r-r_0)^{10}} + \frac{d}{(r-r_0)^{12}} \quad (5-3)$$

where  $r_0$  is an effective distance from the center of the nanoshell. It is important to note that for nanoparticles of this size regime, the SERS enhancement is also well approximated by an exponential decay:

$$G_{SERS} \propto e^{\frac{-(r-r_2)}{L_{SERS}}} \quad (5-4)$$

where  $(r-r_2)$  is the distance above the nanoparticle surface. The simple exponential profile would be rigorously correct for the case of a macroscopic flat film. The exponential approximation is also shown, as an overlay, in Figure 5-4. The exponential approximation is in even better agreement with the larger radius nanoshell, which better approximates an infinite film (i.e. a thin film is a nanoshell of infinite radius). We can use the simple exponential fit to parameterize and define a unique  $1/e$  length,  $L_{SERS}$ , characteristic of the SERS signal profile for each nanoparticle geometry. Based on this analysis we determine that  $L_{SERS}$  for the  $[r_1, r_2] = [43, 58]$  nm nanoshell substrate is 6.2 nm and for the  $[r_1, r_2] = [70, 91]$  nm nanoshell substrate is 9.7 nm.

In summary, this work demonstrated a SERS-based nanoscale metrological approach for mapping the near field at the surface of a plasmon resonant nanostructure. Quantitative agreement was obtained between the experimental SERS profile measured using a bifunctional DNA molecular ruler and the near field profile of the nanoparticle substrate, for nanoshells of two different sizes and near field resonant properties. The experimental measurements indicate that for this type of SERS substrate, an effective sensing volume can be defined which includes an effective  $1/e$  distance,  $L_{SERS}$ , above the nanoparticle

substrate surface. Furthermore, signals are easily detectable from Raman-active functional groups positioned at distances of ~10 nm or more from the surfaces of the nanoparticles. This methodology provides a metrological protocol that could be applied generally to designing new plasmonic substrates; in particular, it could be extremely useful for characterizing new geometries that combine large field enhancements with open, exposed surface areas.<sup>113,114</sup> The methodology presented is optimal for the spectral fingerprinting of biomolecules or larger, more complex biological structures.

## Chapter 6. Nanoscale Control of Near-Infrared Fluorescence Enhancement Using Au Nanoshells

Metal enhanced fluorescence is highly relevant for understanding the fundamental physical phenomena contributing towards emission enhancement as well as for developing technologies based on these nanoparticle-fluorophore assemblies. Metal-fluorophore interaction is a sensitive function of the distance between them. While at short distances ( $\leq 4$  nm) fluorescence quenching is inevitable, at an optimum distance from the nanoparticle surface strong plasmon-enhanced fluorescence can be observed.<sup>125-</sup>

<sup>127</sup> The enhancement will decrease as the fluorophore-metal distance continues to increase until the metal's optical field does not affect the fluorophore emission properties. In this chapter, we have qualitatively measured the fluorescence of NIR fluorophore, Indocyanine Green (ICG), as a function of distance from the Au nanoshell surface and determined the optimum distance where a maximum enhancement of 50X is achieved. Beyond the optimal distance from the nanoshell surface, the emission and hence the quantum yield decreases. All nanoparticle synthesis, characterization and experimental fluorescence spectra were obtained by Rizia Bardhan. Nathaniel K. Grady contributed towards theoretical analysis and discussion. Reproduced with permission from Rizia Bardhan, Nathaniel K. Grady, Naomi J. Halas, *Small*, **2008**, 4, 1716–1722. Copyright 2008 Wiley-VCH Verlag GmbH & Co. KGaA, Weinheim.

Water-soluble and biocompatible NIR emitting fluorescent molecules have provided an important new tool for biomedical imaging<sup>128</sup> and for the detection of disease markers *in vivo*. The relatively large penetration depth of NIR light in most biological media offers the potential for imaging deeply into the organs and soft tissues of living systems. This

property is aided by the use of NIR-excitable fluorescent molecules as agents for contrast enhancement.<sup>129</sup> The goal of designing and synthesizing NIR fluorescent molecules with large absorption coefficients and high quantum yields that are also safe for physiological environments is quite challenging, due at least in part to the complex synthetic routes required for these large, complex molecules.<sup>130, 131</sup> A highly promising alternative approach is to enhance the emission of currently available NIR fluorescent molecules by combining them with appropriately designed metallic “nanoantennas”. For example, ICG, currently the only FDA-approved, commercially available NIR emitting dye, is used extensively as an exogenous fluorescent marker in clinical imaging applications<sup>132</sup> such as the diagnosis of cardiac and hepatic function,<sup>133</sup> measurement of plasma volume,<sup>134, 135</sup> ophthalmic scanning laser angiography<sup>136, 137</sup> and optical tomography.<sup>138</sup> However, ICG is a relatively weak fluorophore with a quantum yield of only 1.3 %, <sup>139</sup> and toxicity limits the maximum concentration appropriate for clinical use. Enhancing the quantum efficiency of ICG significantly without compromising its biocompatibility will lead to significant improvements in the detection limits of NIR fluorescence-based imaging, enabling, for example, the detection of significantly smaller tumor volumes than is currently possible. Recently, we have shown that the fluorescence of ICG can be significantly enhanced when the fluorescent molecules are positioned near Au nanoshells, when the plasmon resonance of the nanoshell is tuned to the emission wavelength of the fluorophore.<sup>89</sup> Fluorescence enhancements as large as 50 were achieved, for a nanoshell designed with a significant scattering cross section at that wavelength. In this system the ICG molecules act like local sources that feed the optical “nanoantenna”, which then transmits their light efficiently into the nanoparticle far field.

Noble metal nanoparticles and nanostructures exhibit unique, remarkably vivid optical properties due to excitation of their surface plasmons by incident light. Plasmon excitation results in significantly enhanced local fields at the nanoparticle surfaces, which give rise to fundamentally interesting phenomena and technologically important applications.<sup>125, 140-142</sup> Noble metal nanoparticles are known to significantly enhance the emission rates of vicinal fluorophores by decreasing their radiative lifetime, thereby increasing their quantum yield.<sup>127, 143, 144</sup> The photostability of fluorophores can also be increased in this manner. Enhancing the emission of molecular fluorophores is a highly useful strategy for improving detection sensitivity and selectivity in many emerging applications such as DNA screening<sup>145</sup> and single molecule detection,<sup>146</sup> in addition to image enhancement.<sup>147</sup> Consequently, designing and developing nanoparticle-molecule complexes to enhance molecular fluorescence is of broad interest and general importance.

The influence of metallic surfaces (and subsequently metal nanoparticles) on fluorescence emission and molecular excited-state lifetimes has been a topic of interest since the pioneering work of Drexhage.<sup>67, 125, 126, 148</sup> The lifetime of a molecular excited state varies as a function of distance from the surface of a noble metal due to a modification of the enhanced absorption (due to the near field), radiative decay rate (due to the modified photon density of states near the metal surface) and nonradiative decay channels (due to energy dissipation).<sup>149, 150</sup> While fluorescence from a molecule directly adsorbed onto a metal surface or nanoparticle is quenched, for a molecule positioned a few nanometers from the metal, it can be strongly enhanced. As the fluorophore-metal distance is increased, longer-range interactions between the molecule and the metal can lead to oscillatory enhancement and quenching behavior as a function of separation

distance for bulk metals. For large separation distances from a bulk metal or metallic nanoparticle, the molecular fluorescence returns to its unperturbed value.<sup>151, 152</sup>

In this study, we have investigated the fluorescence enhancement of ICG molecules as a function of distance from the surface of Au nanoshells (NS). The distance between ICG molecules and the NS surface is controlled by varying the thickness of silica shell spacer layers grown on the nanoshell surface. We observe a fluorescence enhancement of 50 when ICG molecules are spaced 7 nm from the Au nanoshell surface, which decreases with increasing distance of the molecule from the nanoshell surface. Au nanoshells are excellent plasmonic nanostructures for these experiments for several reasons. First, their plasmon resonances can be controllably tuned across the visible and infrared region of the spectrum by modification of their core and shell dimensions.<sup>17, 39</sup> Their relative absorption and scattering cross sections can also be controlled by varying total nanoparticle size.<sup>54, 89</sup> The spherical symmetry provides a highly uniform geometry for studying phenomena requiring a systematic variation of molecule-metal nanoparticle distance. Growing a silica shell spacer layer around the Au nanoshell core, then binding molecules onto the silica layer, is a controllable and reproducible technique for positioning fluorophores at well controlled, nanometer-scale distances from the nanoparticle surface over the length scales appropriate for modifying molecular fluorescence. The chemistry also imparts a robust, chemically inert, and biocompatible surface for the nanoparticle.<sup>153</sup> This approach allows us to measure the spatial extent of the fluorophore – nanoparticle interaction quantitatively over a length scale relevant to fluorescence enhancement.

## 6.1 Fabrication of Nanoshell-ICG Conjugates

### 6.1.1 *NS@SiO<sub>2</sub> fabrication:*

Au-NS with  $76 \pm 3$  nm radii were fabricated by seed-mediated electroless plating of Au onto silica spheres as previously reported.<sup>25</sup> Briefly, monodisperse silica nanospheres of  $60 \pm 2$  nm radii were synthesized by the hydrolysis of TEOS in basic solution via the Stöber method<sup>154</sup> and functionalized with (3-aminopropyl) triethoxysilane (APTES, Sigma–Aldrich) overnight. These functionalized nanoparticles were decorated with small gold colloid (2–3 nm) prepared by the method reported by Duff et al.<sup>87</sup> A continuous gold shell was grown by reducing gold from a 1% solution of H<sub>2</sub>AuCl<sub>4</sub> onto the attached small colloid in the presence of formaldehyde.

Silica epilayers of varying thicknesses were grown around the Au-NS by modifying a protocol previously described by Evanoff et al.<sup>107</sup> Briefly, 4 mL of concentrated Au-NS ( $\approx 10^9$  particles mL<sup>-1</sup>) aqueous solution was added to 40 mL absolute 200-proof ethanol (Aaper Alcohol and Chemical Co.) at room temperature under constant stirring. 500  $\mu$ L of 30% ammonium hydroxide (Sigma–Aldrich) and appropriate amounts (6  $\mu$ L to 70  $\mu$ L) of tetraethylorthosilicate (TEOS, Sigma–Aldrich) was added to the reaction mixture simultaneously. Different amounts of TEOS were added to control the silica layer thickness surrounding the nanoshell core. The reaction was allowed to proceed at room temperature under vigorous stirring for 40 minutes and then allowed to age without agitation for 24 h at 4° C. The silica coated Au-NS (Au-NS@SiO<sub>2</sub>) nanoparticles were centrifuged and washed several times followed by resuspension in 10 mL water.

### 6.1.2 ICG Binding to NS@SiO<sub>2</sub> Nanoparticles:

ICG molecules were adsorbed onto the NS@SiO<sub>2</sub> by a two step procedure. (1) 1 mg ICG was mixed with 500  $\mu$ L degassed 200 proof ethanol and 100  $\mu$ L APTES was subsequently added and the mixture was stirred for 8 hrs at room temperature. (2) The APTES-ICG mixture was added to the NS@SiO<sub>2</sub> nanoparticles dispersed in ethanol and stirred for 24 hours at room temperature. The ICG bound nanoparticles were centrifuged in microcentrifuge tubes in small aliquots of 1 mL for 5 minutes at 280 rcf to remove unbound ICG molecules. Absorbance of the supernatant was monitored to account for unbound dye and we determined that  $\sim$  400 nM ICG molecules were bound to the NS@SiO<sub>2</sub> nanoparticles. ICG molecules were bound to silica nanospheres similarly and  $\sim$  400 nM ICG were attached to the silica nanospheres as well. The final nanoparticle solutions were redispersed in water and stored at 4 °C. Fluorescence measurements of ICG molecules adsorbed on NS@SiO<sub>2</sub> nanoparticles and silica nanospheres were obtained in solution with  $10^7$  particles/ mL.

## 6.2 Characterization of Nanoshell-ICG Conjugates

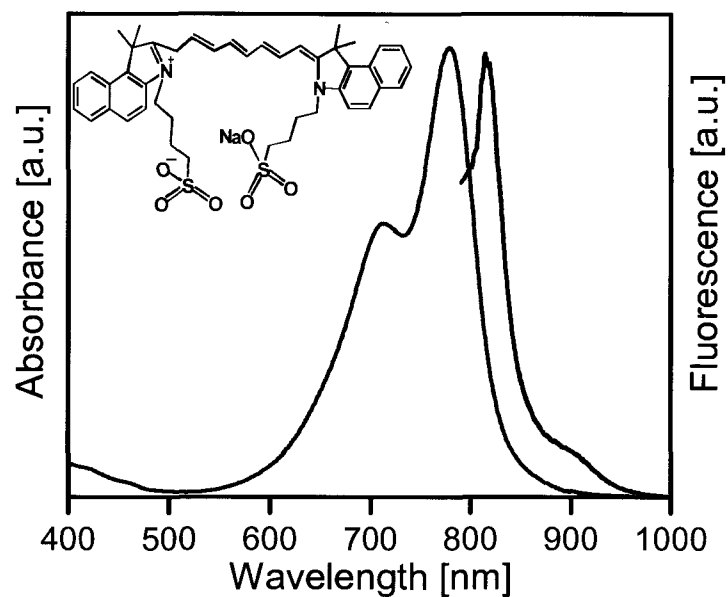


**Figure 6-1** Absorption–emission spectra ( $\lambda_{\text{max-Ab}} = 780 \text{ nm}$  and  $\lambda_{\text{max-Em}} = 820 \text{ nm}$ ) and chemical structure (inset) of ICG.

The nanoparticles were characterized by obtaining transmission electron microscope (TEM) images using a JEOL JEM-2010 TEM, and absorption measurements using a Varian Cary 5000 UV-Vis-NIR spectrometer. Fluorescence emission spectra were obtained using Jobin Yvon Spex Fluorolog 3 and the samples were excited at 785 nm. The absorption-emission spectrum and chemical structure of ICG (Figure 6-1), shows that ICG, a negatively charged tricyanin dye, strongly absorbs at 780 nm and emits at 820 nm. The presence of the charged sulfonate groups increases the solubility of ICG in aqueous media and minimizes significant ground-state aggregation, a phenomenon commonly observed in carbocyanine-type dyes.<sup>155</sup>

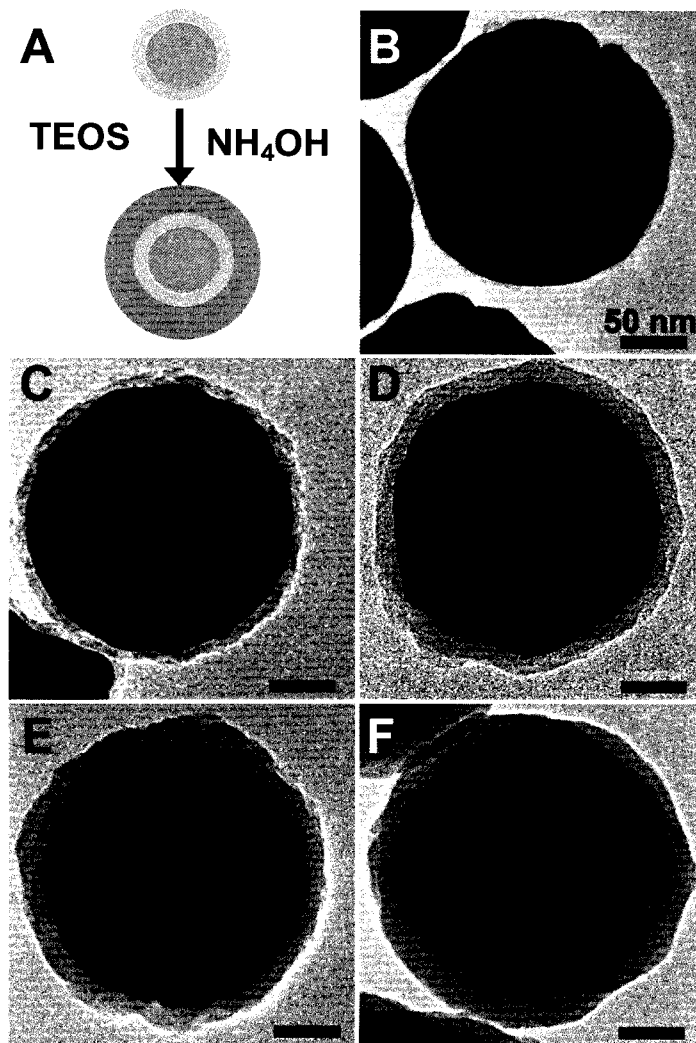


**Figure 6-2** (A) Schematic diagram of fabrication procedure, and TEM micrographs (B – F) of NS coated with varying thicknesses of silica epilayers (B)  $7 \pm 2$  nm (C)  $13 \pm 2$  nm (D)  $21 \pm 3$  nm (E)  $30 \pm 3$  nm (F)  $42 \pm 3$  nm. Scale bar is 50 nm for all TEM images.

The fabrication procedure of NS@SiO<sub>2</sub> nanoparticles is illustrated in Figure 2.2A. TEM micrographs of NS coated with different thicknesses of SiO<sub>2</sub> are shown in Figure 2.2B – 2F, where the thickness of the silica shell was varied from 7 – 42 nm. The NS@SiO<sub>2</sub> nanoparticles range from  $166 \pm 3$  nm in diameter to  $236 \pm 4$  nm where the silica thickness was controlled by concentration of tetraethylorthosilicate (TEOS) after alkaline initiation.

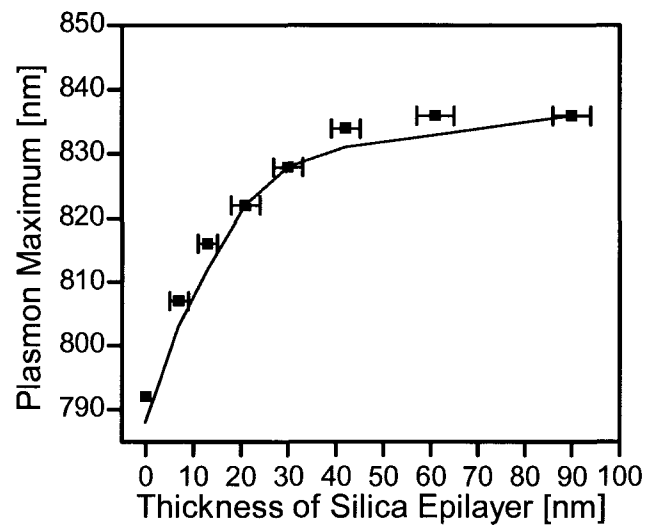


**Figure 6-3** Observed shift in the plasmon resonance peak with increasing thickness of silica layer surrounding the NS. (■) Experimental, and (—) calculated values for NS [r1, r2] = [60, 76] nm and NS@SiO<sub>2</sub> nanoparticles, with 7 ± 2 nm, 13 ± 2 nm, 21 ± 3 nm, 30 ± 3 nm, 42 ± 3 nm, 61 ± 4 nm, and 90 ± 4 nm thick silica epilayers are shown.

The plasmon resonance of the NS nanoparticles shifts to longer wavelengths as the silica layer thickness is increased. The experimentally obtained plasmon resonance frequencies as a function of silica layer thickness are compared directly to theoretical values calculated using Mie Theory for a concentric, three-layer, SiO<sub>2</sub>-Au-SiO<sub>2</sub> spherical nanoparticle (Figure 6-3). The plasmon redshift occurs due to the presence of the silica layer because of the higher refractive index of silica relative to water. The increasing thickness of the silica epilayer surrounding the NS screens the electron oscillation in the metal, decreasing the plasmon energy.<sup>156</sup> A redshift in the plasmon resonance peak from 790 nm (without silica shell layer) to 834 nm (with 60 nm silica shell layer) is observed, with the plasmon shift remaining constant for the thicker silica shell layers. This behavior indicates that changes to the local dielectric environment beyond a certain distance from the surface do not apparently affect the surface plasmons of the NS nanoparticles.<sup>107</sup> However, the silica layer thicknesses used in this experiment do not extend to the longer

length scale where oscillatory behavior of the SPR shift with increasing dielectric layer thickness has been reported.<sup>95</sup> The experimentally obtained values of the plasmon resonance wavelength shown in Figure 6-3 correlate very well with the theoretically obtained values. The linewidth of the plasmon peak of these nanostructures allows good overlap with the ICG absorption-emission profile for all the NS@SiO<sub>2</sub> nanoparticles synthesized for this experiment.

### 6.3 Experimental Fluorescence Enhancement

A schematic of ICG adsorption on the NS@SiO<sub>2</sub> nanoparticles through APTES surface functionalization, and subsequent fluorescence emission, is illustrated in Figure 6-4A. The ICG molecules are adsorbed onto the silica surface of the nanoparticle electrostatically. To quantify the fluorescence enhancement due to the silica coated nanoshells, ICG bound in the same manner to silica nanospheres (radius  $60 \pm 2$  nm) was used as a control sample. Comparison of the fluorescence of ICG adsorbed to silica-coated nanoshells vs. ICG on silica nanoparticles, rather than ICG in solution, allows us to examine the fluorescence enhancement process for molecules in equivalent chemical environments. The fluorescence spectra of ICG bound to silica ( $\lambda_{\text{max}} = 810$  nm) at varying distances from NS surface, as determined by the silica spacer layer, is shown (Figure 6-4B).

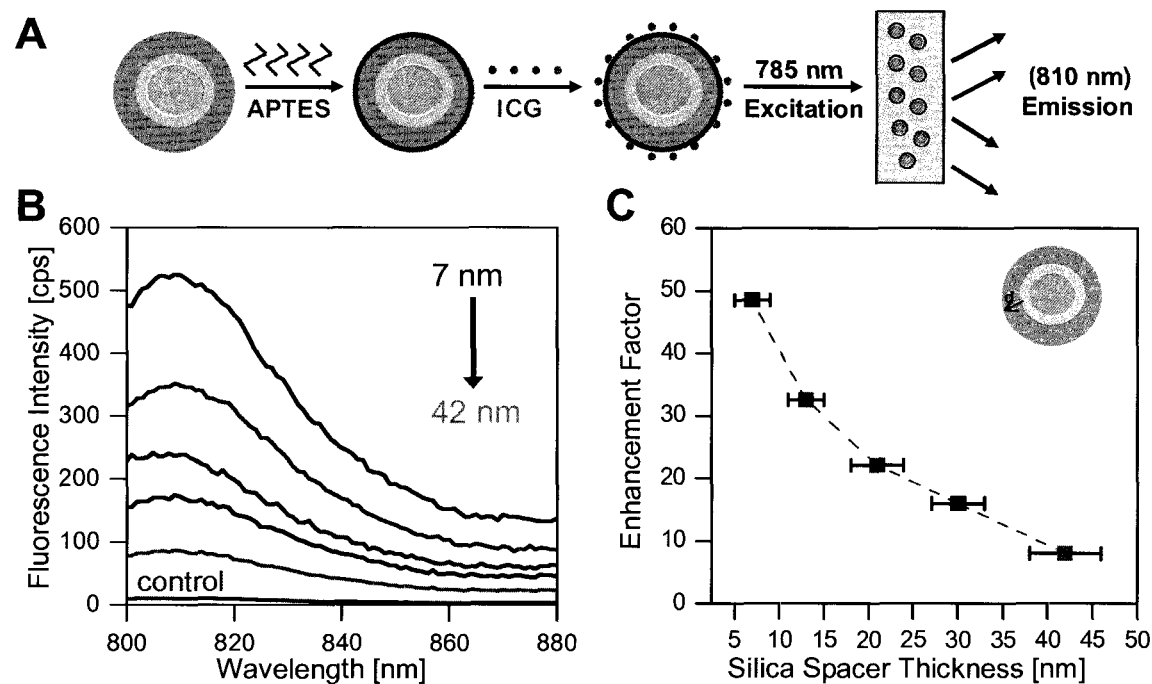


**Figure 6-4** (A) Schematic diagram of ICG conjugation on NS@SiO<sub>2</sub> nanoparticles, excitation and observed emission. (B) Fluorescence spectra of ICG conjugated at various distances from the NS surface. (—) Emission spectrum of control, ICG deposited on silica nanospheres is also included. (C) Fluorescence enhancement factor of ICG conjugated on NS@SiO<sub>2</sub> nanoparticles relative to silica nanospheres is shown as a function of thickness of silica layer surrounding the NS (color coordinated with reference to panel B).

The fluorescence spectra were collected under identical excitation and detection conditions, allowing direct comparison of the various nanoparticle-ICG complexes. The concentration of ICG molecules was maintained at  $\sim 400$  nM in each of the nanoshell and silica nanoparticle solutions used in the deposition of ICG onto the nanoparticle surfaces. Based on our deposition protocol, near-saturation coverage of ICG on the nanoparticle surfaces is likely, corresponding to nominally  $10^3$  ICG molecules per nanoparticle, increasing as nanoparticle size (and therefore surface area) is increased. A maximum enhancement of  $50\times$  is achieved relative to ICG molecules adsorbed on silica nanospheres for a silica spacer layer of  $7 \pm 2$  nm on the nanoshell surface. As the thickness of the silica spacer layer ( $13 \pm 2$  nm,  $21 \pm 3$  nm,  $30 \pm 3$  nm,  $42 \pm 3$  nm) was

increased, the fluorescence enhancement decreased, with the lowest enhancement factor of 7 observed for the largest spacer layer. This distance-dependent decay of the fluorescence enhancement is shown in Figure 6-4C as a function of silica layer thickness.

#### 6.4 Calculated Fluorescence Enhancement

The Au nanoshells influence ICG emission by a combination of two processes: absorption enhancement via the high intensity nanoparticle near field, and radiative rate enhancement, which increases its quantum yield.<sup>89</sup> Since the nanoparticle complexes used in this study have spherical symmetry, their properties can be calculated quite straightforwardly using Mie theory. In particular, both the near field enhancement and the radiative rate enhancement of molecules near the nanoshell surface can be calculated for this spherical geometry.<sup>31</sup> To obtain the near field enhancement, the electromagnetic fields around and within the particle are expressed in terms of a spherical harmonic basis set and the scattering is obtained in response to an incident plane wave.<sup>15</sup> To evaluate the radiative rate enhancement, a similar procedure is followed, except that the plane wave excitation is replaced with a point dipole adjacent to the nanoparticle. The far-field Poynting vector is then integrated over all angles and compared directly to the amount of energy radiated by the same dipole in free space. This theoretical model agrees very well with the distance dependence of the fluorescence enhancement we have observed (Figure 6-5A). We will now examine the relative contribution of these processes in more detail.

Emission from a fluorophore is experimentally quantified in terms of its quantum yield ( $Q_o$ ) and lifetime ( $\tau$ ). Intrinsically, these processes are best described in terms of the radiative emission rate ( $\Gamma$ ) and non-radiative decay rate ( $k_{nr}$ ). The quantum yield is then

the relative likelihood that the excited molecule relaxes following a radiative decay pathway:

$$Q_0 = \Gamma / (\Gamma + k_{nr}) \quad (6-1)$$

While the observed lifetime is simply the inverse of the total decay rate of the excited state:

$$\tau_0 = (\Gamma + k_{nr})^{-1} \quad (6-2)$$

For most dye molecules, including ICG, these parameters are highly dependent on local environment.<sup>157</sup> For ICG adsorbed onto silica-coated NS and ICG on solid silica nanospheres, we can assume that the intrinsic radiative and non-radiative decay rates of ICG are the same for these equivalent environments. When a sample of molecules with absorptivity  $\epsilon$  is excited with light of intensity  $I_{exc}$ , the total amount of energy absorbed is simply  $I_{exc} \cdot \epsilon$ . The quantum yield determines what portion of this energy is reemitted as fluorescence; therefore, the observed emission intensity is

$$I_o = I_{exc} \cdot \epsilon \cdot Q_0. \quad (6-3)$$

In the presence of the Au-NS, the enhanced local field will increase the amount of light absorbed by the molecule. The surface average of the near field intensity enhancement,  $\langle |\mathbf{E}|^2 \rangle$ , can be calculated directly using Mie theory, leading to a fluorescence emission of  $(\langle |\mathbf{E}|^2 \rangle \cdot I_{exc}) \cdot \epsilon \cdot Q_0$ . However, this is only half of the process. Electromagnetic coupling between the fluorophore and the Au-NS plasmons at the emission wavelength increases the radiative decay rate of the molecule by a factor  $\gamma_r$ , resulting in an effective radiative decay rate  $(\gamma_r \cdot \Gamma)$ . Due to the spherical symmetry of this system, this can also be evaluated

using Mie theory following the method in Gibson et al.<sup>31</sup> This results in a decrease in lifetime and an increase in quantum yield:

$$Q_{NS} = \gamma_r \Gamma / (\gamma_r \Gamma + k_{nr}) \quad (6-4)$$

and

$$\tau_{NS} = (\gamma_r \Gamma + k_{nr})^{-1}. \quad (6-5)$$

Because the chemical environment is unchanged from the reference sample and quenching is not observed, we assume that  $k_{nr}$  is unaffected by the presence of the metal shell inside the silica coating. The observed emission of the ICG- NS system is therefore

$$I_{NS} = (\langle |\mathbf{E}|^2 \rangle I_{exc}) \cdot \epsilon \cdot Q_{NS}. \quad (6-6)$$

We then evaluate the enhancement, following the same procedure as for the experiment, by taking the ratio of the emission from the ICG-NS ( $I_{NS}$ ) to the reference ICG on the silica nanosphere ( $I_o$ ):

$$\frac{I_{NS}}{I_o} = \langle |\mathbf{E}|^2 \rangle \frac{Q_{NS}}{Q_o} = \langle |\mathbf{E}|^2 \rangle \frac{\chi_r (\Gamma + k_{nr})}{\chi_r \Gamma + k_{nr}}, \quad (6-7)$$

where both the dye concentration and excitation intensity are taken to be the same in both cases. From this expression, one can see that the observed enhancement can be separated into the effect of the field enhancement ( $\langle |\mathbf{E}|^2 \rangle$ ) and the quantum yield enhancement ( $Q_{NS}/Q_o$ ). This expression indicates that fluorescence enhancement depends on the properties of the nanoparticle, and also the dye molecule, via  $\Gamma$  and  $k_{nr}$ . A third effect should come into play when the molecule is very close to the metal surface, where the fluorescence is quenched by an increase in the nonradiative decay rate. In the experimental regime studied here, no evidence of quenching is observed and is therefore not included in this analysis. We performed a control experiment with ICG molecules

bound to nanoshells without any silica layer, and observed fluorophore quenching, shown in Figure 6-5. However, direct comparison of the fluorescence enhancement factor of ICG molecules bound to NS@SiO<sub>2</sub> nanoparticles relative to ICG adsorbed on NS surface would not be quantitative since the chemical environment of the fluorophore is different in each solution.

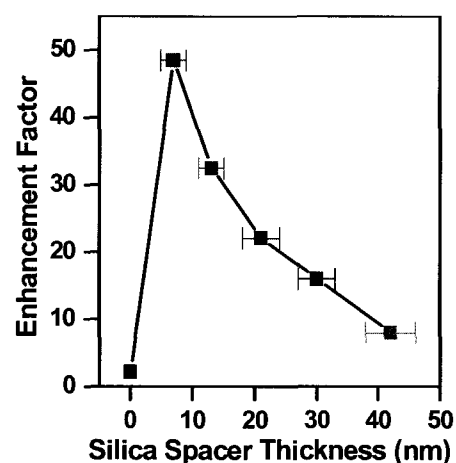


**Figure 6-5** Fluorescence enhancement factor of ICG molecules adsorbed on NS without any silica layer (■) is represented showing strong quenching of ICG molecules. ICG molecules bound to NS@SiO<sub>2</sub> nanoparticles relative to silica nanospheres is also shown as a function of silica layer thickness surrounding the NS. The data points representing ICG-NS@SiO<sub>2</sub> nanoparticles are color coordinated with ref. to Figure 6-4B and C.

The model we have used yields excellent agreement with the observed fluorescence enhancement as a function of distance (Figure 6-6A). To obtain this fit, we first calculated the surface-averaged near field intensity enhancement  $\langle |E|^2 \rangle$  as a function of distance from the nanoshell surface using Mie theory (Figure 6-6B). This term appears quite similar to the observed distance-dependent fluorescence enhancement. However, it was shown previously that near field enhancement alone does not explain the fluorescence enhancement as a function of plasmon energy for ICG at a fixed distance from the nanoparticle surface.<sup>89</sup> Therefore we need to investigate to what extent the

properties of the molecule affect the fluorescence enhancement. We also calculate the radiative rate enhancement factor  $\chi_r$  (Figure 6-6C).

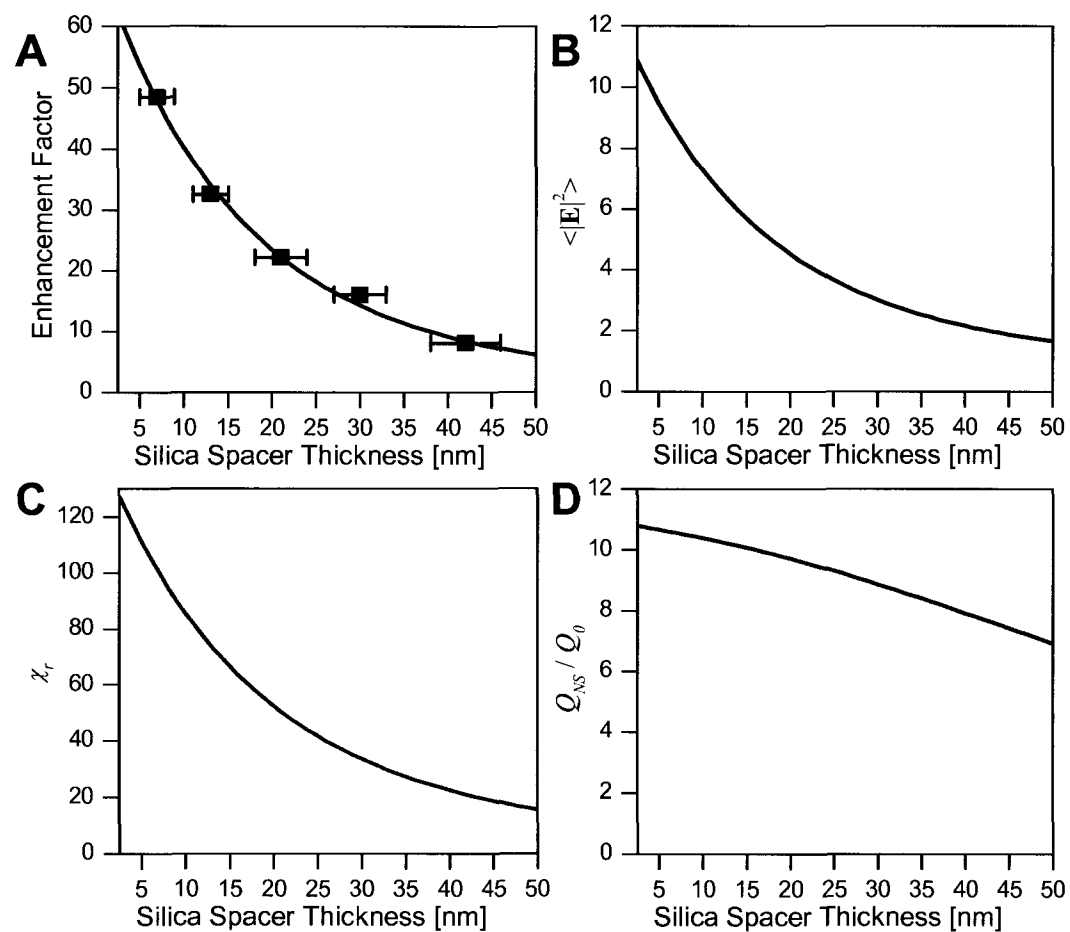


**Figure 6-6** (A) (■) Experimental, and (—) calculated values of fluorescence enhancement factor of ICG conjugated to NS@SiO<sub>2</sub> nanoparticles relative to ICG bound to silica nanospheres. (B)–(D) Calculated values of distance dependent fluorescence of ICG as a function of silica spacer thickness surrounding the NS. (B) Calculated surface average field enhancements, (C) Calculated radiative rate enhancements, (D) Calculated Q.E. enhancement of ICG conjugated to NS@SiO<sub>2</sub> nanoparticles relative to that of silica nanospheres.

To calculate the quantum yield enhancement  $Q_{NS}/Q_0$ ,  $\Gamma$  and  $k_{nr}$  for ICG in a silica environment are required. To determine these parameters, the total fluorescence enhancement (Eqn. 6–7) was fit to the experimental data with  $\Gamma$ ,  $k_{nr}$ , and a scale factor (interpreted as molecular orientation) as free parameters, using a generalized reduced

gradient minimization algorithm. The initial values of  $\Gamma$  and  $k_{nr}$ , were chosen based on the rates previously reported.<sup>157</sup> From this approach, values of  $\Gamma = 0.19 \text{ ns}^{-1}$ ,  $k_{nr} = 2.1 \text{ ns}^{-1}$ , and a scale factor of 0.53, yielding values of  $\tau_o = 0.44 \text{ ns}$  and  $Q_o = 8.6 \%$  for the ICG-on-silica-nanoparticle control sample, were obtained. The increase in quantum yield for ICG from nominally 1.3% for the molecule in solution to 8.6% for ICG adsorbed on silica nanoparticles is quite reasonable and consistent with several aspects of the molecule's new environment: stabilization of the polymethine chain due to adsorption on the silica surface, and the reduction in polarity and free oxygen exposure relative to an aqueous phase environment.<sup>157</sup> The resulting fit (i.e. the product of Figures 6-6B, 6-6, and a scale factor on the order of 0.5) is shown in Figure 6-6A. The scale factor is justifiable due to the random orientation of ICG on the nanoparticle surface. The agreement between our analysis and the experimental data shown in Figure 6-6A demonstrates that this modeling approach does an excellent job describing the system, and also confirms that the sample uniformity is quite good. Due to the tractability of this system, this approach is highly promising for further experimental studies and analysis of fluorescence modification on nanoshell-based structures.

### 6.5 Calculated Quantum Yield and Lifetime

Examining the contribution from the near field enhancement (Figure 6-6B) and quantum yield enhancement (Figure 6-6D), it can be seen that the radiative rate enhancement is actually more important than the near field enhancement at all distances studied here, and decreases quite slowly with distance. This is quite an important point to consider, since a fluorophore with intrinsically high quantum yield can only be enhanced due to  $\langle |\mathbf{E}|^2 \rangle$ , and would therefore experience much weaker enhancement. The effective quantum yield

and lifetime of the ICG-NS system can be calculated using these obtained parameters and Equations 6-4 and 6-57-5 from chapter 1, and is shown in Figure 6-7. From Figure 6-7A it can be seen that the quantum yield is strongly enhanced, approaching unity, relative to the unenhanced 8.6% quantum yield without the presence of the nanoshell. In this analysis, the quantum yield enhancement (Figure 6-6D) is relatively flat for thin spacer layers. The lifetime of the dye decreases significantly as the silica layer is decreased (Figure 6-7B), resulting in an increased quantum yield. Further studies to test this model using direct lifetime measurements are currently underway.

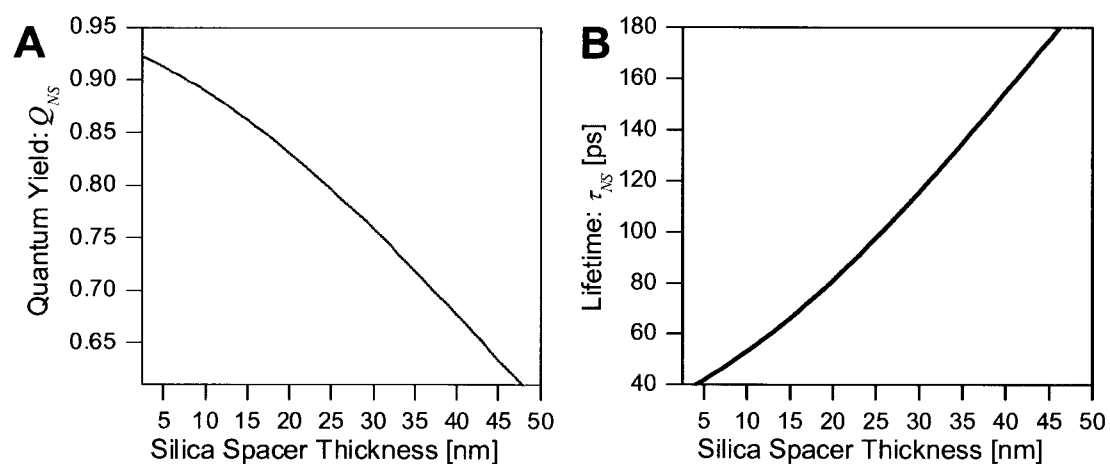


**Figure 6-7** Calculated values of distance dependent fluorescence of ICG as a function of silica spacer thickness surrounding the Au-NS (a) quantum yield and (b) lifetime.

## 6.6 Conclusions

In conclusion, we have shown that fabrication of silica epilayers surrounding NS nanoparticles of controlled thicknesses allows us to examine the distance-dependent fluorescence enhancement of the low quantum yield molecular fluorophore ICG in a quantifiable manner. A maximum fluorescence enhancement of 50 $\times$  is achieved at a distance of  $\sim 7$  nm from the NS surface, and even for the thickest silica layer fabricated on the NS ( $\sim 42$  nm) a 7 fold enhancement is still observed. The quantum yield of ICG

molecules decrease with increasing distance from the NS surface due to a decrease in the NS near field at the excitation wavelength and a decrease in coupling of the fluorophore to the NS plasmon at the emission wavelength. The strongly enhanced fluorescent emission of ICG in this nanoparticle configuration is potentially very valuable in biomedical imaging and clinical diagnostic applications. This strategy for enhancing the emission of low-quantum-yield fluorescent emitters can be straightforwardly generalized to other types of fluorescent emitters and media.

## **Chapter 7. Fluorescence Enhancement by Au nanostructures: Nanoshells and Nanorods**

### **7.1 Introduction**

In the previous chapter, we examined the distance dependence of the fluorescence enhancement by one nanoparticle geometry. The well-characterized nature of this system allowed us to perform a detailed theoretical analysis. This analysis indicated that, for low quantum yield near-infrared fluorophores, the enhancement of the radiative decay rate played a key role. In this chapter, we further explore the fundamental photophysics contributing responsible for plasmon-enhanced fluorescence by extending our study to Au nanorods, which have a large field enhancement but low scattering cross section, and directly measure the reduction in fluorescence lifetime due to the plasmonic nanoparticles. All nanoparticle synthesis, characterization, fluorescence, lifetime and experimental angular scattering measurements were performed by Rizia Bardhan. Nathaniel K. Grady developed the angular scattering apparatus, and contributed to the data interpretation and discussion. Joseph R. Cole performed the calculations of the optical properties of nanorods. Reproduced with permission from Rizia Bardhan, Nathaniel K. Grady, Joseph R. Cole, Amit Joshi, and Naomi J. Halas, "Fluorescence Enhancement by Au Nanostructures: Nanoshells and Nanorods," ACS Nano 3(3), 744-752 (2009). Copyright 2009 American Chemical Society.

Fluorescence imaging has seen widespread use in clinical diagnosis and monitoring processes in biological systems.<sup>158</sup> The development of contrast agents, such as fluorescent probes with engineered biomarker functionalities, has become integral to the advancement of new bioimaging technologies.<sup>159</sup> Fluorescent molecules emitting at

wavelengths in the physiologically relevant “water window” (700 nm – 900 nm), are of particular interest due to the large penetration depth of near infrared (NIR) light in most biological media, and offer the potential for imaging at significant depths in living tissues.<sup>160</sup> However, achieving bright fluorescent emission with photostable and biocompatible NIR fluorophores has proven to be extremely difficult. It has long been known that in the proximity of a metallic surface, fluorescence emission of molecules can be enhanced; this is also the case for metallic nanostructures and nanoparticles adjacent to a fluorophore.<sup>4, 125, 126, 161</sup> The presence of a nearby metallic nanoparticle can not only enhance the quantum yield but also stabilize adjacent fluorophores against photobleaching, further enhancing their practical use in bioimaging applications.<sup>127</sup> In new and emerging light-assisted therapeutic applications such as photothermal cancer therapy, the addition of bright NIR fluorescence to a therapeutic nanostructure complex could provide additional diagnostic imaging capabilities for this treatment strategy that could facilitate clinical use. Understanding precisely how metallic nanostructures enhance molecular fluorescence is of general fundamental interest, and may ultimately provide practical routes to enhancing light emission from a variety of materials systems and devices far beyond the specific application of bioimaging.

Metal nanostructures exhibit remarkable optical properties due to excitation of their surface plasmons by incident light, which results in a significant enhancement of the electromagnetic field at the nanoparticle surface. This enhanced near field can be used to design highly sensitive chemical and biosensors with specific plasmon resonances tailored by the nanoparticle geometry.<sup>162, 163</sup> Metallic nanoparticles have been shown to enhance the fluorescence emission and decrease the molecular excited-state lifetimes of

vicinal fluorophores. The fluorescence enhancement is attributable to a combination of processes including enhanced absorption by the molecule, modification of the radiative decay rate of the molecule, and enhanced coupling efficiency of the fluorescent emission to the far field.<sup>125, 127</sup>

The plasmon resonant properties of metallic nanoparticles can be controlled by optimizing the nanoparticle topology, dimensions, and composition.<sup>164-167</sup> When plasmonic nanoparticles are much smaller than a wavelength of light they are absorbers, much like molecules. Nanoparticles larger than a few tens of nanometers both absorb and scatter light. While both the absorption and scattering cross sections of a plasmon resonant nanoparticle increase with increasing particle size, scattering begins to dominate in this larger-size regime.<sup>89</sup> Au nanorods (NRs) and Au nanoshells (NSs) are both particularly useful for biological applications since their near field and far field optical properties can be tuned controllably throughout the NIR water window by varying their geometry. For NRs, the aspect ratio defines two distinct plasmon resonance frequencies associated with the longitudinal and transverse dimensions of the nanostructure.<sup>168</sup> For NSs, symmetric spherical nanoparticles consisting of a dielectric core and a metal shell, the plasmon resonances are determined by the relative size of the core and the metal shell layer.<sup>39</sup> NSs can be fabricated both in a small size regime ( $d \sim 50$  nm) using Au<sub>2</sub>S/Au and sizes up to a micron in silica/Au core/shell structures, accessing NIR resonances over a large size range.<sup>89</sup> NRs tuned to the same NIR plasmon resonance frequency as silica/Au NSs are significantly smaller in size than the corresponding nanoshell, resulting in a much smaller contribution of scattering to the overall extinction cross section. Studying

fluorescence enhancement by these two types of structures allows us to examine how the properties of both nanostructures contribute to this effect.

We have recently shown that the fluorescence of NIR fluorophores can be significantly enhanced when the molecules are in close proximity to NSs.<sup>20, 89</sup> Fluorescence enhancements as large as 50× were obtained when the plasmon resonance of the nanoshell was tuned to the emission wavelength of the fluorophore, for a nanoshell designed with a significant scattering cross section at that wavelength. In the study we report here, we compare the fluorescence enhancement of IR800 positioned a small, controlled distance from NSs and NRs. We quantified the fluorescence enhancement of IR800 experimentally by measuring the angle resolved scattering intensities, frequency domain fluorescence decay, and quantum yield of IR800 before and after binding to the nanoparticles. We also calculated the scattering cross sections of NSs and NRs to determine the scattering intensities of the nanoparticles and relative contribution of nanoparticle scattering towards molecular fluorescence enhancement.

When a fluorophore is adsorbed directly onto a metal surface, its fluorescence is quenched. However, at a distance of a few nanometers from the nanoparticle surface, the fluorescence can be strongly enhanced.<sup>103</sup> IR800 molecules were placed in close proximity of NS and NR surfaces by coating the nanoparticles with a 5-11 nm layer of human serum albumin (HSA) in order to prevent quenching of IR800. Serum albumin, a large multi-domain protein relevant to many physiological functions,<sup>169</sup> has been conjugated to Au nanoparticles extensively for cell-targeting applications.<sup>170, 171</sup> It binds to Au by electrostatic attraction between the amine groups of the protein and the negative

charge on the gold surface, or, alternatively, by covalent attachment between the Au surface and amino acid functional groups present in the protein.<sup>172</sup> In this study HSA acts as both a spacer layer as well as a linker of the fluorophore to the nanoparticle. It contains an abundance of  $\alpha$ -amines at N-terminals and  $\epsilon$ -amines on lysine side chains, which covalently bind to IR800 via the N-hydroxysuccinimide (NHS) ester group to form a stable protein-dye complex.<sup>173</sup> The NHS ester group facilitates protein conjugation, and the presence of the negatively charged sulfonate groups makes IR800 soluble in aqueous media. While these properties make IR800 a suitable dye for bioimaging,<sup>129</sup> it is limited by low quantum efficiency compared to commonly used visible dyes such as Boron Dipyrromethene (BODIPY) and Fluorescein isothiocyanate (FITC). Therefore, by binding IR800 to metal nanoparticles with a suitably determined spacer layer, the quantum yield can be significantly enhanced.

## 7.2 Fabrication of Nanoparticle-Fluorophore Conjugates

### 7.2.1 *Nanoparticle Fabrication*

All chemicals were purchased from Sigma Aldrich and IR800 NHS ester was purchased from Licor Biosciences. Au nanoshells (NSs) [ $r_1, r_2$ ] = [63, 78] nm were fabricated as previously described.<sup>26</sup> The fabricated NSs were centrifuged several times and finally redispersed in phosphate buffer ( $\text{Na}_3\text{PO}_4$ , pH ~ 8.0).

Au nanorods (NRs) [ $w, l$ ] = [11, 46] nm were fabricated by the method reported by Murphy and co workers.<sup>174</sup> Briefly, the seed solution was prepared by gently mixing 7.5 mL of 0.1 M Cetyl trimethylammonium bromide (CTAB) with 0.25 mL of 0.01 M  $\text{HAuCl}_4$ . 0.6 mL of ice-cold 0.01 M  $\text{NaBH}_4$  was injected into the solution and mixed

rapidly. The solution turns from a golden yellow color to pale brown color. It is essential that the temperature of  $\text{NaBH}_4$  is maintained at  $\sim 0^\circ\text{C}$  prior to mixing with CTAB and  $\text{HAuCl}_4$  for proper growth of nanorods. The seed solution was then stored at  $27^\circ\text{C}$  until further use. The growth solution was prepared by gently mixing 47.5 mL of 0.1 M CTAB, 2 mL of 0.01 M  $\text{HAuCl}_4$ , 0.3 mL of 0.01 M  $\text{AgNO}_3$  and 0.32 mL of 0.1 M Ascorbic Acid in the order mentioned. Addition of ascorbic acid turns the solution from golden yellow to colorless. 0.25 mL of the seed solution was added to the growth solution and mixed gently and then the solution was stored at  $27^\circ\text{C}$  for 3 hours without agitation. Within 20 minutes the solution changes from colorless to pink and eventually changes to dark pinkish brown after 3 hours. The NRs were washed twice at 8000 rpm to remove excess CTAB and finally redispersed in 10 mL  $\text{Na}_3\text{PO}_4$  buffer.

### 7.2.2 *Protein and Fluorophore Conjugation*

HSA was conjugated to IR800 by mixing equal volumes of 5  $\mu\text{M}$  HSA aqueous solutions in  $\text{Na}_3\text{PO}_4$  buffer and 30  $\mu\text{M}$  IR800 aqueous solution at room temperature for 5 hours, in the dark. The protein-fluorophore complex was then dialyzed in  $\text{Na}_3\text{PO}_4$  buffer for 24 hours at room temperature protected from light, in a 3500 MW dialysis bag (MW of HSA is 67 kDA and MW of IR800 is 1166 g/mol) to remove excess dye. Absorbance peaks of the protein-dye complex ( $\lambda_{\text{max}} = 782\text{ nm}$ ) and protein ( $\lambda_{\text{max}} = 280\text{ nm}$ ) were monitored to account for free-dye removal. After sufficient removal of unbound dye, the ratio of fluorophore to protein concentration ( $N_{\text{IR800}}:\text{NHSA}$ ) of the complex is determined by utilizing the absorbance of fluorophore at 782 nm ( $A_{\text{IR800}}$ ), molar extinction coefficient of IR800 ( $\epsilon_{\text{IR800}}$ ), absorbance of HSA at 280 nm ( $A_{\text{HSA}}$ ), molar extinction coefficient of HSA ( $\epsilon_{\text{HSA}}$ ) given by:

$$N_{\text{IR800}} / N_{\text{HSA}} = [A_{\text{IR800}}/\epsilon_{\text{IR800}}] / [A_{\text{HSA}}/\epsilon_{\text{HSA}}]$$

where  $\epsilon_{\text{IR800}} = 240,000 \text{ M}^{-1}\text{cm}^{-1}$  and  $\epsilon_{\text{HSA}} = 42,864 \text{ M}^{-1}\text{cm}^{-1}$ . The final protein concentration was calculated using the molecular weight ( $M.W._{\text{HSA}}$ ) and dilution factor (d. f.) of original solution given by:

$$N_{\text{HSA}} = [A_{\text{HSA}}/\epsilon_{\text{HSA}}] \times M.W._{\text{HSA}} \times \text{d. f.}$$

The final protein concentration was  $\sim 4 \mu\text{M}$  and fluorophore concentration was  $\sim 10 \mu\text{M}$ .

### 7.2.3 *Protein-Fluorophore Complex Binding to Nanoparticles*

The protein-fluorophore complex obtained was conjugated to the nanoparticles by adding 1 mL of HSA-IR800 solution in  $\text{Na}_3\text{PO}_4$  buffer to 10 ml nanoshells, and 10 ml nanorods dispersed in  $\text{Na}_3\text{PO}_4$  buffer respectively under constant stirring. After 7 hours conjugation at room temperature, in the dark, the nanoparticles were centrifuged in small aliquots of 500  $\mu\text{L}$  to remove excess dye and resuspended in  $\text{Na}_3\text{PO}_4$  buffer and we closely monitored the absorbance of the supernatant to account for unbound fluorophore concentration in the supernatant (9.55 – 9.65  $\mu\text{M}$ ). The concentration of the supernatant was then subtracted from the initial concentration of HSA-IR800 which was added to the nanoparticles to calculate the amount of HSA-IR800 on the nanoparticles. The final NSs concentration after resuspension in buffer was at  $\sim 10^8$  particles/mL and final NRs concentration was at  $\sim 10^9$  particles/mL. The surface area available for the HSA-IR800 complex to bind to the nanoparticles was normalized (see below) and hence the concentration of fluorophore was equivalent for both the NSs-HSA-IR800 and NRs-HSA-IR800,  $\sim 400 \pm 50 \text{ nM}$ .

7.2.4 Calculation of surface area available for HSA-IR800 to bind to nanoparticles

The amount of protein and fluorophore bound to the nanoparticles were quantified by assuming that IR800 binds to HSA similarly for both nanoshells and nanorods. The available surface area for fluorophore binding is kept equivalent for both nanoparticle solutions. The concentration ( $C_{NS}$ ) and extinction co-efficient ( $\sigma_{NS}$ ) for NSs were calculated utilizing Mie theory:

$$\sigma_{NS} = 9.6072 \times 10^{-10} \text{ cm}^2 \text{ for NSs } [r_1, r_2] = [63, 78] \text{ nm}$$

$$C_{NS} = \ln(10) \times \text{Absorbance} / \sigma \times \text{cuvette path length}$$

$$= 2.303 \times 0.052 / 9.6072 \times 10^{-10} \text{ cm}^2 \times 1 \text{ cm}$$

$$= 1.25 \times 10^8 \text{ particles/ mL.}$$

$$\text{The Surface Area of one NS (SA}_{NS}) = 4\pi [r_2^2 - r_1^2] = 2.855 \times 10^{-14} \text{ m}^2.$$

$$\text{The Surface Area of NSs solution} = (\text{SA}_{NS}) \times C_{NS} = 3.568 \times 10^{-6} \text{ m}^2/\text{mL.}$$

The extinction coefficient ( $\sigma_{NR}$ ) for NRs [ $w, l$ ] = [11, 46] nm resonant at ~ 800 nm have been reported previously as  $\sigma_{NR} \sim 4 \times 10^{-11} \text{ cm}^2$ .<sup>41</sup> The concentration of NRs ( $C_{NR}$ ) were calculated utilizing Gan's theory,

$$C_{NR} = 2 \times \text{Absorbance} / \sigma \times \text{cuvette path length}$$

$$= 2 \times 0.043 / 4 \times 10^{-11} \text{ cm}^2 \times 1 \text{ cm}$$

$$= 2.154 \times 10^9 \text{ particles / mL.}$$

The surface area of one NR ( $SA_{NR}$ ) =  $2\pi r^2 + 2\pi rl = 1.727 \times 10^{-15} \text{ m}^2$ .

The surface area of NRs solution =  $(SA_{NR}) \times C_{NR} = 3.719 \times 10^{-6} \text{ m}^2/\text{mL}$ .

However, experimentally the available nanoparticle surface area for fluorophore binding would vary slightly due to non-uniform size distribution of nanoparticles in solution.

#### 7.2.5 Calculation of no. of HSA-IR800 molecules bound to the nanoparticles

The diameter of a HSA molecule is approximately  $\sim 8 \pm 3 \text{ nm}$  and we assume the diameter of a IR800 molecule is roughly  $\sim 2 \text{ nm}$ , resulting in a hydrodynamic diameter of  $\sim 12 \text{ nm}$  for the protein-fluorophore complex. We have determined the number of fluorophore molecules per protein molecule by taking a ratio of their surface area:

The surface area of one HSA molecule ( $SA_{HSA}$ ) =  $4\pi r^2 = 4\pi (4 \times 10^{-9})^2 = 2.011 \times 10^{-16} \text{ m}^2$

The surface area of one IR800 molecule ( $SA_{IR800}$ ) =  $4\pi (1 \times 10^{-9})^2 = 1.256 \times 10^{-17} \text{ m}^2$

The no. of IR800 molecules per HSA molecule =  $SA_{HSA} / SA_{IR800}$

$$\approx 16 \text{ dye molecules}$$

We have also calculated the number of molecules of protein-fluorophore complex per nanoparticle, for both NSs as well as NRs:

The surface area of one HSA-IR800 molecule ( $SA_{HSA-IR800}$ ) =  $4\pi (6 \times 10^{-9})^2$

$$= 4.523 \times 10^{-16} \text{ m}^2$$

The no. of HSA-IR800 molecule per NS =  $SA_{NS} / SA_{HSA-IR800}$

$$= 2.855 \times 10^{-14} \text{ m}^2 / 4.523 \times 10^{-16} \text{ m}^2$$

$$\approx 63 \text{ HSA-IR800 molecules}$$

$$\text{The no. of HSA-IR800 molecule per NR} = SA_{\text{NS}} / SA_{\text{HSA-IR800}}$$

$$= 1.727 \times 10^{-15} \text{ m}^2 / 4.523 \times 10^{-16} \text{ m}^2$$

$$\approx 4 \text{ HSA-IR800 molecules}$$

However, as described above the surface area available for HSA-IR800 complex to bind to NSs and NRs have been normalized by adjusting the nanoparticle concentration. This provides almost equivalent amounts of protein-dye molecules to bind to each nanoparticle suspension.

### 7.3 Characterization of Nanoparticle-Fluorophore Conjugates

The nanoparticles were characterized by obtaining transmission electron microscope (TEM) images using a JEOL JEM-2010 TEM, and absorbance measurements using a Varian Cary 5000 UV-Vis-NIR spectrometer. Fluorescence emission spectra and frequency domain lifetime measurements were obtained using Jobin Yvon Fluorolog 3 and the samples were excited at 780 nm. The dynamic range of the Fluorolog 3 for lifetime measurements is 0 – 300 MHz. The absorption-emission profile of IR800 conjugated to HSA in sodium phosphate buffer ( $\text{Na}_3\text{PO}_4$ , pH ~ 8.0) is shown in Figure 7-1a. The absorbance maximum of the protein-fluorophore complex is observed at 782 nm, and the fluorescence emission maximum at 804 nm. The IR800 molecules were conjugated to HSA to form the HSA-IR800 complex, which was then bound to NSs (NSs-HSA-IR800) and NRs (NRs-HSA-IR800) as demonstrated in Figure 7-1b.

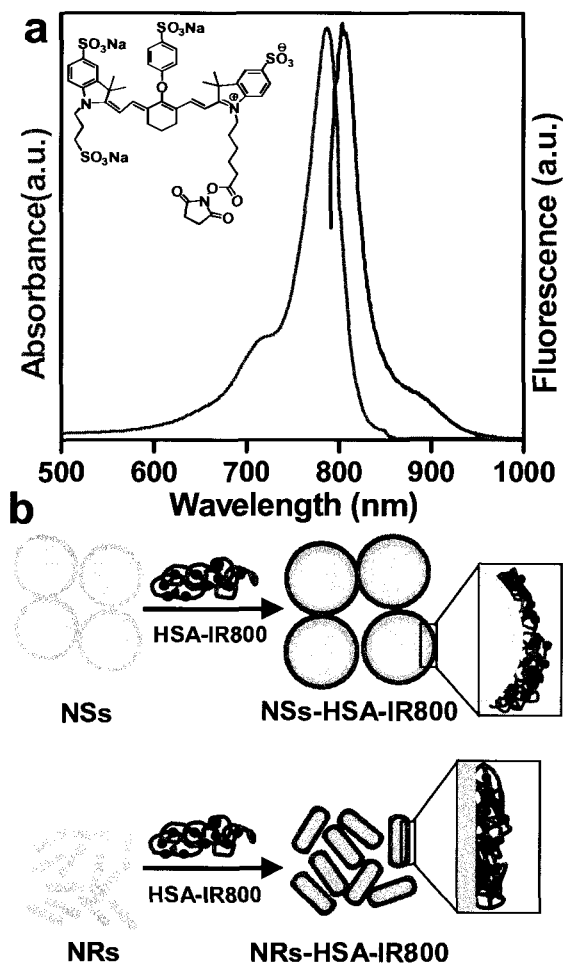


**Figure 7-1** (a) Absorption - emission profile ( $\lambda_{\text{max-Ab}} \sim 782$  nm and  $\lambda_{\text{max-Em}} \sim 804$  nm) of IR800 conjugated with HSA. Chemical structure of IR800 is provided as inset. (b) Schematic diagram illustrating the conjugation of HSA-IR800 protein-fluorophore complex to Nanoshells (NSs) and Nanorods (NRs) to form NSs-HSA-IR800 and NRs-HSA-IR800 respectively. The blue curved line represents HSA and red dots represent IR800 dye.

HSA-IR800 conjugation was performed at room temperature, and the protein-fluorophore complex was dialyzed for 24 hours to remove excess dye (see §7.2.2). It was determined that approximately 16 molecules of IR800 were bound to each HSA molecule (see §7.2.5). The bioconjugation of the HSA-IR800 complex to the nanoparticles was performed in  $\text{Na}_3\text{PO}_4$  buffer at room temperature and protected from light, and excess protein-fluorophore mixture was removed by centrifuging the nanoparticle conjugates in

small aliquots (see §7.2.3). We determined that  $\sim 63$  HSA-IR800 complexes were conjugated to each NS and  $\sim 4$  HSA-IR800 complexes were bound to each NR (see §7.2.5). However, the total number of HSA-IR800 complexes bound to NSs or NRs was kept constant by adjusting the nanoparticle concentration, such that the total surface area available for conjugation was equivalent for both NSs and NRs (see §7.2.4).

The geometry of the nanoparticles coated with HSA-IR800 was characterized with transmission electron microscopy (TEM). TEM micrographs of NSs with dimensions  $[r_1, r_2] = [63, 78]$  nm, where  $r_1$  is the radius of the silica core and  $r_2$  is the radius of the Au shell, are shown in Figure 7-2a. NRs,  $[w, l] = [11, 46]$  nm, where  $w$  is the width and  $l$  is the length, are shown in Figure 7-2c. The NSs and NRs coated with a uniform  $8 \pm 3$  nm layer of HSA are shown in Figures 7-2b and 7-2d, respectively.

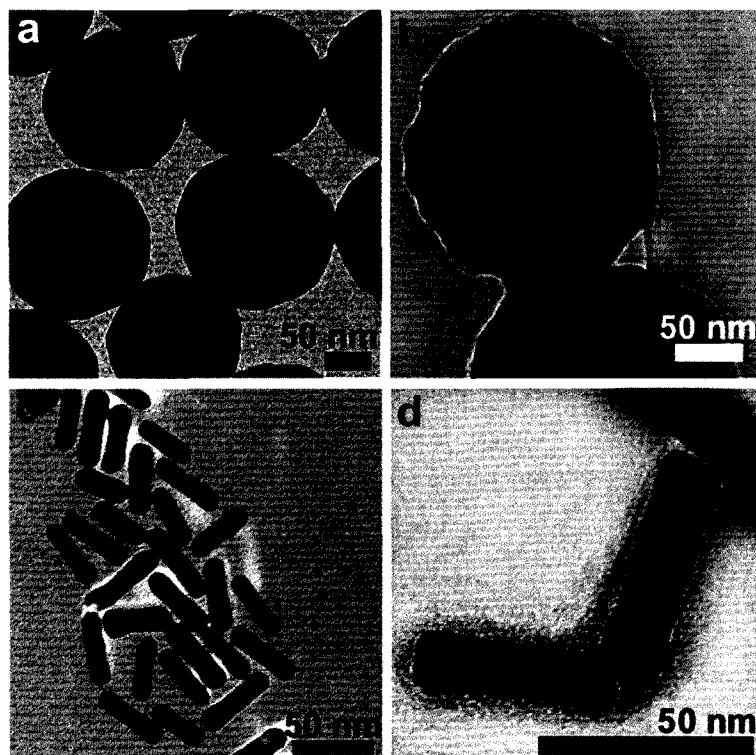


**Figure 7-2** TEM micrographs of (a) NSs  $[r_1, r_2] = [63, 78]$  nm, (b) NSs coated with  $8 \pm 3$  nm HSA-IR800, (c) NRs  $[w, l] = [11, 46]$  nm, and (d) NRs coated with  $8 \pm 3$  nm HSA-IR800.

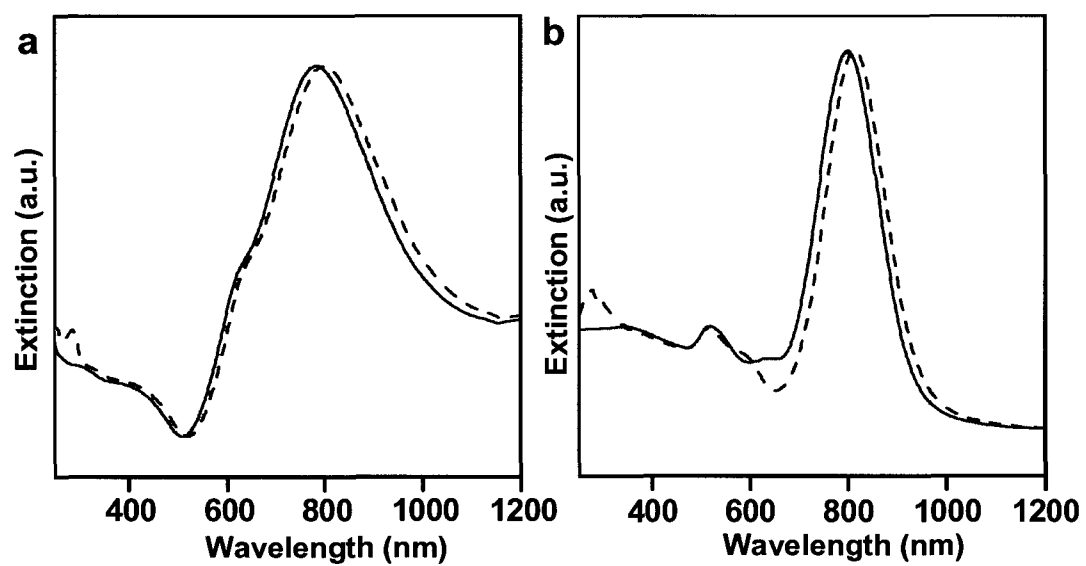


**Figure 7-3** Surface plasmon resonance shift when nanoparticles are conjugated with HSA-IR800 (a) NSs (solid red),  $\lambda_{\max} \sim 800$  nm and NSs coated with HSA-IR800 (dash),  $\lambda_{\max} \sim 805$  nm, and (b) NRs (solid blue),  $\lambda_{\max} \sim 796$  nm and NRs coated with HSA-IR800 (dash),  $\lambda_{\max} \sim 804$  nm. The peak at 280 nm is protein absorbance peak.

#### 7.4 Experimental Fluorescence Enhancement

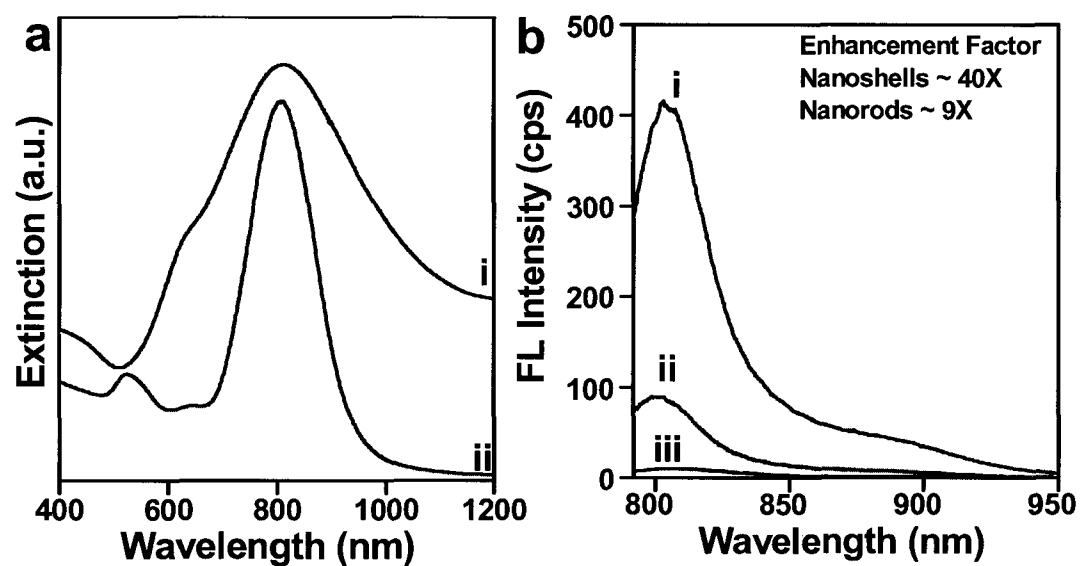


**Figure 7-4** (a) Extinction spectra of (i) NSs-HSA-IR800, plasmon maximum at  $\sim 805$  nm, and (ii) NRs-HSA-IR800, plasmon maximum at  $\sim 804$  nm are shown. Spectra are offset for clarity. (b) Fluorescence (FL) spectra,  $\lambda_{\text{max}} \sim 804$  nm of (i) NSs-HSA-IR800, (ii) NRs-HSA-IR800, and (iii) control sample HSA-IR800 are shown.

The plasmon resonance of NSs and NRs shifts to longer wavelengths by 5 – 8 nm when HSA-IR800 is adsorbed, due to the higher refractive index of HSA than  $\text{H}_2\text{O}$ <sup>156, 175</sup> shown in Figure 7-3. The plasmon resonances of the nanoparticles were tuned to the emission wavelength of the fluorophore-protein complex to maximize the fluorescence enhancement.<sup>89</sup> The extinction maximum of NSs-HSA-IR800 was observed at  $\sim 805$  nm, and that of NRs-HSA-IR800 was observed at  $\sim 804$  nm, as shown in Figure 7-4a. The corresponding emission spectra of HSA-IR800 conjugated to the nanoparticles are shown in Figure 7-4b. HSA-IR800 was used as the control sample rather than IR800 in aqueous solution to ensure that the fluorophore was in essentially the same chemical environment in all measurements. The emission spectra of nanoshells coated with HSA without IR800 and nanorods coated with HSA without IR800 are also provided in Figure 7-5. The nanoparticles exhibited no fluorescence in the near-infrared without the fluorophore. The

reference sample as well as the nanoparticle-conjugates was excited at 780 nm and the fluorescence spectra were collected in solution under identical excitation and detection conditions, allowing direct comparison of the various nanoparticle-fluorophore complexes. A maximum fluorescence enhancement of  $\sim 40$  was measured for NSs-HSA-IR800 relative to the control sample, and an enhancement of  $\sim 9$  was found for NRs-HSA-IR800.

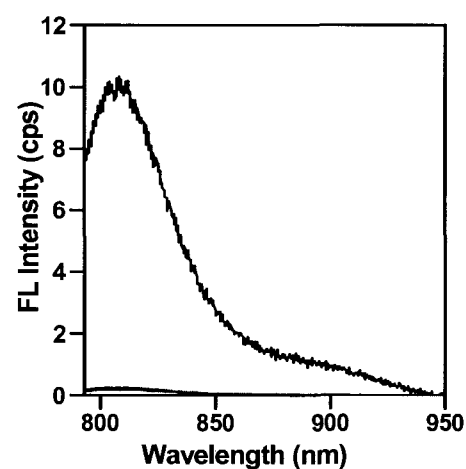


**Figure 7-5** Emission spectra of control, HSA-IR800 (black), nanoshells coated with HSA without IR800 (red), and nanorods coated with HSA without IR800 (blue) are shown. Fluorescence is not observed from the nanoparticles without the fluorophore.

### 7.5 Calculated and Experimental Scattering Efficiency of Nanostructures

Since the nanoparticles used in this experiment vary in size, their relative scattering cross sections also differ significantly, which directly affects their fluorescence enhancement efficiency. We determined the scattering intensities of the NSs and NRs by calculating their scattering cross sections using experimentally obtained nanoparticle sizes. The calculated scattering intensities for NSs  $[r_1, r_2] = [63, 78]$  nm in aqueous medium were obtained using Mie theory, and the maximum plasmon resonance peak was observed at 800 nm. The theoretical scattering intensity of NRs was calculated by using the finite

element method (FEM) (as implemented by COMSOL Multiphysics). The nanorods were modeled as cylindrical objects with hemispherical end-caps in H<sub>2</sub>O, estimating size obtained from TEM  $[w, l] = [11, 46]$  nm. The dielectric function used for Au was obtained from literature values.<sup>50</sup> The calculated longitudinal plasmon mode of NRs, showed a maximum at a wavelength of 824 nm in water. The experimentally observed longitudinal plasmon resonance of NRs (804 nm) differs from that calculated theoretically because the energy of the longitudinal mode depends strongly on the end cap geometry.<sup>176</sup> Nonetheless, the calculated scattering spectra shown in Figure 7-6 indicate that NSs scatter more efficiently than NRs for the sizes of nanoparticles studied.

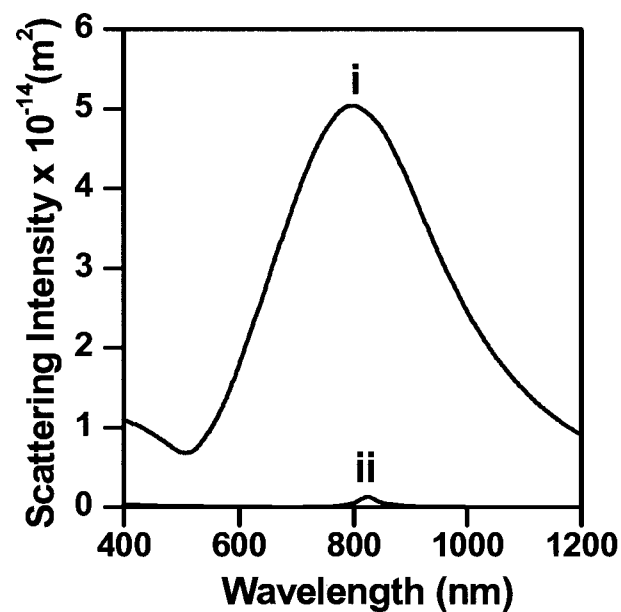


**Figure 7-6** Calculated scattering spectra of (i) NSs  $[r_1, r_2] = [63, 78]$  nm,  $\lambda_{\max} = 805$  nm and (ii) NRs  $[w, l] = [11, 46]$  nm,  $\lambda_{\max} = 824$  nm.

The relative scattering efficiency was also obtained experimentally by utilizing solutions with similar concentrations of NSs and NRs (Figure 7-7A). The nanoparticle solutions were positioned in a 6.25 mm path length cylindrical cuvette and placed on a goniometer which rotated the collection point around the sample while keeping the angle of the

sample fixed. A 785 nm diode laser was used as the excitation source, along with appropriate combination of filters and linear polarizers for light propagation and detection. The scattered light from the nanoparticles was detected by a CCD array connected to a spectrograph. The scattering intensities of the nanoparticles were then determined by obtaining the scattered light intensity as a function of polar angle. The measurements range from  $0^\circ$  to  $360^\circ$ , however measurements between  $130^\circ$  -  $180^\circ$  were not obtained due to constraints in the experimental set-up. The spectra are not completely symmetric for rotation over  $90^\circ$  attributable to a small misalignment in the apparatus. We observe that NSs scatter by a factor of  $\sim 34$  more than NRs. (Figure 7-7B) The larger scattering efficiency of NSs relative to NRs studied here correlates with the larger fluorescence enhancement observed for IR800 by NSs.

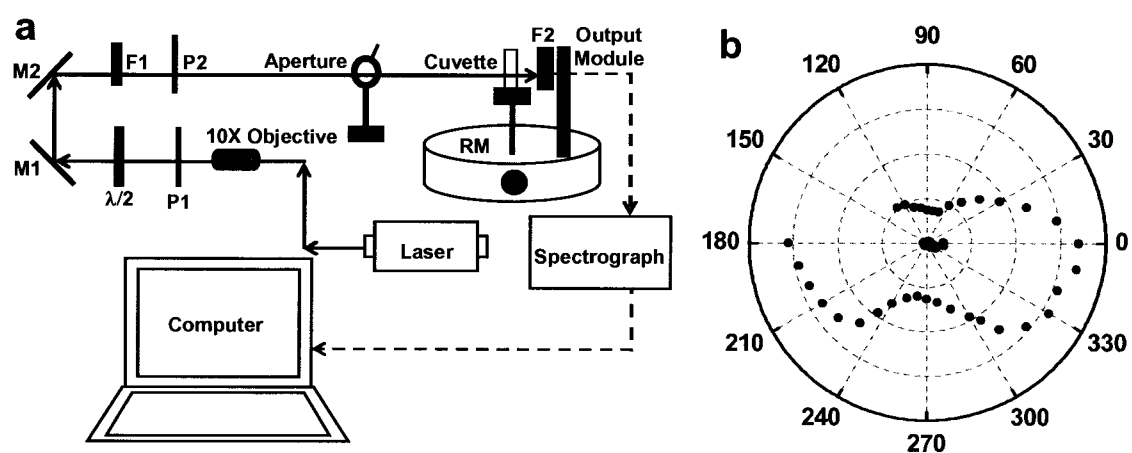


**Figure 7-7** (a) Schematic diagram representing angle-resolved fluorescence emission apparatus. M1: Mirror1, M2: Mirror 2, P1: Polarizer, P2: Polarizer,  $\lambda/2$ : Half-wavelength plate, F1: Laser selection filter, F2: Long pass filter, RM: Rotating mount with knob to control the angle of the sample relative to the excitation light (Red circle). Black solid line indicates laser light path. (b) Experimental angle-resolved scattering spectra of NSs (red circles) and NRs (blue circles). Spectra are normalized by concentration of nanoparticles. The radial axis ranges from 0 – 4.

## 7.6 Frequency Domain Lifetime Decay

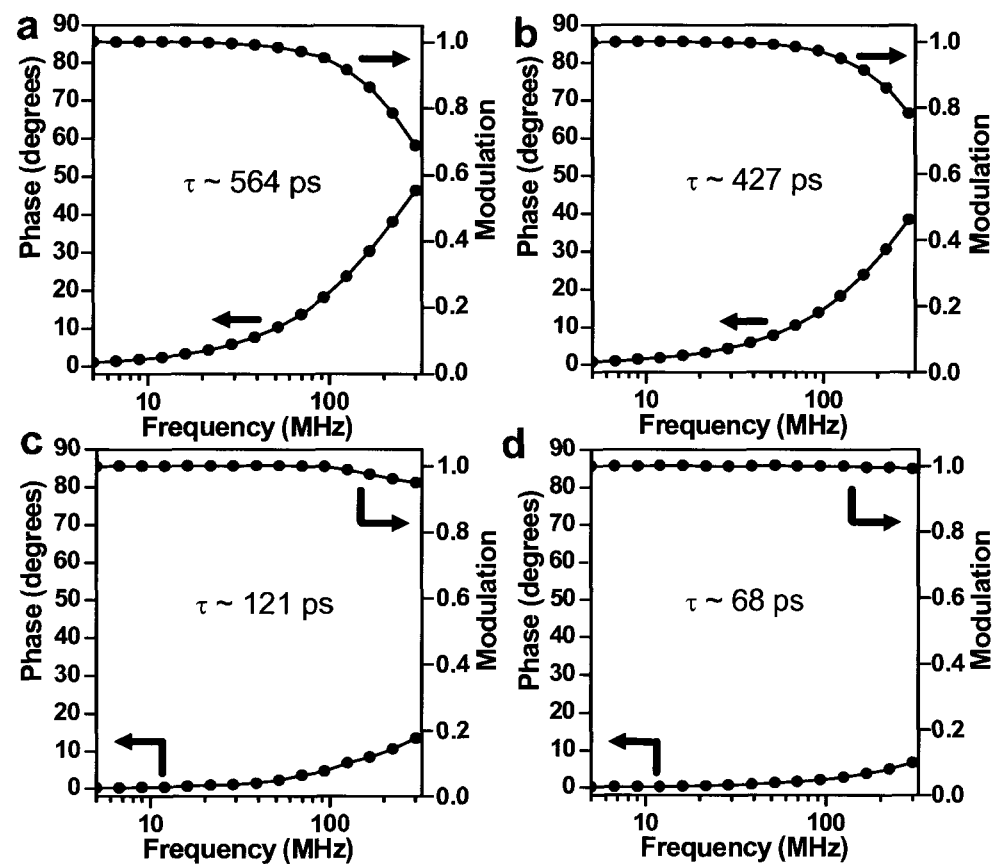


**Figure 7-8** Frequency domain fluorescence decay of (a) IR800 ( $\tau \sim 564$  ps), (b) HSA-IR800 ( $\tau \sim 427$  ps), (c) NRs-HSA-IR800 ( $\tau \sim 121$  ps), and (d) NSs-HSA-IR800 ( $\tau \sim 68$  ps). The curves referring to phase and modulation are shown with arrows.

In addition to the scattering characteristics of the nanoparticles, increasing the radiative decay rate of the fluorophore also contributes substantially to fluorescence enhancement.

In a homogeneous solution, fluorophores emit light into free space and are observed in the far field. The observed emission of the fluorophore in the absence of any quenching interactions is described in terms of quantum yield ( $Q_0$ ) and lifetime ( $\tau_0$ ). The quantum yield, given by

$$Q_0 = \frac{\Gamma}{\Gamma + k_{nr}} \quad (7-1)$$

is the fraction of the excited fluorophores which relaxes by radiative decay ( $\Gamma$ ) relative to the total relaxation rate ( $\Gamma + k_{nr}$ ). The observed lifetime is simply the inverse of the total decay rate of the excited state:

$$\tau_0 = \frac{1}{\Gamma + k_{nr}}. \quad (7-2)$$

When a fluorophore is in the presence of a metal nanoparticle, the enhanced near field of the nanoparticle increases the amount of light absorbed by the molecule. In addition, electromagnetic coupling occurs between the fluorophore and the nanoparticle plasmon, causing an increase in the radiative decay rate of the molecule at the emission wavelength by a factor  $\gamma_r$ . As a result, the effective radiative decay rate is equivalent to  $\gamma_r\Gamma$ . The modified quantum yield ( $Q_M$ ) and lifetime ( $\tau_M$ ) are then given by

$$Q_M = \frac{\gamma_r\Gamma}{\gamma_r\Gamma + k_{nr}} \quad (7-3)$$

and

$$\tau_M = \frac{1}{\gamma_r\Gamma + k_{nr}}. \quad (7-4)$$

We assume that the nonradiative decay rate,  $k_{nr}$ , is unaffected by the presence of the nanoparticles.

The change in radiative lifetime for IR800 conjugated to NSs and NRs via HSA was determined experimentally by monitoring the frequency domain fluorescence decay in aqueous solution. The lifetime spectra of IR800, HSA-IR800, NRs-HSA-IR800, and NSs-HSA-IR800 are shown in Figure 7-8. The intrinsic lifetime of the fluorophore was measured to be  $\sim 564$  ps, which corresponds well to the previously reported value.<sup>129</sup> The

lifetime decreased to 427 ps when IR800 molecules were bound to HSA (Figure 7-8b). This is due to a small enhancement in quantum yield of the fluorophore when conjugated to the protein, attributable to an increased steric stabilization of IR800 bound to HSA. This reduces the mobility of the fluorophore in aqueous solution, resulting in higher stability and a decreased lifetime.<sup>177</sup> The lifetime of IR800 bound to the nanoparticles via HSA was reduced significantly to 121 ps for NRs-HSA-IR800 and 68 ps for NSs-HSA-IR800. These measured lifetimes confirm the theoretical prediction of enhanced quantum yield and diminished lifetime of fluorophores near metallic surfaces.<sup>20</sup>

In the frequency domain technique, lifetime measurements are obtained by exciting the fluorescent sample with intensity-modulated light at a high frequency comparable to  $\tau^{-1}$  of the sample. Subsequent to excitation, the fluorescence emission of the sample follows the same modulation frequency as the excitation, but it is delayed in time relative to the excitation. The time delay is measured as a phase shift ( $\Phi$ ) from which the lifetime ( $\tau_{\Phi}$ ) is determined:

$$\tau_{\Phi} = \frac{1}{\omega} \tan(\Phi) \quad (7-5)$$

where  $\omega$  is angular frequency. The fluorescence lifetime data can be evaluated in terms of a single exponential (SE) model or a multiexponential (ME) model. A SE model is appropriate for samples consisting of a single fluorophore in a homogeneous environment, while a ME model describes the fractional contribution of decay time for each component present in a sample mixture.<sup>178</sup> The ME model for analyzing the intensity decay is given by

$$I(t) = \sum_i \alpha_i e^{-\frac{t}{\tau_i}}, \quad (7-6)$$

where  $\tau_i$  are observed lifetimes with amplitude or molecular fraction  $\alpha_i$ , such that

$$\sum_i \alpha_i = 1.$$

The amplitude-weighted lifetime is then

$$\langle \tau \rangle = \sum_i \alpha_i \tau_i. \quad (7-7)$$

The results of fitting to a ME decay analysis are represented in Table 7-1. The decay rate for IR800 in aqueous media, in the absence of any other component in the solution, fits a SE decay model. However, the HSA-IR800 complex required a ME decay model, demonstrating that two different environments are available to the fluorophore with distinct lifetimes in each individual environment. About 90 % of the IR800 molecules were covalently attached to HSA with a fluorescence decay of 418 ps. The lifetime of the remaining fraction was similar to that observed for free IR800 in aqueous media, suggesting that a small fraction of unbound fluorophores remain in the HSA-IR800 solution. The ME analysis of the fluorescence decay of IR800 conjugated to nanoparticles indicates three distinct environments, which we interpret as IR800 molecules conjugated to the nanoparticle-HSA, IR800 molecules bound to HSA only, and the free fluorophore in solution. Most of the fluorophores in these samples exhibited a significantly reduced lifetime, indicating that nearly all of the dye molecules were attached to the nanoparticles via the HSA layer. This analysis reveals that both

nanoparticle samples had less than 2% of unbound HSA-IR800 complex and less than 1% of free fluorophore in the solution mixture. This is attributable to the high affinity of the protein for Au nanoparticle surface as well as the use of a fluorophore with a chemical linker which can covalently attach to the protein. Therefore, the nanoparticle-HSA-IR800 system provides a useful complex for determining individual lifetime components. The  $\chi^2_R$  values shown in the last column of Table 7-1 are the goodness of fit parameter, obtained by fitting calculated values to experimentally obtained parameters by a nonlinear least-squares deconvolution method. The  $\chi^2_R$  values represented here are within 5–10% of the random deviations in the data.<sup>178</sup>

Sample	$\alpha_i$	$\tau_i$	$\langle\tau\rangle$	$\chi^2_R$
IR800	1	0.564	0.564	1.57
	–	–		
	–	–		
HSA-IR800	0.076	0.547	0.427	1.54
	0.924	0.418		
	–	–		
NRs-HSA-IR800	0.008	0.550	0.121	1.42
	0.019	0.419		
	0.973	0.112		
NSs-HSA-IR800	0.005	0.568	0.068	1.39
	0.01	0.421		
	0.985	0.065		

**Table 7-1** Multiexponential analysis of intensity decay of IR800 with nanoparticles showing molecular fraction ( $\alpha$ ), observed lifetime ( $\tau_i$ , ns), amplitude weighted lifetime ( $\langle\tau\rangle$ , ns), and goodness of fit parameter ( $\chi^2_R$ ).

### 7.7 Experimental Quantification of Quantum Yield

In order to determine the radiative rate enhancement from the experimentally measured changes in lifetime, the nonradiative decay rate must be known. By combining and

rearranging eqs. 7-1 and 7-2, the radiative and nonradiative decay rate can be experimentally obtained:

$$\Gamma = \frac{Q_0}{\tau_0} \quad (7-8)$$

$$k_{nr} = \frac{1}{\tau_0} - \Gamma \quad (7-9)$$

The quantum yield of IR800 ( $Q$ ) was determined experimentally using Indocyanine green (ICG) as a reference sample with a known quantum yield ( $Q_R$ ) of  $\sim 1\%$  in aqueous media.<sup>157</sup> The NIR excitation-emission profile of ICG (excitation: 780 nm, emission: 820 nm) is similar to that of IR800 and is therefore ideal as a reference sample for quantum yield determination. The quantum yield was computed by measuring the optical density of solutions with equivalent concentrations of IR800 ( $OD$ ) and ICG ( $OD_R$ ) and by calculating the integrated fluorescence intensity of IR800 ( $I$ ) and ICG ( $I_R$ ):

$$Q = Q_R \frac{I}{I_R} \frac{OD}{OD_R} \frac{\eta}{\eta_R}, \quad (7-10)$$

where  $\eta$  is the refractive index of sample medium and  $\eta_R$  is the refractive index of the reference medium, which are equivalent in this experiment ( $\eta = \eta_R = \eta_{H_2O} = 1.33$ ). By using Eqn. 7-10, the quantum yield of IR800 was determined to be 7% in H<sub>2</sub>O, and that of the HSA-IR800 complex was determined to be 11%. Using the quantum yield and lifetime measured independently, Eqs. 7-8 and 7-9 allow determination of the radiative and nonradiative decay rates of the fluorophore as shown in Table 7-2. The quantum yield values obtained for IR800 in aqueous media as well as HSA-IR800 are comparable to those reported in the literature.<sup>179</sup>

Sample	Q.Y.	$\Gamma$	$k_{nr}$
IR800	0.07	$1.241 \times 10^8$	$1.648 \times 10^9$
HSA-IR800	0.11	$2.576 \times 10^8$	$2.084 \times 10^9$
NRs-HSA-IR800	0.74	$6.180 \times 10^9$	$2.084 \times 10^9$
NSs-HSA-IR800	0.86	$1.262 \times 10^{10}$	$2.084 \times 10^9$

**Table 7-2** Quantum yield (Q.Y.), radiative decay rate ( $\Gamma$ ) and nonradiative decay rate ( $k_{nr}$ ) of IR800, HSA-IR800 and HSA-IR800 with nanoparticles.

The radiative rate enhancement of IR800 induced by NSs and NRs and the improved quantum yields can now be calculated by rearranging Eqs. 7-3 and 7-4:

$$\gamma_r \Gamma = \frac{1}{\tau_M} - k_{nr} \quad (7-11)$$

$$Q_M = \gamma_r \Gamma \tau_M, \quad (7-12)$$

where  $\tau_M$  is obtained from Table 7-1, and  $k_{nr}$  is the non-radiative decay rate for HSA-IR800. We assume that  $k_{nr}$  is unaltered from HSA-IR800 for both NS-HSA-IR800 and NR-HSA-IR800 complexes because no fluorescence quenching was observable and the chemical environment of the fluorophore was equivalent in all cases. The nonradiative decay rate does increase when the chemical environment of the fluorophore is changed<sup>180</sup> from solution phase to being bound to HSA. Table 7-2 shows that the  $k_{nr}$  increases when IR800 is bound to HSA compared to the free fluorophore in solution. On a metallic surface, the nonradiative decay rate also increases for short fluorophore-metal distances,  $< 4$  nm,<sup>102, 120, 143</sup> since the nonradiative energy transfer rate depends on the inverse cube of the molecule-surface separation.<sup>35</sup> However, in our nanostructure complexes, HSA provides a spacer layer of  $\sim 8$  nm between the fluorophore and the metal nanoparticle

surface. For this significantly larger metal-molecule distance, a significant increase in  $k_{nr}$  due to the metal nanoparticle surface is not anticipated.<sup>20, 89</sup> Therefore we assume that  $k_{nr}$  is essentially the same for HSA-IR800 in solution and for HSA-IR800 adsorbed sequentially onto a nanoshell or nanorod surface. The radiative decay rates of NRs-HSA-IR800 and NSs-HSA-IR800 and the quantum efficiencies are also shown in Table 7-2. The high quantum yield of 86% for NSs-HSA-IR800 demonstrates that plasmonic enhancement can be used to create NIR-fluorescent species with similar intensities as visible dyes. Although the NRs achieve a lower quantum yield of 74% due to the lower scattering efficiency of the particles, this is still a very high value for a NIR fluorophore, and these structures would certainly also be useful as markers in fluorescence-based bioimaging where the smaller physical size of the NR-based nanoparticle complex would be desired.

The precise relative contribution of each process responsible for IR800 fluorescence enhancement, including absorption enhancement, scattering enhancement, and radiative decay rate enhancement, is difficult to determine since these processes are interdependent. Nevertheless, for the experimental parameters and nanoparticle geometries discussed here, the scattering efficiency of a nanoparticle appears to provide the most important mechanism for improving the quantum yield of a fluorophore. NRs predominantly enhance the emission of the fluorophore by absorption enhancement, owing to the high-intensity near field resulting from the longitudinal plasmon resonance. However, due to the significant difference in scattering cross sections of NSs and NRs it is apparent that NSs increase the coupling efficiency of the fluorescence emission to the far field more efficiently than NRs. This explains the 40-fold fluorescence enhancement

observed for IR800 bound to NSs compared to the 9-fold enhancement for IR800 bound to NRs. The radiative decay rate enhancement of the fluorophore is dependent on both the scattering efficiency as well as the absorption efficiency of nanoparticles. This explains why NRs enhance the quantum yield of IR800 by 74% as well as decrease the fluorophore's lifetime considerably.

### **7.8 Conclusions**

In conclusion, we have examined the fluorescence enhancement of IR800 conjugated to NSs and NRs, and we have shown that both NS and NR lead to large increases in quantum yield relative to the isolated fluorophore. We have observed that nanoshells are more efficient in improving the emissive properties of a fluorophore due to their significant scattering cross section at the emission wavelength of the fluorophore. Additionally, the near-field response of NSs gives rise to a considerable enhancement in the absorption, and the radiative decay rate of IR800, resulting in 40 fold enhancement and 86% quantum yield. IR800 molecules bound to NRs demonstrate a 9-fold emission enhancement and a 74% quantum yield, attributable to the high local field enhancement at the longitudinal plasmon wavelength. Utilizing Au nanoparticles with appropriate geometry and dimensions for emission enhancement is a useful strategy for enhancing the detection sensitivity of low-quantum-yield fluorescent emitters. This approach is also potentially valuable in biomedical imaging, and moreover can be conveniently generalized to enhance other fluorescent media.

## **Chapter 8. Nanoparticle-Induced Enhancement and Suppression of Photocurrent in a Silicon Photodiode**

Both resonant plasmonic structures and non-resonant dielectric nanoparticles can significantly alter the flow of light through an interface. In the previous three chapters, we have examined in detail how the plasmonic response of Au nanoshells alters the properties of molecules directly adjacent to the surface. In this chapter, we examine the influence of nanoparticles on photocurrent generation in silicon photodiodes, where the pn junction is 500 nm below the surface upon which the particles are deposited. Adapted and reprinted with permission from Sri Priya Sundararajan, Nathaniel K. Grady, Nikolay Mirin, and Naomi J. Halas, "Nanoparticle-Induced Enhancement and Suppression of Photocurrent in a Silicon Photodiode," *Nano Letters* **8**(2), 624-630 (2008). Copyright 2008 American Chemical Society.

Photoinduced carrier generation and charge separation are the requisite processes of solar cells and photodetectors. In the photosynthetic reaction center of plants, nature has merged these two functions to achieve almost unit efficiency; however, in man-made devices their integration remains a critical challenge. The combined needs for light harvesting and voltage or current generation drive device design, bringing photoabsorbers directly into the active region of the device, as in the case of photoelectrochemical cells.<sup>181</sup> Another approach is to implement light-harvesting strategies in a separate processing step, by adding light-absorbing molecules or by positioning or patterning light-harvesting antenna structures onto the active face of a fabricated device.<sup>182</sup> This latter approach may offer methods for further increasing efficiencies of devices already in use or in production. If relatively inexpensive, mass-producible nanoparticles could serve

as effective light-harvesting nanoantennas, significant improvements in device efficiency and performance for photodetectors and solar cells may be obtainable at relatively low cost for widespread use. Recent experiments have shown that Au nanoparticles can be used as light-harvesting nanoantennas when deposited at remarkably low coverage on the active face of silicon solar cells.<sup>183-186</sup> The nanoparticles showed a measurable, wavelength dependent increase in device efficiencies in both shallow and buried pn junction devices. The junction depth dependence suggests two regimes of nanoparticle-induced light harvesting.

For deep junction devices, the forward scattered field (nominally within several particle diameters) affects photocurrent generation,<sup>187</sup> while for very shallow junction devices, the nanoparticle near field can enhance photocurrent generation in the active region close to the device surface.<sup>188, 189</sup> It is highly likely that the properties of the specific individual nanoparticles, such as absorption and scattering cross section and plasmon resonances, controlled by their size and shape, play a critical role in light harvesting in these types of device structures. However, the nanoparticle-dependent aspects of this highly promising light-harvesting strategy have not yet been investigated.

Here, we report a study of the changes in photocurrent in a buried silicon photodiode induced by nanoparticles of differing properties: Au nanoparticles, Au nanoshells and nanoshell aggregates varying in size and plasmon resonance frequency, and silica nanospheres. Photocurrent imaging, initially developed to obtain charge mapping in individual nanoscale devices,<sup>190</sup> is used here to measure the effect of each individual nanoparticle on the electrical response of the device. Plasmonic nanoparticles can either

enhance or suppress photocurrent in the device depending on wavelength, nanoparticle resonance, and nanostructure size and geometry. This surprising response is directly related to the complex energy flow of scattered light by plasmonic nanoparticles, an effect previously predicted for radiatively damped metallic nanoparticles in vacuum, but not yet experimentally observed. In contrast, dielectric scatterers provide a uniform photocurrent enhancement across a broad spectral range.

### 8.1 Structure

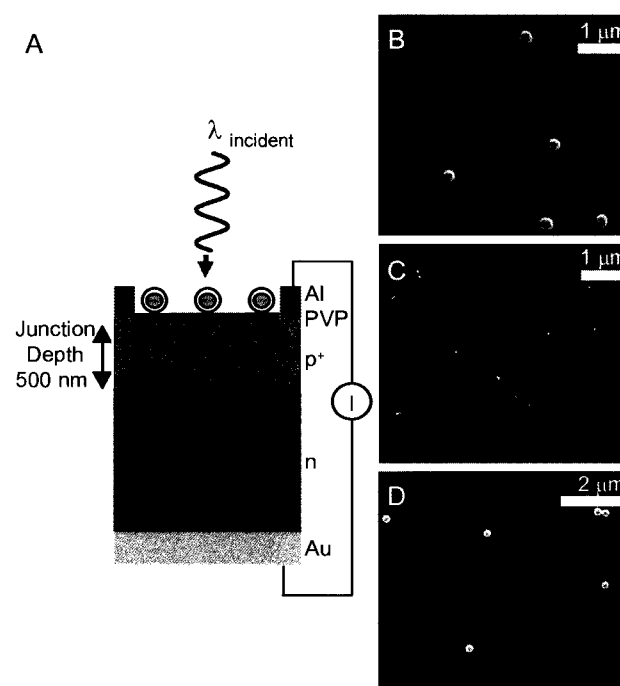


**Figure 8-1** (A) Schematic of the nanoparticle functionalized  $p^+n$  photodiode. Right: Scanning electron micrograph images, indicating representative densities of nanoparticle surface coverage on devices for (B)  $r = 60$  nm silica particles, (C)  $r = 25$  nm Au colloid, and (D)  $[r_1, r_2] = [96, 116]$  nm nanoshells.

Our experimental geometry consisted of silicon photodiodes functionalized with nanoparticles on their light collecting face (Figure 8-1A). Silicon  $p^+n$  diodes (Addison Engineering, Inc., San Jose, CA) were fabricated on 0.010-0.020  $\Omega$  cm resistivity n-type wafers. The junction depth was 500 nm, determined by destructive profiling of one of the

devices (Solecon Laboratories, Reno, NV). The surface carrier concentration within the first 200 nm of device is p-type and ranges from  $4 \times 10^{19}$  to  $1 \times 10^{20}$   $\text{cm}^{-3}$ . The front aluminum contact thickness is a 3 mm wide  $\times$  500 nm thick edging running along all four sides of the rectangular die (2.0 cm  $\times$  2.2 cm) while the back contact is a 475 nm thick gold layer coating the entire back surface. Five types of nanoparticles were used to functionalize the active face of the photodiodes. Solid silica nanospheres ( $r = 60$  nm, Precision Colloid, Cartersville, GA) and solid Au nanospheres ( $r = 25$  nm, Ted Pella, Redding, CA) were obtained commercially. Three different sizes of Au-silica nanoshells with  $[r_1, r_2] = [38, 62]$  nm,  $[r_1, r_2] = [62, 81]$  nm,  $[r_1, r_2] = [96, 116]$  nm, where  $r_1$  is the inner silica core radius and  $r_2$  is the total particle radius, were prepared on commercially available silica cores (Precision Colloids, Cartersville, GA and Nissan Chemical, Houston, TX) using the seeded growth technique previously reported. The extinction spectra in aqueous suspension for these particles are shown in Figure 8-2. The p<sup>+</sup>n photodiodes were cleaned by sonication in ethanol and dried in a stream of nitrogen. The nanoparticles were deposited from aqueous suspension onto the diode faces prefunctionalized with poly(vinyl pyridine).<sup>191</sup> The deposition times and precursor nanoparticle suspension concentrations were selected to maintain interparticle spacings much greater than the laser spot size, yet to ensure sufficiently dense surface coverage that multiple particles could be imaged in each  $15 \times 15$   $\mu\text{m}$  area scan (Figure 8-1).

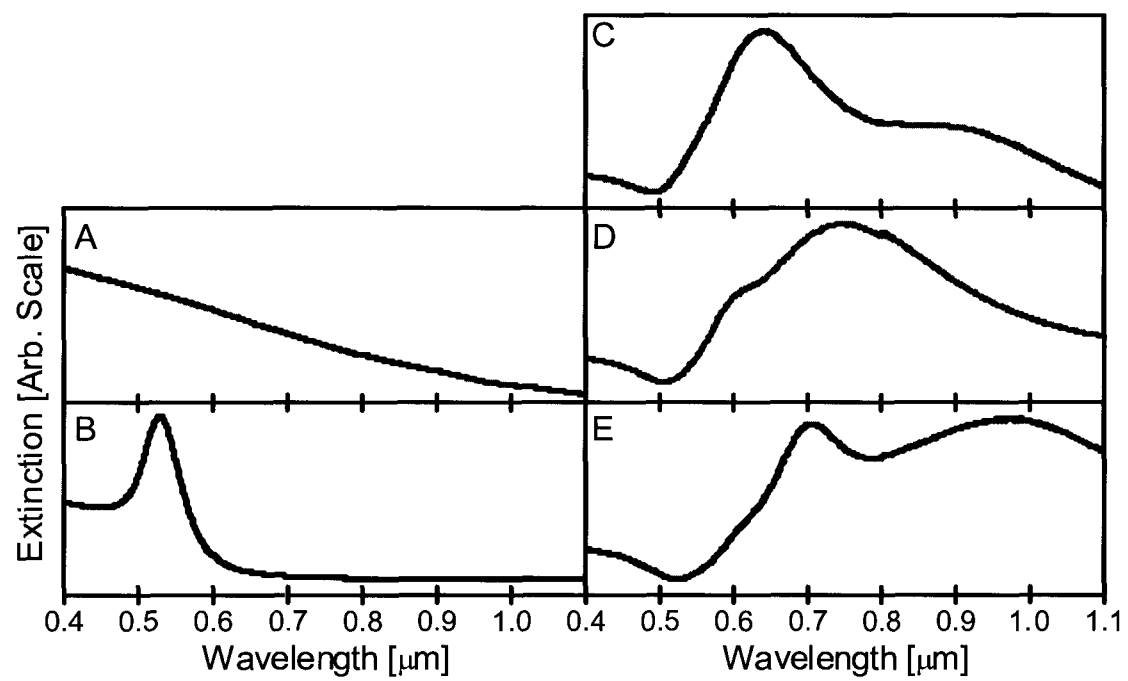


**Figure 8-2** Measured extinction spectra in aqueous suspension for: (A)  $r = 61$  nm silica nanospheres, (B)  $r = 25$  nm Au nanospheres, (C)  $[r_1, r_2] = [38, 62]$  nm nanoshells, (D)  $[r_1, r_2] = [62, 81]$  nm nanoshells, and (E)  $[r_1, r_2] = [96, 116]$  nm nanoshells.

## 8.2 Measurement

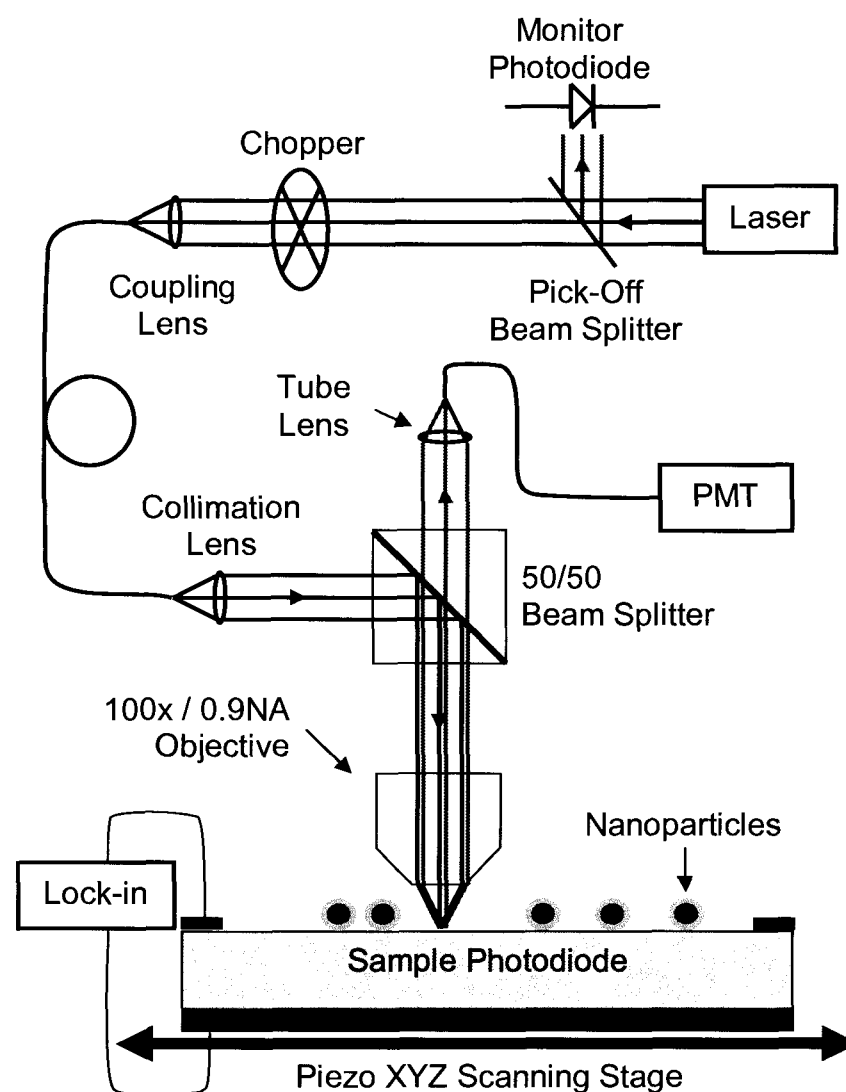


**Figure 8-3** Confocal scanning photocurrent apparatus.

Maps of the local photocurrent were obtained by scanned imaging of the functionalized photodiodes using a fiber-coupled confocal sample-scanning optical microscope, shown in Figure 8-3, with 532, 633, 785, and 980 nm wavelength laser sources ( $\alpha$ -SNOM, WITec GmbH, Ulm, Germany). A 100x/0.9 NA microscope objective provided a diffraction-limited laser spot on the surface of the photodiode. The sample is raster-scanned using a piezo stage, typically over a  $15 \times 15 \mu\text{m}$  area with  $128 \times 128$  pixels at an

integration time of 0.15 s/pixel for 532, 633, or 785 nm and 0.83 s/pixel for 980 nm. At each pixel, the reflected light (detected with a photomultiplier tube) and the photocurrent were obtained simultaneously using standard lock-in techniques (SR540 and SR850, Stanford Research Systems, Sunnyvale, CA) at a ~400 Hz chopping rate. No bias was applied to the photodiodes. The simultaneous collection of confocal reflectance and photocurrent permits the correlation of nanoparticle position with an increase or decrease of photocurrent at the same point. The incident laser power was monitored during the measurement with a silicon photodiode (DET110, Thorlabs, Newton, NJ). The incident laser intensity was adjusted to obtain a photocurrent of approximately 2.5 nA at wavelengths of 532, 633, and 785 nm and 0.6 nA at 980 nm.

To obtain the local enhancement at each nanostructure, the scan line containing the strongest photocurrent due to the particle ( $I_{particle}$ ) was obtained, then compared to the average local background level ( $I_{background}$ ) along this linear scan. The change in photocurrent due to the presence of the nanoparticle is

$$\frac{\Delta I}{I} \equiv \frac{I_{particle} - I_{background}}{I_{background}}. \quad (8-1)$$

This local determination of photocurrent enhancement due to each individual nanoparticle is advantageous because individual nanoparticle contributions can be clearly distinguished from enhancements due to variations in nanoparticle surface coverage density. In addition, this approach removes any effect of long-term laser power drift or large-range (micron or millimeter scale) spatial inhomogeneities in the response of the device structure. In our photocurrent images the nanoparticle appears bright if its presence increases the measured photocurrent and dark if its presence suppresses the

photocurrent at that location. The apparent size of the nanostructure-associated feature in the photocurrent images is a convolution of the laser spot size and the nanostructure influenced portion of the substrate. Because this measurement does not specifically resolve the topology of the nanostructure, this approach can be combined with atomic force microscopy to obtain the specific nanostructure geometry responsible for each local change in photocurrent.

### 8.3 Results

Photocurrent images for all types of nanoparticles studied at the four wavelengths used in the experiment were obtained (Figure 8-4). The images in the top row correspond to silica nanospheres of 60 nm radius, (A-D), in the second row Au nanoparticles of 25 nm radius (E-F), followed by (third row) Au nanoshells of dimension  $[r_1, r_2] = [38, 62]$  nm (I-L), and (fourth row) Au nanoshells of dimension  $[r_1, r_2] = [96, 116]$  nm. In each row, images of the same sample were obtained at the excitation wavelengths of 532, 633, 785, and 980 nm, respectively. In the four rightmost images obtained at 980 nm wavelength, individual nanoparticle features are denoted with specific symbols. The values of the changes in photocurrent  $\Delta I/I$  for the individual nanoparticles of each type, corresponding to the symbols in these four images, are plotted as percentage changes in Figure 8-5.

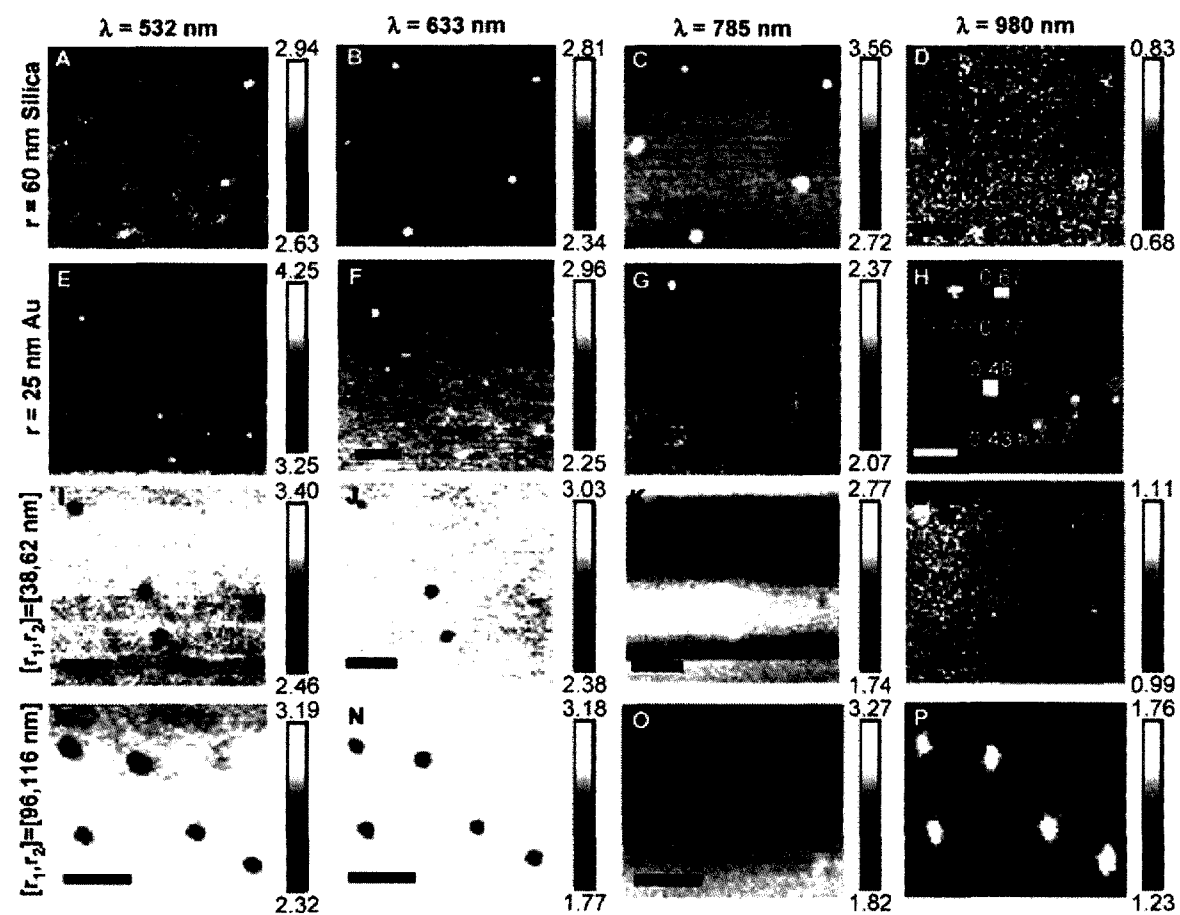


**Figure 8-4.** Photocurrent images [in nanoamperes] of (A-D)  $r = 61$  nm silica nanospheres, (E-H)  $r = 25$  nm solid Au nanospheres, (I-L)  $[r_1, r_2] = [38, 62]$  nm nanoshells, and (M-P)  $[r_1, r_2] = [96, 116]$  nm nanoshells for light incident at wavelengths of 532, 633, 785, and 980 nm. Symbols represent single nanoparticles, dimers, and higher order aggregates sampled during each scan. Scale bars are  $2 \mu\text{m}$ .

These images reveal strong, nanoparticle-dependent differences in photocurrent modification due to the properties of the various types of nanoparticles studied. (Small variations in  $\Delta I/I$  for the individual nanoparticles sampled may also arise from differences in the local environment of each nanoparticle due to variations in dopant or surface trap state density in the underlying device and nonuniformity in the PVP spacer layer.) Dielectric silica nanospheres (Figure 8-4AD) exhibit a consistent and uniform enhancement over the entire wavelength region studied. This uniform enhancement is attributed to the very similar, nonresonant scattering properties of these particles across

the measurement wavelength range. The particle-to-particle variation in enhancement is also relatively small, indicating that the nanoparticles themselves are relatively uniform in size, and well dispersed on the device with minimal or no aggregation. Au nanospheres also display a photocurrent enhancement over this wavelength range, appearing strongest at the shortest wavelength (11%) and decreasing with increasing wavelength, to 3% at 980 nm. This observed wavelength dependence is generally consistent with previously reported results that did not distinguish individual nanoparticle contributions, but also shows some variation with those results.<sup>186</sup> For example, one of the observed Au nanoparticles in this image (denoted □) shows a wavelength-dependent enhancement that deviates significantly from the other nanoparticles in the image, revealing a significantly stronger photocurrent enhancement over the entire wavelength range. This possibly may be due to the presence of a nanoparticle aggregate at that site. Small Au nanoparticle aggregates such as dimers and trimers possess a different spectrum of plasmon resonances and a larger scattering cross section due to their larger spatial extent than their individual Au nanoparticle constituents.<sup>111, 192</sup> The presence of even a small percentage of such aggregates, quite possible in the preparation of these types of nanoparticle-dispersed surfaces, may be responsible for additional photocurrent enhancements for this device geometry.

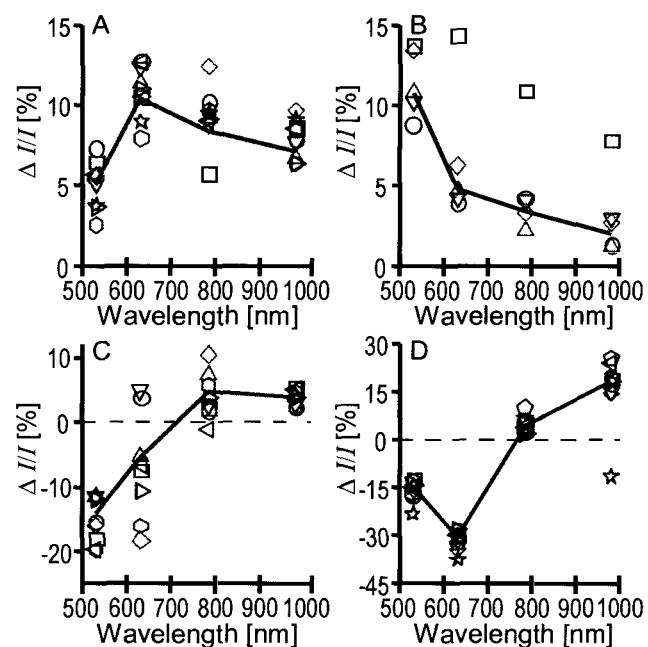


**Figure 8-5.** Local photocurrent modification for photodiodes functionalized with (A)  $r = 61$  nm silica nanospheres, (B)  $r = 25$  nm solid Au nanospheres, (C)  $[r_1, r_2] = [38, 62]$  nm nanoshells, or (D)  $[r_1, r_2] = [96, 116]$  nm nanoshells. Symbols correspond to particles marked in the rightmost column images of Figure 8-4 (Figure 8-4, panels D, H, L, and P, respectively). Solid lines indicate the trend of the average value. In panel C, the red square pertains to parameters modeled in Figure 8-7A, and the green square corresponds to Figure 8-7B.

Au nanoshells (Figure 8-4I-P and Figure 8-6A-D) exhibit a markedly different wavelength-dependent photocurrent enhancement- suppression characteristic than either silica or Au nanospheres. Two different sizes of nanoshells were investigated: Figure 8-4I-L shows the photocurrent images of  $[r_1, r_2] = [38, 62]$  nm nanoshells, and Figure 8-4M-P shows the  $[r_1, r_2] = [96, 116]$  nm nanoshell photocurrent maps. With increased total particle size, the proportion of scattering to absorption in the total extinction cross section will increase, and multipolar plasmon modes will contribute more significantly to the overall nanoshell plasmon response.<sup>47, 54, 95, 193</sup> The dipolar plasmon resonances for the  $[r_1, r_2] = [38, 62]$  nm and  $[r_1, r_2] = [96, 116]$  nm nanoshells suspended in H<sub>2</sub>O occur at 650 and 960 nm, respectively, and a quadrupolar resonance at 697 nm is also present for

the  $[r_1, r_2] = [96, 116]$  nm nanoshells (Figure 8-2). On a highly refractive substrate such as the silicon device studied here, the resonance frequencies of plasmonic nanoparticles are expected to redshift and higher order multipole plasmon modes should be preferentially enhanced.<sup>89, 156, 194-197</sup>

Both the small and large nanoshells suppress the photocurrent at wavelengths of 532 and 633 nm and enhance the photocurrent at wavelengths of 785 and 980 nm (Figure 8-5C,D and Figure 8-6F), where the larger nanoshells show the larger photocurrent suppression and enhancement. The strongest photocurrent suppression (30%) is due to the  $[r_1, r_2] = [96, 116]$  nm nanoshells at a wavelength of 633 nm (Figure 8-4N and Figure 8-5D). The maximum photocurrent enhancement observed in these experiments, nominally 20%, was observed at 980 nm excitation for these larger nanoshells. In this case, the forward scattering of light into the device is enabled both by the strongly scattering character of the nanoshell dipolar resonance for a nanoparticle in this size range<sup>54</sup> and by the greater transmissivity of the 980 nm wavelength light in silicon. These large observed enhancements have important technological implications for long-wavelength sensitization of silicon photodetectors into the near IR for imaging applications, as well as for expanding the spectral response of silicon-based solar cells in that wavelength region as well. However, long wavelength photocurrent enhancement comes at the cost of shorter wavelength photocurrent suppression, a property that may impact device or nanoparticle design or applications.

By combining photocurrent imaging with atomic force microscopy, the specific nanoparticle geometry associated with each enhancement-suppression feature in the

photocurrent images can be determined. This approach allows us to discriminate between the photocurrent modification due to isolated nanoshells and nanoshell aggregates also deposited on the active surface of the device. An AFM tip mounted below a standard 50× long working distance microscope objective and positioned using a high-precision piezo stage in our microscope permits the acquisition of AFM images and photocurrent images of the same area of the sample with systematic offsets of at most a few microns. This combined photocurrent-AFM measurement is seen in the case of intermediate sized  $[r_1, r_2] = [62, 81]$  nm nanoshells on Si photodiodes (Figure 8-6). A clear visible correlation between the individual nanoshells and nanoshell aggregates observed in the AFM topographic image in Figure 8-6E and the photocurrent images of Figure 8-6A-D is easily observable. In Figure 8-6E, the presence of both individual isolated nanoshells and nanoshell dimers and occasionally larger aggregates can be seen. From these data, we can clearly distinguish between the photocurrent suppression-enhancement characteristics of individual nanoshells and nanoshell aggregates. In contrast to the photocurrent suppression-enhancement characteristic of individual nanoshells, most of the nanoshell dimers suppress the photocurrent at all four wavelengths (Figure 8-6G). This is also in contrast to the nanoparticle aggregate case observed in Figure 8-5B, which results in photocurrent enhancement. The magnitude of the photocurrent suppression in the case of nanoshell aggregates is likely to be related to the large scattering cross section of the aggregates and may also be influenced by nanoshell dimer properties such as interparticle distance, including the cases of touching or fused dimers<sup>112, 192, 198</sup> and relative orientation of the dimer axis with respect to the polarization of the incident light. This type of

broadband photocurrent suppression would no doubt be deleterious to device performance; for this device geometry nanoshell aggregates should clearly be avoided.

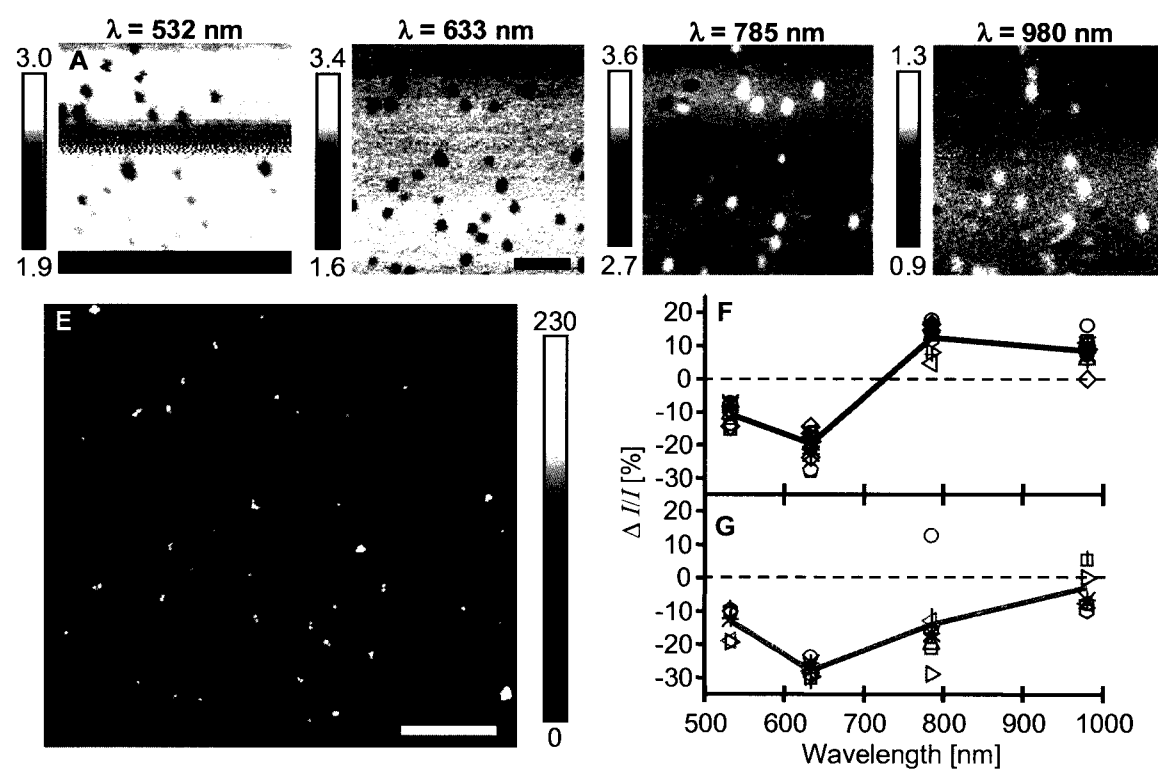


**Figure 8-6.** Photocurrent images [in nanoamperes] of (A-D)  $[r_1, r_2] = [62, 81]$  nm nanoshells for light incident at wavelengths of 532, 633, 785, and 980 nm. (E) Topographic (AFM) image of the same area shown in panels A-D, revealing individual nanoparticle geometry. Scale bars all correspond to  $3 \mu\text{m}$ . Individual nanoshells are highlighted in magenta, nanoshell dimers in green. In panels A-E, the blue inset boxes mark a representative subset of nanoparticles replicated in each image but with varying influence on the photocurrent. (F) Photocurrent modification for isolated nanoshells and (G) dimers of nanoshells. Solid lines represent average trend. Each symbol in panels F and G corresponds to one of the marked particles in panel E.

In general, the nanoparticle-induced photocurrent changes that are observed are related to the interference between the light scattered from the nanoparticle into the device and the light transmitted directly into the input face of the device.<sup>186</sup> The relative phase of these two input waves results in constructive or destructive interference, which may affect photocurrent generation if a constructive or destructive node occurs in the active region

of the device. For plasmon resonant nanoparticles in particular, the behavior of the forward scattered wave can be quite complex.<sup>199-201</sup> Previous theoretical studies of plasmon resonant nanoparticles in vacuum have shown that the forward scattered field for frequencies on or near the plasmon resonance of the nanoparticle may have vortexlike characteristics and a spatial structure that depends quite sensitively on the properties of the nanoparticle. It seems quite plausible that this vortexlike behavior may also be present for the case of a nanoparticle in vacuum with forward scattering into a Si medium and more generally may be an important property of plasmonic nanoparticle-induced light scattering into larger devices and materials.

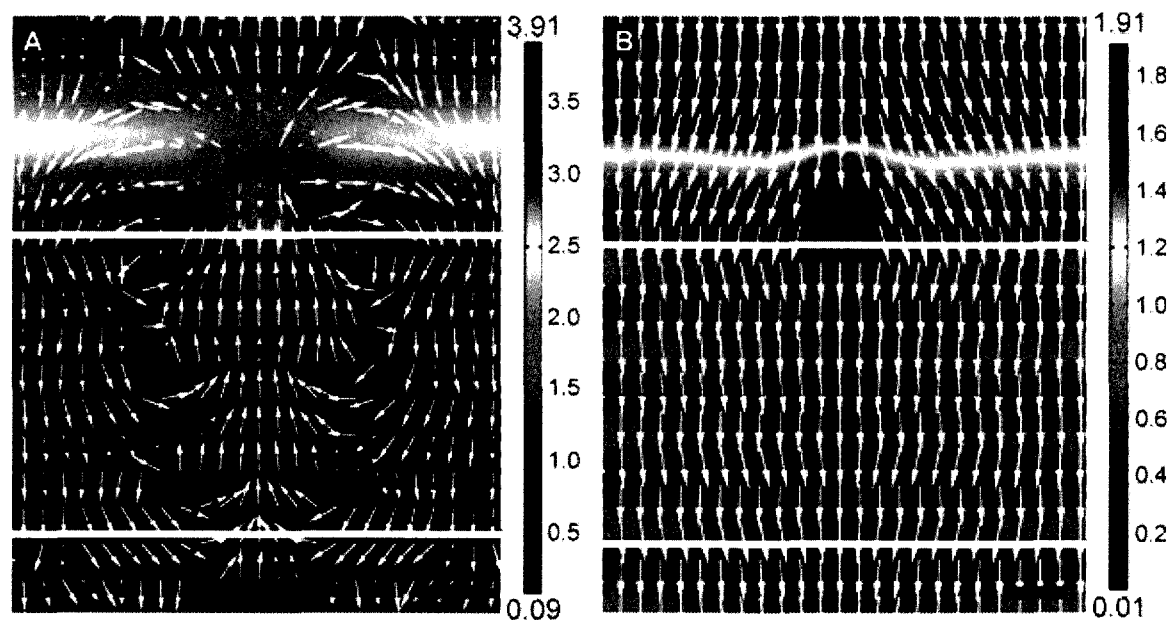


**Figure 8-7.** Poynting vector field plots show power flow through a  $[r_1, r_2] = [38, 61]$  nm nanoshell on a Si slab at (A) 633 nm and (B) 980 nm, corresponding to the data points shown in Figure 8-5C enclosed in red and green, respectively. Arrows are normalized for power flow magnitude and indicate direction of power flow. The top and bottom white lines indicate the air-Si interface at  $z = 0$  and at a depth of 500 nm, respectively. These cross sections are in the  $yz$  plane, perpendicular to the incident light polarization. The Poynting vector field is overlaid onto the norm of the vector electric field (indicated by colorbar).

To further examine the unusual enhancement-suppression characteristic of nanoshells in this basic device geometry, finite element simulations were performed for  $[r_1, r_2] = [38, 61]$  nm nanoshells on a silicon slab using the commercially available COMSOL modeling package. The incident light was modeled as a plane wave linearly polarized in the  $x$ -direction, propagating into the device ( $z$ -direction). Mirror boundary conditions were applied at lateral faces of the simulation domain. These boundary conditions were chosen to best approximate the sparse surface coverage regime studied experimentally where adjacent nanoparticles are spaced by several particle diameters and interparticle interactions are minimal. The period of the square array of nanoparticles thus simulated is set by the  $x$  and  $y$  extent of the simulation domain. In a regime where the domain extent was not sufficiently large, interparticle interactions were manifest as spots of intense electric field near the domain boundaries. In the case of a  $[r_1, r_2] = [38, 61]$  nm nanoshell, a simulation domain size of 800 nm in both  $x$ - and  $y$ -directions was used. This extent was found to be sufficiently large to avoid interparticle interaction effects due to strong scattering of light by the nanoshell. The extent of the slab in the  $z$ -direction was 1.5  $\mu\text{m}$ . A scattering boundary condition was applied at the exit face, and a perfectly matched layer absorbing in the  $z$ -direction was implemented adjacent to it to eliminate extraneous reflections. The dielectric functions for Au and Si were obtained from Johnson and Christy<sup>50</sup> and Adachi,<sup>202</sup> respectively.

The parameters used in this simulation correspond to experimental parameters that showed unusual and contrasting behavior. In our experimental data, the 633 nm photocurrent images for  $[r_1, r_2] = [38, 61]$  nm nanoshells showed an anomalously wide variation in modified photocurrent, varying from +5 to -20% (Figure 8-5C, red). In

contrast, the photocurrent measurements for the same nanoparticles on the same sample at 980 were quite consistent and well behaved (Figure 8-5C, green), indicating that the large variation observed in the 633 nm data was not due to inhomogeneities in the nanoparticles or the device. In Figure 8-7, the Poynting vector field through the Si slab is overlaid onto the electric field magnitude in the  $yz$  plane for the case of an  $[r_1, r_2] = [38, 61]$  nm Au nanoshell is shown for 633 and 980 nm wavelength incident plane waves. At 633 nm (Figure 8-7A), the presence of the nanoshell clearly disrupts the power flow well into the Si slab. Vortexlike behavior<sup>199,203</sup> of the forward scattered field is clearly observed in this simulation, throughout the depth of the Si slab used to model the device. At this incident wavelength, the average energy flow across this plane is directed toward the surface and toward the nanoparticle with the energy concentrated near the nanoparticle-silicon interface. In contrast, at the incident field wavelength of 980 nm (Figure 8-7B) the scattered light into the device is well behaved with energy flow directed toward the bottom surface of the device and with a uniform distribution of energy throughout the entire simulation region. This type of behavior may need to be an important consideration in devices where plasmonic nanoparticles are used in light collection or transmission and also may be relevant to the properties of other types of nanoantennas, such as nanofabricated bowtie structures, implemented on device structures for the same light-harvesting function.

#### 8.4 Conclusions

In conclusion, we have investigated nanoparticle-induced photocurrent enhancement and suppression in a silicon photodiode, focusing on the influence of the nanoparticle properties on this effect. Imaging the changes in photocurrent due to individual

nanoparticles positioned on the active face of the device has allowed us to investigate the effect of specific nanoparticle type, which will be directly relevant to enhancing device efficiencies. Several important conclusions are obtained from this study. While plasmonic nanoparticles have been of interest for photocurrent enhancement in these types of device structures, this study also indicates that nonresonant dielectric nanoparticles provide photocurrent enhancement over a wide wavelength range. Therefore silica nanoparticles should be considered promising candidates for boosting light-harvesting efficiencies at low cost in certain types of devices. Plasmonic nanoparticles have quite widely varying enhancement-suppression characteristics, depending on nanoparticle size, geometry, and plasmon resonance wavelength, which may lend themselves most favorably to specific applications such as sensitizing the response of photodetectors over specific wavelength regions. However, where individual nanoparticles may provide photocurrent enhancement at certain wavelengths, aggregates of the same nanoparticle may in fact suppress photocurrent at those same wavelengths and degrade device performance, an important fabrication and manufacturing consideration. Finally, for certain cases the energy flow associated with the forward scattered field of a plasmonic nanoparticle exhibits a complex spatial structure. This vortexlike behavior may very well influence photocurrent enhancement at the wavelengths where it occurs. While this property had been previously studied theoretically for the case of a metallic nanoparticle in vacuum, our observations may indicate that this interesting behavior may be quite important in the design and development of nanoparticle-enhanced light-collecting devices such as infrared detectors and solar cells.

## **Chapter 9. Optically-Driven Collapse of a Plasmonic Nanogap Self-monitored by Optical Frequency Mixing**

Metallic nanostructures are one of the most versatile tools available for manipulating light at the nanoscale. These nanostructures support surface plasmons, collective excitations of the conduction electrons, which can exist as propagating waves at a metallic interface or as localized excitations of a nanoparticle or nanostructure. The interaction between plasmons on adjacent metallic nanostructures is a sensitive function of interparticle spacing. Control of this nanoscale spacing allows for great flexibility in tuning the spectral response of complex multilayer or aggregate nanostructures, controlling the focusing of light in the near field region of a nanostructure, or, conversely, controlling the outcoupling of electromagnetic energy from surface plasmons to far field, free space radiation. Structures where interacting plasmons supported by adjacent nanostructures dominate the optical response include dimers or aggregates of nanoparticles,<sup>7, 8, 30, 204-207</sup> multilayer core-shell nanoparticles such as nanoshells or nanomatryushkas,<sup>26</sup> and nanoparticles adjacent to metallic surfaces or extended wires<sup>194, 208-213</sup>.

The vast majority of previous studies of interacting plasmons have focused on stationary geometries or, more recently, systems where the interaction between plasmons is controlled by external means. Examples include breaking symmetry in an initially spherical nanoshell by electron-beam ablation<sup>214</sup> and controlling the separation between adjacent nanospheres by affixing one of the Au nanospheres to the end of a scanning probe microscopy tip<sup>7</sup>. While these methods have allowed the interaction between nanostructures to be investigated, direct optical manipulation of plasmonic structures

with spatial precision on the few-nanometer scale could provide a new approach to controlling interacting plasmonic systems in a highly sensitive manner.

The intense focusing of light into a plasmonic gap, known as a “hot spot”, is most popularly known as a mechanism for enhancing the nonlinear optical process of surface enhanced Raman scattering (SERS).<sup>8, 30, 205</sup> However, a variety of nonlinear optical responses can be generated in nanoscale metal-insulator-metal junctions, since the phase-matching requirements for nonlinear optics in conventional macroscopic media are relaxed in this geometry.<sup>215-218</sup> For example, four wave mixing (FWM), where optical fields  $\vec{E}(\omega)$  at frequencies  $\omega_1$ , and  $\omega_2$  induce the nonlinear polarization  $\vec{P}^{(3)}(\omega_{FWM} = 2\omega_1 - \omega_2) = \epsilon_0 \vec{\chi}^{(3)}(\omega_{FWM}; \omega_1, \omega_1, \omega_2) : \vec{E}(\omega_1) \vec{E}(\omega_1) \vec{E}^*(\omega_2)$  has been observed in nanoscale junctions.<sup>7, 204</sup> The third order nonlinear susceptibility tensor  $\vec{\chi}^{(3)}$  accounts for the intrinsic nonlinear response of the material(s). The FWM signal can be generated with multiple discrete single frequency laser sources, but also, more conveniently, within the broad spectral envelope of an ultrashort continuum laser pulse. In the context of plasmonics, FWM has previously been used in apertureless near field scanning optical microscopy (ANSOM) to characterize the approach and contact of a particle attached to a cantilever with another particle or on an underlying substrate<sup>7</sup> and as a nanoscale light source<sup>204</sup>. The relative enhancement of FWM from isolated Au nanorods as a function of rod geometry has been shown to agree with a straightforward electromagnetic model, and is suitable for use as an optical contrast agent when imaging cells.<sup>219</sup> Recently, quantitative measurements of surface-enhanced FWM from macroscopic planar Au films imprinted with a grating structure and smooth Au films have been performed.<sup>220</sup>

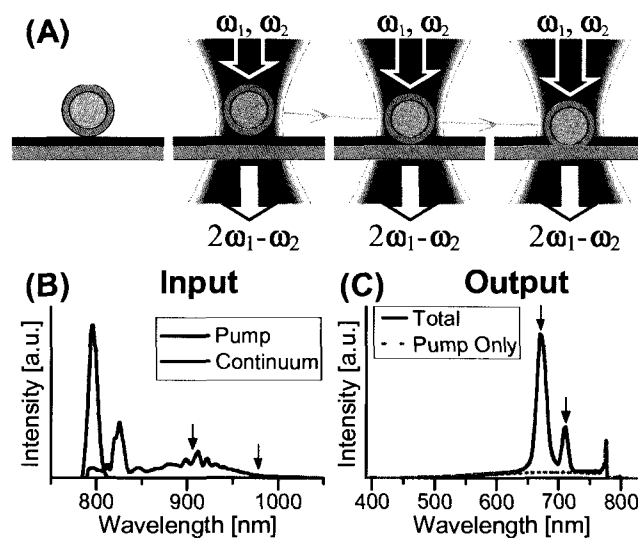


**Figure 9-1** (A) Schematic illustration of the experiment. Lasers at frequencies  $\omega_1$  and  $\omega_2$  are applied to the nanoshell over film structure, both generating a four wave mixing (FWM) signal at  $2\omega_1 - \omega_2$  and driving the particle into the film. (B) Spectrum of the applied pump and continuum laser fields. Note that the relative amplitude of the continuum has been exaggerated for visibility. (C) Example output FWM spectrum obtained when both the pump and continuum are applied (solid black) and the background TPPL when only the pump is applied (dotted orange). Two strong peaks in the FWM ( $2\omega_1 - \omega_2$ ) are observed at 671 nm and 710 nm, indicated by green and blue arrows, respectively. The corresponding frequencies in the continuum ( $\omega_2$ ), 978 nm and 906 nm, which mix with the pump ( $\omega_1$ ) at 796 nm to generate these peaks are indicated with the correspondingly colored arrows in (B). The spectral feature at  $\sim 775$  nm is the edge of the short pass filter used to block the excitation light.

Here we report the surprising observation that the illumination of an individual Au nanoshell-over-Au film with a nanoscale organic dielectric spacer – a “nanogap” - with ultrashort optical pulses at its plasmon resonance frequency results in a continuous, monitorable collapse of the nanogap. An easily detectable FWM signal is generated from this structure, due to the subwavelength light focusing of this geometry. The amplitude of the FWM signal generated in the nanogap provides a continuous, highly sensitive optical monitor of the nanogap spacing while it is being optically reduced. The dramatic increase in this signal upon contact provides a clear, unambiguous signal of the gap closure. Here we perform both a physical manipulation on the few-nm scale using light, and detection

of the local electromagnetic field during the ongoing process, with the same incident beam that drives the process. This optical manipulation and monitoring can easily be performed on individual gaps; in fact, this method is so sensitive to each specific nanoscale geometry that significant gap-to-gap variations are easily observed. This approach could potentially be exploited as a technique to fine-tune the near field optical response of individual nanoscale junctions beyond the practical limits of existing nanoscale fabrication methods.

The nanogap structure consists of an Au nanoshell separated from a thin Au film by a polymeric spacer layer, forming the nanogap (Figure 9-1). In this geometry, nanoshell plasmons interact strongly with the plasmons supported by the film, forming hybrid plasmon modes<sup>208, 210</sup>. This results in a discrete localized plasmon in the near-infrared (NIR) and a broader delocalized plasmon at lower energies arising from the interaction of the nanoshell plasmon with a continuum of surface plasmons in the metallic film substrate. This structure is important because it can focus electromagnetic energy into the nanogap, creating an intense hot spot between nanoparticle and film, allowing efficient coupling between far field radiation and launching surface plasmons along a film or waveguide.<sup>111, 211-213, 221, 222</sup>

### **9.1 Apparatus**

A simple sample-scanning nonlinear optical microscope was constructed and used to illuminate the nanostructures and measure the FWM signal (Figure 9-2). This approach allowed us to examine the light-induced collapse of individual nanogaps. An ultrafast Ti:Sapphire laser was used to generate 85 fs pulses centered at a wavelength of 795 nm

(Mira 900, Coherent Inc.). Most of this light was passed through a photonic crystal fiber (FemtoWhite 800, Crystal Fiber A/S) to generate a continuum. In this way, a wide range of frequencies spanning the visible and NIR was obtained. The remaining light from the laser was used as the pump beam. Directly out of the laser, the pump beam includes a non-zero background at wavelengths well short of the center of the spectral envelope of the pulse. This overlaps with the spectral region of the FWM signal and therefore must be blocked in order to measure the nanogap FWM signal. A dispersionless short pass filter, consisting of a folded single grating / lens  $4f$  pulse compressor<sup>223</sup> with a sharp edge inserted at the Fourier plane (cleaved edge of a thin Si wafer), removed all light from the pump beam in the spectral region of the FWM signal. The continuum and pump were then superimposed spatially using a metallic beam splitter (OD 0.3 Inconel reflective neutral density filter, ND03B, Thorlabs). A computer-controlled variable delay line was inserted into the continuum beam path to overlap the pulses in time. The collinear, copolarized beams were then focused onto the sample using a 60x / 0.8NA microscope objective (HC PL FLUOTAR, Leica). The pump and continuum were attenuated using gradient neutral density filters to provide an average input power at the objective of 350  $\mu\text{W}$ , comprised of 210  $\mu\text{W}$  from the pump laser and 140  $\mu\text{W}$  from the generated continuum. Transmitted light was collected using a 40x / 0.6NA objective (LUCPlan FL N, Olympus) with a variable cover slip correction collar. It was filtered with a pair of short pass filters (10SWF-850-B, Newport and SP01-785RU-25, Semrock) to remove the excitation light, imaged onto the input slit of a 300 mm focal length spectrograph (SpectraPro 400i, PI/Acton) by an  $f = 40$  mm cemented achromatic doublet lens (AC254-040-A, Thorlabs), and detected by a Si CCD array (PIXIS 100, PI/Acton). In this way,

the FWM signal, TPPL induced by the pump, and a small fraction of the input light that leaks through the filters can all be observed simultaneously. A weak second harmonic signal, arising from the pump beam along focused into the nanogap, can also be detected (observable as small feature near 398 nm in the spectrum shown in Figure 9-1C). Samples were mounted on a 3 axis closed-loop piezoelectric translation stage (P-545.3R2 NanoXYZ, Physik Instrumente (PI) GmbH) in order to precisely place the desired nanostructures at the focus of the excitation light. It was critical to ensure that drift in the position of the nanoparticle relative to the excitation laser was insignificant in order to unambiguously measure the time-dependent evolution of the FWM signal. A sufficient amount of the pump light at 795 nm passes through the short pass filters to monitor variations in the transmitted pump signal from the obtained spectra. For the data presented, the pump signal variation was below the noise limit, indicating that any instability in the apparatus did not have a significant effect on these measurements.

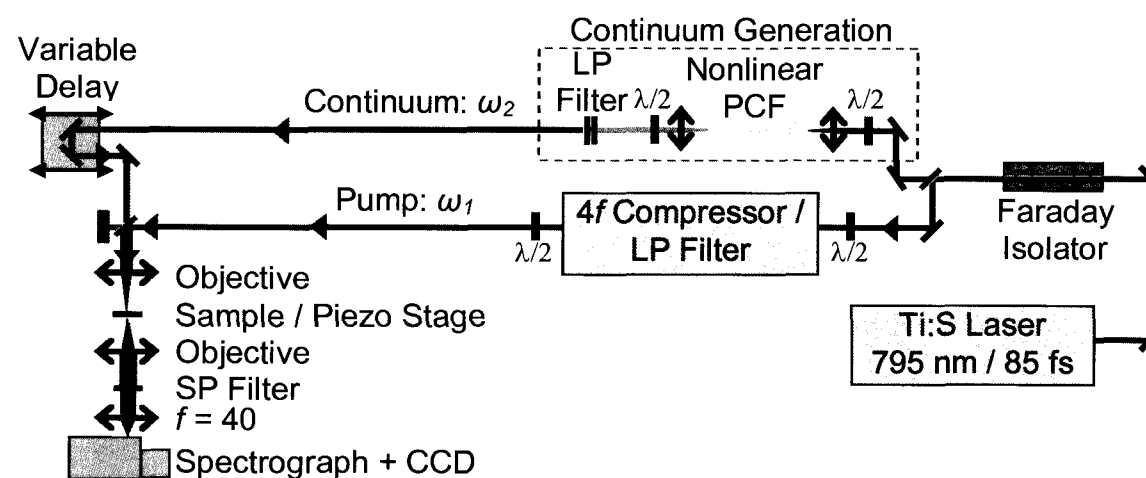


**Figure 9-2** Experimental apparatus used to measure FWM. SP Filter is a combined dielectric and colored glass 785 nm short pass filter, LP Filter is a dielectric 795 nm long pass filter, and  $\lambda/2$ s are half-wave plates.

The nanogap near field was monitored by the mixing of a strong pump pulse centered at  $\omega_1 = 795$  nm, with the continuum generated from the same laser pulse, spanning a range of frequencies  $\omega_2$ , to generate a four wave mixing signal  $\omega_{FWM} = 2\omega_1 - \omega_2$ . The input pump laser was centered at 795 nm in wavelength and the continuum spans several hundred nanometers to the long wavelength side of the pump laser wavelength (Figure 9-1B). Here the continuum intensity has been magnified relative to the pump; in the actual experiment, the spectral power density of the continuum was significantly weaker than that of the pump. The geometry of the nanoshell-over-film structures was designed to put the localized plasmon mode in resonance with the pump laser and a portion of the continuum. When the pump and continuum were incident on a nanogap, the resulting spectrum, shown in Figure 9-1C, consisted of a strong, peaked FWM signal on top of a weak, two-photon photoluminescence signal. Due to the complex temporal structure of the continuum pulses<sup>224, 225</sup> used in this experiment, only part of the continuum temporally overlaps the pump pulse. This results in a FWM signal that is strongly peaked and covers a much smaller range of frequencies than would be expected from the entire spectral extent of the continuum. Adjusting the time delay between the pump and continuum pulses would result in the appearance of different peaks in the FWM spectrum than those in Figure 9-1C. While the plasmonic properties of the cylindrically symmetric structures investigated here do not depend on the polarization of the excitation in the plane of the sample, the relative polarization of the pump and continuum fields will change the polarization and intensity of the FWM signal. In the present experiment, only the case where the pump and continuum are polarized in the same direction is considered, since this configuration results in the strongest signal.

## 9.2 Sample Fabrication

Samples were fabricated by depositing Au nanoshells<sup>26</sup> either directly onto a thin Au film or separated from the Au film by a thin polymer spacer layer. Electron-beam evaporation was used to deposit 15 nm thick Au films onto glass microscope slides with an intervening 1.5 nm thick Ti to promote adhesion of the Au film to the glass slide. A quartz crystal thickness monitor was used to determine the film thickness. Three distinct structures were investigated: Au nanoshells directly in contact with the Au film, Au nanoshells separated from the film by a thin polymer spacer layer, and Au nanoshells separated from the film by a thick polymer layer. For the case of no spacer layer, nanoshells were spin-coated directly from aqueous suspension onto the Au surface. To obtain a small gap, poly(diallyl dimethylammonium) chloride (PDDA) was deposited on the Au film by immersing the slide in a 2 % w/v aqueous solution for ~15 min. The films were then rinsed with a copious amount of ultrapure water. Nanoshells were again deposited by spin-coating from aqueous suspension. This results in a ~ 1 nm gap between the nanoshell and the Au film.<sup>169, 226-229</sup> In addition to creating a well-defined gap, PDDA also acts as an electrostatic adhesion layer and renders the surface hydrophilic resulting in a more uniform nanoshell film with less aggregation. Electrostatic layer-by-layer deposition<sup>169, 226-229</sup> was used to create a substantially thicker spacer layer for control experiments. For this, the Au-coated slide was alternately immersed in a 2 % w/v aqueous solution of PDDA and a 2 % w/v aqueous solution of poly(styrene sulfonate) (PSS) for 15 min, with a thorough rinse under ultrapure water between each step. The final PDDA / [PSS / PDDA]<sub>2</sub> multilayer procedure created a gap of approximately 6 nm between the nanoshell and the film. Due to the difficulty in measuring the thickness of

such thin transparent films with high precision, the thickness is assumed to be similar to that reported in previous studies.<sup>169,226-229</sup> A thin, electroformed Cu or Ni plate with cut-outs forming an indexed grid (100 mesh Cu micron index 1 TEM grids from Ted Pella, Inc., or 100 mesh Ni EF100-Ni TEM grids from Electron Microscopy Sciences, Inc.) was affixed to the top of the sample with a very small amount of quick-drying epoxy. This provided index marks suitable for correlating optical and electron micrographs. The fabricated structures with a spacer layer are illustrated on the left of Figure 9-1A.

### 9.3 Results

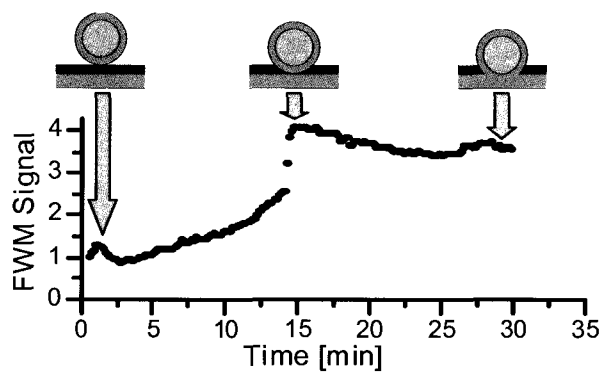


**Figure 9-3** Temporal evolution of the normalized FWM signal at  $\omega_{FMW} = 680$  nm for an  $[r_1, r_2] = [90, 104]$  nm nanoshell initially held  $\sim 1$  nm above the surface of a 15 nm thick Au film by a single layer of PDDA.

In Figure 9-3, the FWM signal at 680 nm, corresponding to a pump at  $\omega_1 = 795$  nm mixing with  $\omega_2 = 957$  nm from the continuum, is plotted as a function of time. This signal is characteristic of all signals obtained from nanogaps with small dielectric spacer layers: the FWM signal was observed to increase slowly and smoothly for approximately the first 15 minutes, which varied slightly from nanogap to nanogap, then jump abruptly with an amplitude that varied slightly from nanogap to nanogap. Following this increase, the change in FWM typically showed a slow decay and then a slight increase in FWM at longer times. The total incident average power / pulse energy is  $350 \mu\text{W} / 4.6 \text{ pJ}$ ,

comprised of 210  $\mu\text{W}$  / 2.8 pJ of pump and 140  $\mu\text{W}$  / 1.8 pJ continuum. Spectra were obtained continuously with a 10 s integration time for 30 – 45 min. At this level of incident laser power, any signal from the PDDA/Au film not in the direct vicinity of the nanoshell is not detectable. The signal at all time points was normalized to the first spectrum obtained on each system.

This unusual slow evolution of the FWM signal occurs for all nanogaps of this geometry. We hypothesize what changes in the nanogap may be occurring that correspond to these changes in the FWM signal amplitude. The evolution of the actual nanogap, based on this complex optical signal, is captured by the inset illustrations in Figure 9-3. The initial slow increase in FWM signal amplitude corresponds to a gradual “reduction” or “compression” of the nanogap due to illumination by the incident laser pulses. The abrupt rise observed appears to correspond to a “shorting” of the nanogap, that is, the opening of a conductive (tunneling) path between the nanoparticle and the supporting metallic film. At longer times, changes in the FWM signal still occur, and this may possibly be due to the nanoparticle being pushed into the metallic film substrate by the radiation pressure of the incident light pulses, or a possible deformation of the nanoshell.

To critically examine the origin of this characteristic evolution of the nanogap FWM signal, we modeled the electromagnetic response of the nanogap using the finite element method (FEM) (COMSOL Multiphysics 3.5a, RF Module). An  $[r_1, r_2] = [90, 104]$  nm nanoshell over a 15 nm thick Au film with a varying gap size was simulated. The far-field scattering was calculated using far-field transforms evaluated on a hemispherical space in the backscattered direction. To simulate an infinite space, the simulation was

surrounded by a layer of perfectly matched layers (PMLs) with scattering boundaries on the outermost surface. The metal film was terminated with a matched impedance boundary to prevent reflections from creating standing waves on the Au surface. For nanoshells embedded in the film, a 1.0 nm radius of curvature was imposed at the gap to ensure a well-defined structure with the grid constrained to enforce a maximum element size of 0.5 nm in this region. No changes in the studied quantities were found for a test simulation performed with the grid constrained to 0.25 nm elements in the gap region. The resulting simulations consisted of approximately 250k – 1M degrees of freedom and were solved using the direct PARDISO solver.

The fields at  $\omega_1$ ,  $\omega_2$ , and  $\omega_{FWM}$  all need to be considered to evaluate the dependence of the FWM signal on gap size. Enhancement of the emission due to antenna effects are estimated by applying a factor of the local field enhancement, as is generally done for calculations of SERS enhancement.<sup>230</sup> The intensity of the FWM signal is proportional to the product of the field enhancement at the emission wavelength and the square of the induced polarization  $P^{(3)}(\omega_{FWM})$ , yielding:

$$I(\omega_{FWM}) \propto G^2(\omega_{FWM}) |\tilde{\chi}^{(3)}|^2 G^4(\omega_1) |\bar{\mathbf{E}}(\omega_1)|^4 G^2(\omega_2) |\bar{\mathbf{E}}^*(\omega_2)|^2, \quad (9-1)$$

where  $G(\omega)$  is the local field enhancement,  $\bar{\mathbf{E}}(\omega)$  is the applied field, and polarization effects due to the tensorial nature of  $\tilde{\chi}^{(3)}$  have been neglected. Assuming that only the field enhancements vary appreciably as a function of gap geometry, the relative variation in the FWM signal should be proportional to  $G^4(\omega_1)G^2(\omega_2)G^2(\omega_{FWM})$ . This quantity was integrated over the volume in which the FWM signal was generated, that is, the volume where  $\tilde{\chi}^{(3)}$  is thought to be significant. A previous study of FWM from Au nanorods

showed that this approach was consistent with experimental measurements.<sup>219</sup> This model allows us to examine the relative change in the FWM signal as a function of gap size consistent with our experimental system.

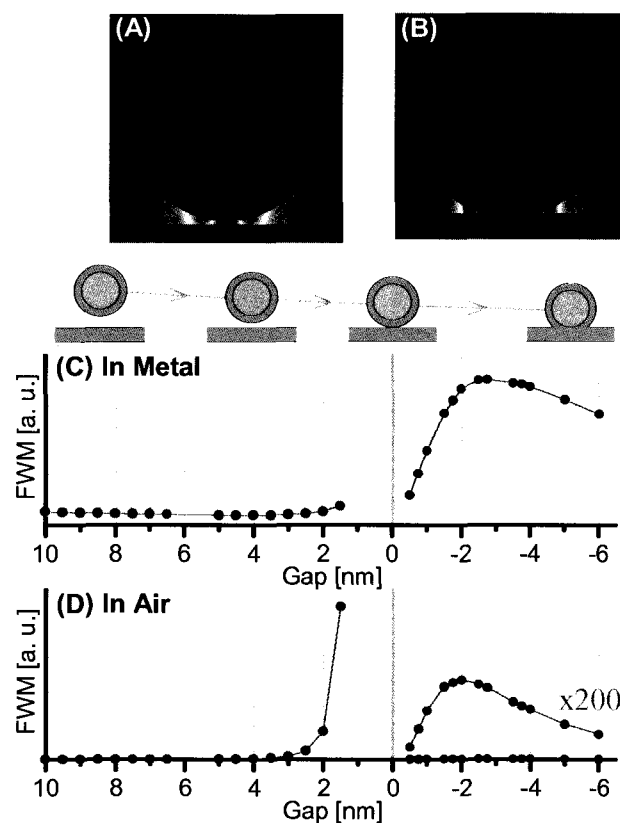


**Figure 9-4** Field enhancements for an  $[r_1, r_2] = [90, 104]$  nm Au nanoshell on a 15 nm thick Au film with a gap of (A) +5 nm and (B) -5 nm at 795 nm shown with the same color scale. The behavior of the FWM signal as a function of gap can be obtained by integrating  $|E(\omega_1)|^4 |E(\omega_2)|^2 |E(\omega_{FWM})|^2$  over the region containing the nonlinear material. In this case, the integral is carried out over either the metal (C) or in the air outside the metal (D). Gray lines are a guide to the eye.

The results of this study are shown in Figure 9-4. Figure 9-4A and Figure 9-4B show the calculated field enhancements in a nanogap at the pump wavelength, 795 nm, for a nanoshell located above a dielectric gap 5 nm above the film (gap = +5 nm) and for a nanoshell embedded 5 nm into the film (gap = -5 nm). We calculated Eq. 9-1 for this geometry as a function of nanogap size, for the case of nanoshell-film contact, and for the

case where the nanoshell begins to become embedded into the metal film substrate. Since our comparison is between the same system with small changes in geometry, it was assumed that  $\tilde{\chi}^{(3)}$  maintained its characteristic values for all materials and was not calculated explicitly. The integration volumes were varied to address two different cases, (i) assuming that the FWM signal originates from within the metallic structures forming the nanogap, and (ii) assuming that the signal originates in the dielectric spacer layer “hot spot” and its local vicinity. This was done by varying the size and shape of the integration volume. The results of both (i) and (ii) are shown in Figure 9-4C and Figure 9-4D, respectively. As the nanoshell-film gap becomes extremely small and approaches conductive contact, the classical approximation inherent in this theoretical approach breaks down:<sup>231,232</sup> therefore, we only examine the results of this model before and after conductive contact is made.

By comparing the theoretical trends in Figure 9-4C and Figure 9-4D with the experimentally measured variations shown in Figure 9-3, it appears that the experimentally observed FWHM signal is most likely generated within the metal features of the nanogap. This is consistent with existing experimental results that indicate that Au has a substantial cubic nonlinearity at femtosecond time scales arising from the hot electrons which decays rapidly as the electrons thermalize with the lattice, with an effective  $\tilde{\chi}^{(3)}$  orders of magnitude larger than nonresonant dielectric media.<sup>220,233,234</sup>

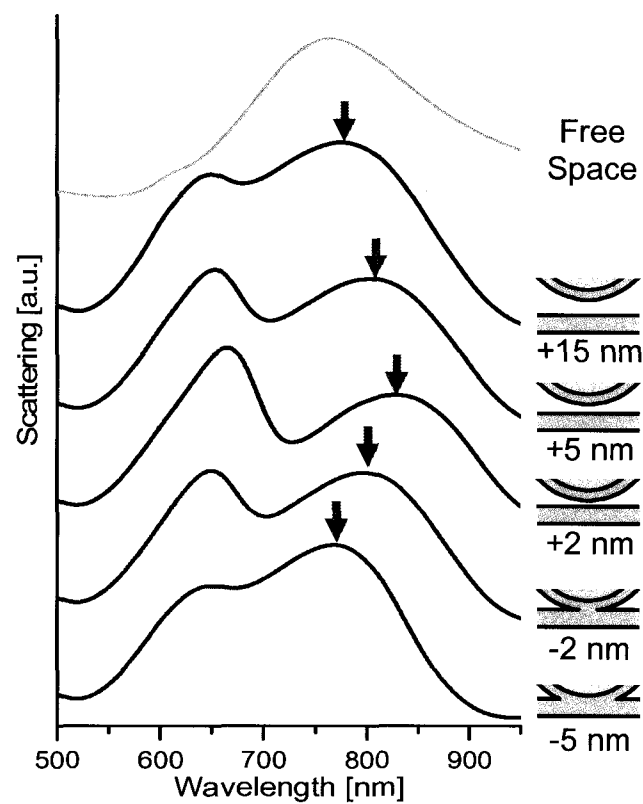


**Figure 9-5** Simulated scattering spectra of an  $[r_1, r_2] = [90, 104]$  nm nanoshell over a 15 nm thick Au film with a varying gap size. The top curve is an  $[r_1, r_2] = [90, 104]$  nm nanoshell in free space.

Far field spectra obtained using this modeling approach are shown in Figure 9-5. The far field spectrum of this structure for a nanoshell slightly above and slightly embedded in the underlying metallic film are indistinguishable. Specifically, as the nanoshell approaches the film, the dipole red-shifts slightly and the quadrupole increases in magnitude relative to a nanoshell in free space. Once in contact, the trends reverse, as the nanoshell makes contact with, and then quite plausibly is pushed even further into the metallic film by radiation pressure. Dark field scattering microspectroscopy performed on several individual nanoshells before and after irradiation (not shown) were also consistent with this observation. Thus, in this case, the linear optical response of this system is not sensitive to changes in the nanoscale geometry, but the nonlinear optical response is

highly sensitive to these changes. This is in contrast to the case of plasmonic dimers, where the linear optical response is highly sensitive to nanoscale geometry.<sup>26, 111, 207, 231</sup>

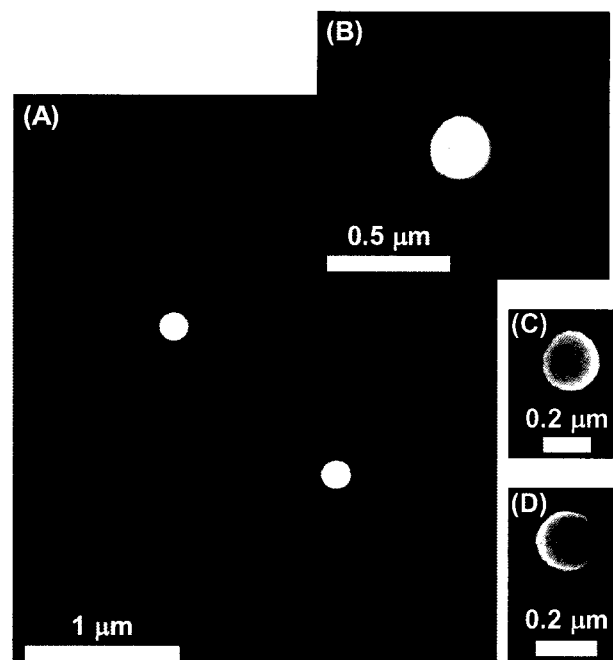


**Figure 9-6** Scanning electron micrographs of the nanoshell / PDDA / Au film nanostructures after irradiation. The specific nanostructure measured in Figure 9-3 is shown in (B) with the brightness adjusted to highlight the effect of irradiation on the film and (C) where the brightness has been adjusted to show the nanoshell clearly. A nanoshell that was not irradiated is shown in (D).

The scanning electron microscopy (SEM) images of the nanogaps reveal dramatic and readily observable structural changes upon irradiation (Figure 9-6). The PDDA layer in the immediate vicinity of each nanoparticle studied appears to have undergone significant modification (Figure 9-6A). The most striking features are the long, extended structures that appear on the substrate, oriented radially outward  $\sim 1\text{-}2\ \mu\text{m}$  away from the irradiated nanogaps. These structures are most likely composed of the dielectric spacer material removed from the nanogap. These structures were observable only around an irradiated nanogap, and were not observed for a similar sample without a dielectric spacer layer, even after irradiation with several times greater intensity. Closer to the nanogap, fringes

consistent with the field pattern expected for a propagating surface plasmon launched from a central source are apparent. Immediately adjacent to each irradiated nanogap, the film appears to have a permanent modification resembling a dipole-like pattern around each nanoshell (Figure 9-6B). Areas of the film irradiated far from a nanogap did not exhibit such structural modifications. These observations provide strong evidence that the changes observed in the vicinity of the nanogap structures arise from photoinduced processes. The actual removal of material from the nanogap and the formation of the extended structures observed further from the particles may depend on additional subsequent mechanisms, possibly including mechanical forces exerted by the particle or rapid local heating on femto- to picosecond time scales. SEM images of representative nanogaps with a thin PDDA spacer layer indicate that the nanoshells themselves were undamaged (Figure 9-6C,D). These observations clearly indicate that the electromagnetic fields are of sufficient intensity to induce significant structural changes in the nanogap region.

To further understand this system, two control cases were investigated experimentally: the absence of a spacer layer and a significantly thicker spacer layer than the samples studied in Figure 9-3. For the case of no dielectric spacer layer, where the nanoshell is initially in contact with the underlying metallic film (Figure 9-7A), the FWM signal decreased monotonically with increasing irradiation time. The dramatic increase in signal characteristically seen when the dielectric spacer layer is present (Figure 9-3) was not observed. It is remarkable that, in this case, where no spacer layer is present, we still see a monotonic decrease in the FWM signal over time. In this case, the slow monotonic signal change is likely occurring as the nanoshell gets pushed into the metallic film,

where the surface area between the nanoparticle and the film is increased. This is consistent with our experimental calculations shown in Figure 9-4C, where following conductive contact, a slow monotonic decrease in the FWM signal is observed. For a thicker spacer comprised of a PDDA / [PSS / PDDA]<sub>2</sub> multilayer approximately 6 nm in thickness, the resulting FWM signal (Figure 9-7B) evolves very similarly to the thinner single PDDA spacer layer (Figure 9-3), but at a much slower rate. Here the signal initially decreases, then starts increasing slowly, jumps at contact (at 23 min), and the slowly decreases. For the single PDDA layer case, the FWM signal increased about 10 minutes after contact.

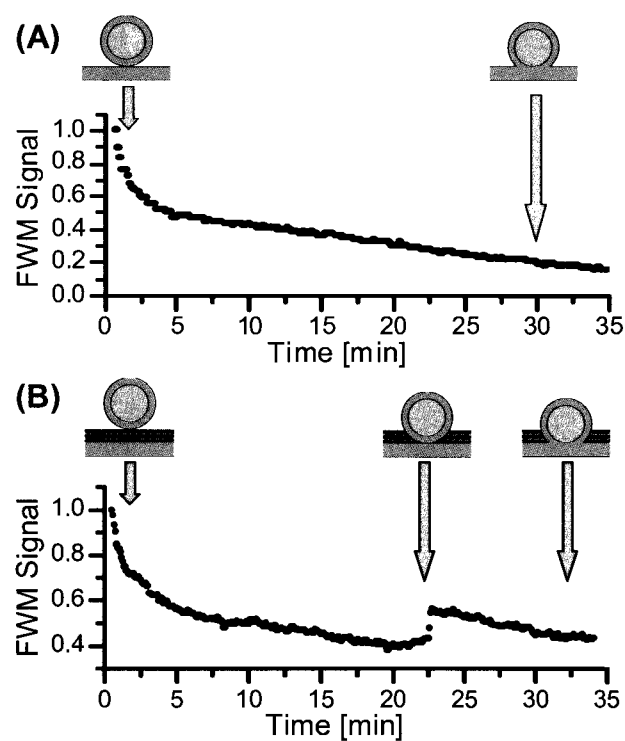


**Figure 9-7** Temporal evolution of the normalized FWM signal at 680 nm, corresponding to the pump at 795 nm mixing with 957 nm light from the continuum, for (A) nanoshells deposited directly on the Au film and (B) nanoshells on top of a PDDA / [PSS / PDDA]<sub>2</sub> multilayer film.

#### 9.4 Conclusions

In this experiment, we have observed that by illuminating a nanogap, consisting of a nanoparticle over a thin metallic film by a polymeric spacer layer, with ultrashort optical pulses, the gap can be slowly and controllably reduced. This process can be self-monitored by the FWM mixing signal from the same illumination beam, which, unlike the linear optical response, is a highly sensitive monitor of the nanoscale geometry. Scanning electron microscopy of the irradiated nanogaps indicates dramatic modifications to the nanoscale polymer layer consistent with photoinduced ablation of the polymer layer within the nanogap, which indicates that the plasmon response of the nanogap is likely to be important in this modification process. These images also indicate that Au nanoshells and the underlying Au film are not modified by this process. In addition to the direct implications for the development of nonlinear plasmonic devices, this observation may lead to a technique to enable the controlled tailoring of the near field properties of individual plasmonic structures. In spirit, this is an optical analog of electromigration-based fabrication techniques in the electrical domain. In electromigration, an applied electric current causes atoms in a small nanostructure to move, while the electrical conductance can be directly measured by monitoring the current driving the electromigration, to controllably fabricate nanoscale gaps.<sup>235, 236</sup> The process we report here parallels this process optically, but with the inverse effect, resulting in a closing, rather than an opening, of a nanoscale junction.

## Chapter 10. Bibliography

1. T. W. Ebbesen, H. J. Lezec, H. F. Ghaemi, T. Thio, and P. A. Wolff, "Extraordinary optical transmission through sub-wavelength hole arrays," *Nature* **391**, 667 - 669 (1998).
2. S. A. Maier, M. L. Brongersma, P. G. Kik, S. Meltzer, A. A.G. Requicha, and H. A. Atwater, "Plasmonics - a route to nanoscale optical devices," *Advanced Materials* **13**(19), 1501-1505 (2001).
3. Stefan A. Maier, Pieter G. Kik, Harry A. Atwater, Sheffer Meltzer, Elad Harel, Bruce E. Koel, and Ari A.G. Requicha, "Local detection of electromagnetic energy transport below the diffraction limit in metal nanoparticle plasmon waveguides," *Nature Materials* **2**(4), 229-232 (2003).
4. W. L. Barnes, "Fluorescence Near Interfaces: The Role of Photonic Mode Density," *J. Mod. Optics* **45**(4), 661-699 (1998).
5. William L. Barnes, Alain Dereux, and Thomas W. Ebbesen, "Surface plasmon subwavelength optics," *Nature* **424**, 824-830 (2003).
6. Palash Bharadwaj, Bradley Deutsch, and Lukas Novotny, "Optical Antennas," *Advances in Optics and Photonics* **1**(3), 438-483 (2009).
7. Matthias Danckwerts and Lukas Novotny, "Optical Frequency Mixing at Coupled Gold Nanoparticles," *Physical Review Letters* **98**(2), 026104 (2007).
8. Martin Moskovits, "Surface-enhanced spectroscopy," *Reviews of Modern Physics* **57**(3), 783-826 (1985).
9. Lukas Novotny and Bert Hecht, *Principles of Nano-Optics* (Cambridge University Press, Cambridge, UK, 2006), pp. 250-299.
10. Surbhi Lal, Stephan Link, and Naomi J. Halas, "Nano-optics from Sensing to Waveguiding," *Nature Photonics* **1**, 641-648 (2007).
11. J. B. Khurgin and G. Sun, "Enhancement of optical properties of nanoscaled objects by metal nanoparticles," *Journal of the Optical Society of America B* **26**(12), B83-B95 (2009).
12. J. P. Marton and B. D. Jordan, "Optical properties of aggregated metal systems: interband transitions," *Physical Review B* **15**(4), 1719-1727 (1977).

13. Hui Wang, Felicia Tam, Nathaniel K. Grady, and Naomi J. Halas, "Cu Nanoshells: Effects of Interband Transitions on the Nanoparticle Plasmon Resonance," *Journal of Physical Chemistry B* **109**(39), 18218-18222 (2005).
14. P. B. Johnson and R. W. Christy, "Optical constants of copper and nickel as a function of temperature," *Physical Review B* **11**(4), 1315-1323 (1975).
15. Arthur L. Aden and Milton Kerker, "Scattering of Electromagnetic Waves from Two Concentric Spheres," *Journal of Applied Physics* **22**(10), 1242-1246 (1951).
16. Richard D. Averitt, Sarah L. Westcott, and Naomi J. Halas, "Linear optical properties of gold nanoshells," *J. Opt. Soc. Am. B* **16**(10), 1824-1832 (1999).
17. S.J. Oldenburg, R.D. Averitt, S.L. Westcott, and N.J. Halas, "Nanoengineering of optical resonances," *Chem. Phys. Lett.* **288**, 234-247 (1998).
18. C. F. Bohren and D. R. Huffman, *Absorption and Scattering of Light by Small Particles* (Wiley, NY, 1983), pp. 136-140.
19. Surbhi Lal, Nathaniel K. Grady, Glenn P. Goodrich, and Naomi J. Halas, "Profiling the Near Field of a Plasmonic Nanoparticle with Raman-Based Molecular Rulers," *Nano Letters* **6**(10), 2338-2343 (2006).
20. Rizia Bardhan, Nathaniel K. Grady, and Naomi J. Halas, "Nanoscale Control of Near-Infrared Fluorescence Enhancement Using Au Nanoshells," *Small* **4**(10), 1716-1722 (2008).
21. Svetlana Neretina, Wei Qian, Erik Dreaden, Mostafa A. El-Sayed, Robert A. Hughes, John S. Preston, and Peter Mascher, "Plasmon Field Effects on the Nonradiative Relaxation of Hot Electrons in an Electronically Quantized System: CdTe-Au Core-Shell Nanowires," *Nano Letters* **8**(8), 2410-2418 (2008).
22. Rizia Bardhan, Nathaniel K. Grady, Joseph R. Cole, Amit Joshi, and Naomi J. Halas, "Fluorescence Enhancement by Au Nanostructures: Nanoshells and Nanorods," *ACS Nano* **3**(3), 744-752 (2009).
23. Sri Priya Sundararajan, Nathaniel K. Grady, Nikolay Mirin, and Naomi J. Halas, "Nanoparticle-Induced Enhancement and Suppression of Photocurrent in a Silicon Photodiode," *Nano Letters* **8**(2), 624-630 (2008).
24. Nathaniel K. Grady, Mark W. Knight, Rizia Bardhan, and Naomi J. Halas, "Optically-Driven Collapse of a Plasmonic Nanogap Self-Monitored by Optical Frequency Mixing," *Nano Letters*, *in press* (2010).
25. Steven J. Oldenburg, Sarah L. Westcott, Richard D. Averitt, and Naomi J. Halas, "Surface enhanced Raman scattering in the near infrared using metal nanoshell substrates," *Journal of Chemical Physics* **111**(10), 4729-4735 (1999).

26. Bruce E. Brinson, J. Britt Lassiter, Carly S. Levin, Rizia Bardhan, Nikolay Mirin, and Naomi J. Halas, "Nanoshells Made Easy: Improving Au Layer Growth on Nanoparticle Surfaces," *Langmuir* **24**(24), 14166–14171 (2008).
27. Carly S. Levin, Cristina Hofmann, Tamer A. Ali, Anna T. Kelly, Emilia Morosan, Peter Nordlander, Kenton H. Whitmire, and Naomi J. Halas, "Magnetic–Plasmonic Core–Shell Nanoparticles," *ACS Nano* **3**(6), 1379-1388 (2009).
28. Uwe Kreibig and Michael Vollmer, *Optical Properties of Metal Clusters*, Springer Series in Materials Science (Springer-Verlag, Berlin, 1995), Vol. 25.
29. Dipankar Sarkar, "Vector Basis Function Solution of Maxwell's Equations," (Rice University, Houston, 2005).
30. Chad E. Talley, Joseph B. Jackson, Chris Oubre, Nathaniel K. Grady, Christopher W. Hollars, Stephen M. Lane, Thomas R. Huser, Peter Nordlander, and Naomi J. Halas, "Surface-Enhanced Raman Scattering from Individual Au Nanoparticles and Nanoparticle Dimer Substrates," *Nano Letters* **5**(8), 1569-1574 (2005).
31. J. W. Gibson and B. R. Johnson, "Density-matrix calculation of surface-enhanced Raman scattering for p-mercaptoaniline on silver nanoshells," *Journal of Chemical Physics* **124**(6), 0647011 - 06470112 (2006).
32. J. B. Pendry, "Negative Refraction Makes a Perfect Lens," *Physical Review Letters* **85**(18), 3966-3969 (2000).
33. Shuming Nie and Steven R. Emory, "Probing Single Molecules and Single Nanoparticles by Surface-Enhanced Raman Scattering," *Science* **275**(5303), 1102-1106 (1997).
34. Katrin Kneipp, Yang Wang, Harald Kneipp, Lev T. Perelman, Irving Itzkan, Ramachandra R. Dasari, and Michael S. Feld, "Single Molecule Detection Using Surface-Enhanced Raman Scattering (SERS)," *Physical Review Letters* **78**(9), 1667-1670 (1997).
35. J. B. Jackson and N. J. Halas, "Surface-enhanced Raman scattering on tunable plasmonic nanoparticle substrates," *Proc. Natl. Acad. Sci. USA* **101** (52), 17930-17935 (2004).
36. Y. Xia and N. J. Halas, eds., *Synthesis and Plasmonic Properties of Nanostructures*, MRS Bulletin (Materials Research Society, Warrendale, PA, 2005), Vol. 30(5).
37. K. Lance Kelly, Eduardo Coronado, Lin Lin Zhao, and George C. Schatz, "The Optical Properties of Metal Nanoparticles: The Influence of Size, Shape, and Dielectric Environment," *Journal of Physical Chemistry B* **107**(3), 668-677 (2003).

38. Chris Oubre and Peter Nordlander, "Optical Properties of Metallo-dielectric Nanostructures Calculated Using the Finite Difference Time Domain Method," *J. Phys. Chem. B* **108**(46), 17740-17747 (2004).
39. E. Prodan, C. Radloff, N. J. Halas, and P. Nordlander, "A Hybridization Model for the Plasmon Response of Complex Nanostructures," *Science* **302**, 419-422 (2003).
40. S. R. Sershen, S. L. Westcott, N. J. Halas, and J. L. West, "Temperature-sensitive polymer-nanoshell composites for photothermally modulated drug delivery," *Journal of Biomedical Materials Research Part A* **51**(3), 293-298 (2000).
41. Christopher Loo, Amanda Lowery, Naomi Halas, Jennifer West, and Rebekah Drezek, "Immunotargeted Nanoshells for Integrated Cancer Imaging and Therapy," *Nano Letters* **5**(4), 709-711 (2005).
42. Christopher Loo, Alex Lin, Leon Hirsch, Min-Ho Lee, Jennifer Barton, Naomi Halas, Jennifer West, and Rebekah Drezek, "Nanoshell-Enabled Photonics-Based Imaging and Therapy of Cancer," *Technology in Cancer Research & Treatment* **3**(1), 33-40 (2004).
43. L. R. Hirsch, R. J. Stafford, J. A. Bankson, S. R. Sershen, B. Rivera, R. E. Price, J. D. Hazle, N. J. Halas, and J. L. West, "Nanoshell-mediated near-infrared thermal therapy of tumors under magnetic resonance guidance," *Proc. Natl. Acad. Sci. USA* **100**(23), 13549-13554 (2003).
44. Corey Radloff and Naomi J. Halas, "Plasmonic Properties of Concentric Nanoshells," *Nano Letters* **4**(7), 1323-1327 (2004).
45. A. E. Neeves and M. H. Birnboim, "Composite structures for the enhancement of nonlinear-optical susceptibility," *Journal of the Optical Society of America B* **6**(4), 787-796 (1989).
46. Colleen L. Nehl, Nathaniel K. Grady, Glenn P. Goodrich, Felicia Tam, Naomi J. Halas, and Jason H. Hafner, "Scattering Spectra of Single Gold Nanoshells," *Nano Letters* **4**(12), 2355-2359 (2004).
47. N. K. Grady, N. J. Halas, and P. Nordlander, "Influence of dielectric function properties on the optical response of plasmon resonant metallic nanoparticles," *Chemical Physics Letters* **399**(1-3), 167-171 (2004).
48. CRC Handbook of Chemistry and Physics, D. R. Lide, Eds., CRC press, Boca Raton, and FL, (2000).
49. J. Wiesner and A. Wokaun, "Anisometric gold colloids. Preparation, characterization, and optical properties " *Chemical Physics Letters* **157**(6), 569-575 (1989).

50. P. B. Johnson and R. W. Christy, "Optical Constants of the Noble Metals," *Physical Review B* **6**(12), 4370-4379 (1972).
51. A. Pinchuk, U. Kreibig, and A. Hilger, "Optical Properties of metallic nanoparticles: influence of interface effects and interband transitions," *Surface Science* **557**(1-3), 269-280 (2004).
52. J. B. Jackson and N. J. Halas, "Silver Nanoshells: Variations in Morphologies and Optical Properties," *J. Phys. Chem. B* **105**, 2743-2746 (2001).
53. S.J. Oldenburg, J. B. Jackson, S.L. Westcott, and N. J. Halas, "Infrared extinction properties of gold nanoshells," *Appl. Phys. Lett.* **111**, 2897-2899 (1999).
54. S. J. Oldenburg, G. D. Hale, J. B. Jackson, and N. J. Halas, "Light scattering from dipole and quadrupole nanoshell antennas," *Applied Physics Letters* **75**(8), 1063-1065 (1999).
55. S.L. Westcott, J.B. Jackson, C. Radloff, and N.J. Halas, "Relative contributions to plasmon lineshape of metal nanoshells," *Physical Review B* **66**(15), Article No. 155431 (2002).
56. Christina Graf and Alfons van Blaaderen, "Metallo-dielectric Colloidal Core-Shell Particles for Photonic Applications," *Langmuir* **18**, 524-534 (2002).
57. Yong Taik Lim, O Ok Park, and Hee-Tae Jung, "Gold nanolayer-encapsulated silica particles synthesized by surface seeding and shell growing method: near infrared responsive materials," *Journal of Colloid and Interface Science* **263**(2), 449-453 (2003).
58. Weili Shi, Y. Sahoo, Mark T. Swihart, and P. N. Prasad, "Gold Nanoshells on Polystyrene Cores for Control of Surface Plasmon Resonance," *Langmuir* **21**(4), 1610-1617 (2005).
59. Zhong-jie Jiang and Chun-yan Liu, "Seed-Mediated Growth Technique for the Preparation of a Silver Nanoshell on a Silica Sphere," *Journal of Physical Chemistry B* **107**(45), 12411-12415 (2003).
60. Lehui Lu, Hongjie Zhang, Guoying Sun, Shiquan Xi, and Haishui Wang, "Aggregation-Based Fabrication and Assembly of Roughened Composite Metallic Nanoshells: Application in Surface-Enhanced Raman Scattering," *Langmuir* **19**(22), 9490-9493 (2003).
61. J. B. Liu, W. Dong, P. Zhan, S. Z. Wang, J. H. Zhang, and Z. L. Wang, "Synthesis of Bimetallic Nanoshells by an Improved Electroless Plating Method," *Langmuir* **21**(5), 1683-1686 (2005).

62. Yugang Sun and Younan Xia, "Increased Sensitivity of Surface Plasmon Resonance of Gold Nanoshells Compared to That of Gold Solid Colloids in Response to Environmental Changes," *Anal. Chem.* **74**(20), 5297-5305 (2002).
63. Yugang Sun and Younan Xia, "Alloying and Dealloying Processes Involved in the Preparation of Metal Nanoshells through a Galvanic Replacement Reaction," *Nano Letters* **3**(11), 1569-1572 (2003).
64. Han-Pu Liang, Li-Jun Wan, Chun-Li Bai, and Li Jiang, "Gold Hollow Nanospheres: Tunable Surface Plasmon Resonance Controlled by Interior-Cavity Sizes," *Journal of Physical Chemistry B* **109**(16), 7795-7800 (2005).
65. Ke Zhao, Hongxing Xu, and Baohua Gu, "One-Dimensional Arrays of Nanoshell Dimers for Single Molecule Spectroscopy via Surface-Enhanced Raman Scattering," *J. Chem. Phys.* **125**, 081102 (2006).
66. Surbhi Lal, Susan E. Clare, and Naomi J. Halas, "Nanoshell-Enabled Photothermal Cancer Therapy: Impending Clinical Impact," *Acc. Chem. Res.* **41**(12)(2008).
67. R. R. Chance, A. Prock, and R. Silbey, "Lifetime of an Excited Molecule near a Metal Mirror - Energy-Transfer in  $\text{Eu}^{3+}$ -Silver System," *Journal of Chemical Physics* **60**(5), 2184-2185 (1974).
68. Daniel W. Brandl and Peter Nordlander, "Plasmon modes of curvilinear metallic core/shell particles," *Journal of Chemical Physics* **126**(14), 144708 (2007).
69. Rizia Bardhan, Shaunak Mukherjee, Nikolay Mirin, Stephen D. Levit, Peter Nordlander, and Naomi J. Halas, "Nanosphere-in-a-Nanoshell: A Simple Nanomatryushka," *J Phys. Chem. C* **in press**, doi: 10.1021/jp9095387 (2009).
70. A. Jolk and C. F. Klingshirn, "Linear and Nonlinear Excitonic Absorption and Photoluminescence Spectra in  $\text{Cu}_2\text{O}$ : Line Shape Analysis and Exciton Drift," *Phys. Stat. Sol. B* **206**, 841-850 (1998).
71. H Matsumoto, K Saito, M Hasuo, S Kono, and N Nagasawa, "Revived Interest on Yellow-exciton Series in  $\text{Cu}_2\text{O}$ : An Experimental Aspect," *Solid State Commun.* **97**(2), 125-129 (1996).
72. N. Naka and N. Nagasawa, "Experimental Study on Two-photon Oscillator Strength of Hydrogenic Yellow Excitons in  $\text{Cu}_2\text{O}$ ," *Solid State Commun.* **116**, 417-419 (2000).
73. K. Karpinska, M. Mostovoy, M. A. van der Vegte, A. Revcolevschi, and P. H. M. van Loosdrecht, "Decay and Coherence of Two-photon Excited Yellow Orthoexcitons in  $\text{Cu}_2\text{O}$ ," *Phys. Rev. B* **72**, 155201 (2005).

74. K. Karpinska, P.H.M. van Loosdrecht, I.P. Handayani, and A. Revcolevschi, "Para-excitons in  $\text{Cu}_2\text{O}$  - A New Approach," *J. Lumin.* **112**, 17-20 (2005).
75. D. Snoke, "Spontaneous Bose Coherence of Excitons and Polaritons," *Science* **298**, 1368-1372 (2002).
76. G. Baldassarri Hoger von Hogersthal, G. Dasbach, D. Frohlich, M. Kulka, H. Stolz, and M. Bayer, "Dynamic Band Gap Shifts and Magneto-Absorption of  $\text{Cu}_2\text{O}$ ," *J. Lumin.* **112**, 25-29 (2005).
77. D. Fishman, C. Faugeras, M. Potemski, A. Revcolevschi, and P. H. M. van Loosdrecht, "Magneto-optical Readout of Dark Exciton Distribution in Cuprous Oxide," *Phys. Rev. B* **80**, 045208 (2009).
78. A. R. H. F. Ettema and J. Versluis, "Dipole-allowed Generation of the Yellow-series Excitons in  $\text{Cu}_2\text{O}$  Due to an Applied Electric Field," *Phys. Rev. B* **68**, 235101 (2003).
79. D. Fröhlich, A. Nöthe, and K. Reimann, "Observation of the Resonant Optical Stark Effect in a Semiconductor.," *Phys. Rev. Lett.* **55**(12), 1335-1337 (1985).
80. Shahin E. Mani, Joon I. Jang, and John B. Ketterson, "Large Third-order Susceptibility and Third-harmonic Generation in Centrosymmetric  $\text{Cu}_2\text{O}$  Crystal," *Optics Lett.* **34**(18), 2817-2819 (2009).
81. Nche T. Fofang, Tae-Ho Park, Oara Neumann, Nikolay A. Mirin, Peter Nordlander, and Naomi J. Halas, "Plexcitonic Nanoparticles: Plasmon-Exciton Coupling in Nanoshell-J-Aggregate Complexes," *Nano Lett.* **8**(10), 3481-3487 (2008).
82. L. Gou and C. J. Murphy, "Controlling the Size of  $\text{Cu}_2\text{O}$  Nanocubes From 200 to 25 nm," *J. Mater. Chem.* **14**, 735 - 738 (2004).
83. C. Ribeiro, E. J. H. Lee, E. Longo, and E.R. Leite, "Oriented Attachment Mechanism in Anisotropic Nanocrystals: A "Polymerization" Approach " *ChemPhysChem* **7**, 664 - 670 (2006).
84. C-H. Kuo, C-H. Chen, and M. H. Huang, "Seed-Mediated Synthesis of Monodispersed  $\text{Cu}_2\text{O}$  Nanocubes with Five Different Size Ranges from 40 to 420 nm," *Adv. Funct. Mater.* **17**, 3773-3780 (2007).
85. Y. N. Barabanenkov and M. Yu. Barabanenkov, "Mie Resonances and Bragg-like Multiple Scattering in Opacity of Two-Dimensional Photonic Crystals," *J. Opt. Soc. Am. A* **23**, 581-585 (2006).
86. W. Lynch and W. R. Hunter, *Handbook of Optical Constants of Solids* (Academic, Orlando, FL, 1985), Vol. 2, pp. 333-341.

87. Daniel G. Duff, Alfons Baiker, and Peter P. Edwards, "A New Hydrosol of Gold Clusters. 1. Formation and Particle Size Variation," *Langmuir* **9**(9), 2301-2309 (1993).
88. J. Zhang, J. Liu, Q. Peng, X. Wang, and Y. Li, "Nearly Monodisperse Cu<sub>2</sub>O and CuO Nanospheres: Preparation and Applications for Sensitive Gas Sensors," *Chem. Mater.* **18**, 867-871 (2006).
89. Felicia Tam, Allen L. Chen, Janardan Kundu, Hui Wang, and Naomi J. Halas, "Mesoscopic nanoshells: Geometry-dependent plasmon resonances beyond the quasistatic limit," *Journal of Chemical Physics* **127**(20), 204703 (2007).
90. E. Prodan and P. Nordlander, "Plasmon hybridization in spherical nanoparticles," *Journal of Chemical Physics* **120**(11), 5444-5454 (2004).
91. K. Kneipp, Y. Wang, H. Kneipp, I. Itzkan, R. R. Dassari, and M. S. Feld, "Population pumping of excited vibrational states by spontaneous surface-enhanced Raman scattering," *Phys. Rev. Lett.* **76**, 2444-2447 (1996).
92. R. C. Maher, L. F. Cohen, P. Etchegoin, H. J. N. Hartigan, R. J. C. Brown, and M. J. T. Milton, "Stokes/anti-Stokes anomalies under surface enhanced Raman scattering conditions," *J. Chem. Phys.* **120**(24), 11746 (2004).
93. A. M. Michaels, J. Jiang, and L. Brus, "Ag Nanocrystal Junctions as the Site for Surface-Enhanced Raman Scattering of Single Rhodamine 6GMolecules," *J. Phys. Chem. B* **104**, 11965-11971 (2000).
94. Hongxing Xu, Javier Aizpurua, Mikael Käll, and Peter Apell, "Electromagnetic contributions to single-molecule sensitivity in surface-enhanced Raman scattering," *Phys. Rev. E* **62**(3), 4318-4324 (2000).
95. Felicia Tam, Cristin Moran, and Naomi Halas, "Geometrical Parameters Controlling Sensitivity of Nanoshell Plasmon Resonances to Changes in Dielectric Environment," *Journal of Physical Chemistry B* **108**(45), 17290-17294 (2004).
96. Amanda J. Haes and Richard P. Van Duyne, "A Nanoscale Optical Biosensor: Sensitivity and Selectivity of an Approach Based on the Localized Surface Plasmon Resonance Spectroscopy of Triangular Silver Nanoparticles," *J. Am. Chem. Soc.* **124**, 10596-10604 (2002).
97. Werayut Srituravanich, Nicholas Fang, Cheng Sun, Qi Luo, and Xiang Zhang, "Plasmonic Nanolithography," *Nano Lett.* **4**(6), 1085-1088 (2004).
98. Arvind Sundaramurthy, P. James Schuck, Nicholas R. Conley, David P. Fromm, Gordon S. Kino, and W. E. Moerner, "Toward Nanometer-Scale Optical Photolithography: Utilizing the Near-Field of Bowtie Optical Nanoantennas," *Nano Lett.* **6**(3), 355-360 (2006).

99. P. O'Neal, L. R. Hirsch, N. J. Halas, J. Donald Payne, and J. L. West, "Photothermal Tumor Ablation in mice using near infrared absorbing nanoshells," *Can. Lett.* **209**, 171-176 (2004).
100. C. S. Yun, A. Javier, T. Jennings, M. Fisher, S. Hira, S. Peterson, B. Hopkins, N. O. Reich, and G. F. Strouse, "Nanometal Surface Energy Transfer in Optical Rulers, Breaking the FRET Barrier," *J. Am. Chem. Soc.* **127**, 3115-3119 (2005).
101. E. Dulkeith, M. Ringler, T. A. Klar, J. Feldmann, A. Muñoz Javier, and W. J. Parak, "Gold Nanoparticles Quench Fluorescence by Phase Induced Radiative Rate Suppression," *Nano Lett.* **5** (4), 585-589 (2005).
102. Joanna Malicka, Ignacy Gryczynski, Zygmunt Gryczynski, and Joseph R. Lakowicz, "Effects of fluorophore-to-silver distance on the emission of cyanine dye-labeled oligonucleotides," *Anal. Biochem.* **315** 57-66 (2003).
103. K. Sokolov, G. Chumanov, and T. M. Cotton, "Enhancement of molecular fluorescence near the surface of colloidal metal films," *Anal. Chem.* **70**, 3898-3905 (1998).
104. H. Knobloch, H. Brunner, A. Leitner, F. Aussenegg, and W. Knoll, "Probing the evanescent field of propagating plasmon surface polaritons by fluorescence and Raman spectroscopies," *J. Chem. Phys.* **98**(12), 10093-10095 (1993).
105. B. J. Kennedy, S. Spaeth, M. Dickey, and K. T. Carron, "Determination of the Distance Dependence and Experimental Effects for Modified SERS Substrates Based on Self-Assembled Monolayers Formed Using Alkanethiols," *J. Phys. Chem. B* **103**, 3640-3646 (1999).
106. Achim Hartschuh, Erik J. Sanchez, X. Sunney Xie, and Lukas Novotny, "High-Resolution Near-Field Raman Microscopy of Single-Walled Carbon Nanotubes," *Phys. Rev. Lett.* **90**(9), 95503-95506 (2003).
107. Jr .David D. Evanoff, White Ryan L., and Chumanov George, "Measuring the Distance Dependence of the Local Electromagnetic Field from Silver Nanoparticles," *J. Phys. Chem. B* **108**, 1522-1524 (2004).
108. Carsten Sonnichsen, Bjorn M Reinhard, Jan Liphardt, and A. Paul Alivisatos, "A molecular ruler based on plasmon coupling of single gold and silver nanoparticles " *Nature Biotech.* **23**(6), 741-745 (2005).
109. J. B. Jackson, S. L. Westcott, L. R. Hirsch, J. L. West, and N. J. Halas, "Controlling the surface enhanced Raman effect via the nanoshell geometry," *Appl. Phys. Lett.* **82**(2)(2003).
110. Hui Wang, Carly S. Levin, and Naomi J. Halas, "Nanosphere Arrays with Controlled Sub-10-nm Gaps as Surface-Enhanced Raman Spectroscopy Substrates," *J. Am. Chem. Soc.* **127**, 14992-14993 (2005).

111. P. Nordlander, C. Oubre, E. Prodan, K. Li, and M. I. Stockman, "Plasmon Hybridization in Nanoparticle Dimers," *Nano Letters* **4**(5), 899-903 (2004).
112. C. Oubre and P. Nordlander, "Finite-difference Time-domain Studies of the Optical Properties of Nanoshell Dimers," *Journal of Physical Chemistry B* **109**(20), 10042-10051 (2005).
113. Hui Wang, Daniel W. Brandl, Fei Le, Peter Nordlander, and Naomi J. Halas, "Nanorice: A Hybrid Plasmonic Nanostructure," *Nano Letters* **6**(4), 827-832 (2006).
114. Hui Wang, Yanpeng Wu, Britt Lassiter, Colleen L. Nehl, Jason H. Hafner, Peter Nordlander, and Naomi J. Halas, "Symmetry breaking in individual plasmonic nanoparticles," *Proc. Natl. Acad. Sci. USA* **103**(29), 10856-10860 (2006).
115. Wolfgang J. Parak, Teresa Pellegrino, Christine M. Micheel, Daniele Gerion, Shara C. Williams, and A. Paul Alivisatos, "Conformation of Oligonucleotides Attached to Gold Nanocrystals Probed by Gel Electrophoresis," *Nano Lett.* **3**(1), 33-36 (2003).
116. Rong-Ying Zhang, Dai-Wen Pang, Zhi-Ling Zhang, Jia-Wei Yan, Jian-Lin Yao, Zhong-Qun Tian, Bing-Wei Mao, and Shi-Gang Sun, "Investigation of Ordered ds-DNA Monolayers on Gold Electrode," *J. Phys. Chem. B* **106**, 11233-11239 (2002).
117. Rongsheng Sheng, Fan Ni, and Therese M. Cotton, "Determination of Purine Bases by Reversed-Phase High-Performance Liquid Chromatography Using Real-Time Surface-Enhanced Raman Spectroscopy," *Anal. Chem.* **63**, 437-442 (1991).
118. Joseph R. Perno, Christine A. Grygon, and Thomas G. Spiro, "Ultraviolet Raman Excitation Profiles for the Nucleotides and for the Nucleic Acid Duplexes Poly(rA)-Poly(rU) and Poly(dG-dC)," *J. Phys. Chem. B* **93**, 5612-5678 (1989).
119. J. S. Suh and M. Moskovits, "Surface-Enhanced Raman Spectroscopy of Amino Acids and Nucleotide Bases Adsorbed on Silver," *J. Am. Chem. Soc.* **108**, 471-4718 (1986).
120. Lili Wang, A. Roitberg, C. Meuse, and A.K. Gaigalas, "Raman and FTIR spectroscopies of fluorescein in solutions," *Spectrochimica Acta Part A* **57**, 1781-1791 (2001).
121. [www.idtdna.com](http://www.idtdna.com), retrieved 2006.
122. Sheila R. Nicewarner-Peña, Surabhi Raina, Glenn P. Goodrich, Nina V. Fedoroff, and Christine D. Keating, "Hybridization and Enzymatic Extension of Au Nanoparticle-Bound Oligonucleotides," *J. Am. Chem. Soc.* **124**, 7314-7323 (2002).

123. Wolfgang K. H. Panofsky and Melba Philips, *Classical Electricity and Magnetism: Second Edition* (Dover Publications, Mineola, NY, 2005).
124. Jon A. Dieringer, Adam D. McFarland, Nilam C. Shah, Douglas A. Stuart, Alyson V. Whitney, Chanda R. Yonzon, Matthew A. Young, Xiaoyu Zhang, and Richard P. Van Duyne, "Surface Enhanced Raman Spectroscopy: new materials, concepts, characterization tools, and applications," *Faraday Discussions* **132**, 9-26 (2006).
125. R. R. Chance, A. Prock, and R. Silbey, "Lifetime of an emitting molecule near a partially reflecting surface," *Journal of Chemical Physics* **60**(7), 2744-2748 (1974).
126. K. H. Drexhage, "Influence of a Dielectric Interface on Fluorescence Decay Time," *Journal of Luminescence* **1-2**, 693-701 (1970).
127. Joseph R. Lakowicz, "Radiative decay engineering 5: metal-enhanced fluorescence and plasmon emission," *Analytical Biochemistry* **337**(2), 171-194 (2005).
128. Kristen E. Adams, Shi Ke, Sunkuk Kwon, Feng Liang, Zhen Fan, and Yang Lu, "Comparison of visible and near-infrared wavelength-excitable fluorescent dyes for molecular imaging of cancer," *Journal of Biomedical Optics* **12**(2), 024017 (2007).
129. Jessica P. Houston, Shi Ke, Wei Wang, Chun Li, and Eva M. Sevick-Muraca, "Quality analysis of in vivo near-infrared fluorescence and conventional gamma images acquired using a dual-labeled tumor-targeting probe," *Journal of Biomedical Optics* **10**(5), 054010 (2005).
130. Yuri Avlasevich and Klaus Müllen, "An Efficient Synthesis of Quaterrylenedicarboximide NIR Dyes," *Journal of Organic Chemistry* **72**(26), 10243-10246 (2007).
131. Kai Licha, Björn Riefke, Vasilis Ntziachristos, Andreas Becker, Britton Chance, and Wolfhard Semmler, "Hydrophilic Cyanine Dyes as Contrast Agents for Near-infrared Tumor Imaging: Synthesis, Photophysical Properties and Spectroscopic In vivo Characterization," *Photochemistry and Photobiology* **72**(3), 392-398 (2000).
132. T. Tsubono, S. Todo, N. Jabbour, A. Mizoe, V. Warty, A. J. Demetris, and T. E. Starzl, "Indocyanine green elimination test in orthotopic liver recipients," *Hepatology* **24**(5), 1165-1171 (1996).
133. Samir G. Sakka, Konrad Reinhart, Karl Wegscheider, and Andreas Meier-Hellmann, "Comparison of Cardiac Output and Circulatory Blood Volumes by Transpulmonary Thermo-Dye Dilution and Transcutaneous Indocyanine Green Measurement in Critically Ill Patients," *Chest* **121**(2), 559-565 (2002).

134. H Ishihara, H Okawa, T Iwikawa, N Umegaki, T Tsubo, and A. Matsuki, "Does indocyanine green accurately measure plasma volume early after cardiac surgery?," *Anesthesia and Analgesia* **94**(4), 781-786 (2002).
135. Pieter R. van den Biesen, Frans H. Jongasma, Geert Jan Tangelder, and Dick W. Slaaf, "Yield of fluorescence from indocyanine green in plasma and flowing blood," *Annals of Biomedical Engineering* **23**(4), 475-481 (1995).
136. Andrew A. Chang, Lawrence S. Morse, James T. Handa, Ronald B. Morales, Richard Tucker, Leonard Hjelmeland, and Lawrence A. Yannuzzi, "Histologic localization of indocyanine green dye in aging primate and human ocular tissues with clinical angiographic correlation," *Ophthalmology* **105**(6), 1060-1068 (1998).
137. R. Tadayoni, M. Paques, J.F. Girmens, P. Massin, and A. Gaudric, "Persistence of fundus fluorescence after use of indocyanine green for macular surgery " *Ophthalmology* **110**(3), 604-608 (2003).
138. V. Ntziachristos, A. G. Yodh, M. Schnall, and B. Chance, "Concurrent MRI and diffuse optical tomography of breast after indocyanine green enhancement," *Proc. Natl. Acad. Sci.* **97**(6), 2767-2772 (2000).
139. R. C. Benson and H. A. Kues, "Fluorescence Properties of Indocyanine Green as Related to Angiography," *Phys. Med. Biol.* **23**(1), 159-163 (1978).
140. Iga Kulakovich, Natalya Strekal, Alexandr Yaroshevich, Sergey Maskevich, Sergey Gaponenko, Igor Nabiev, Ulrike Woggon, and Mikhail Artemyev, "Enhanced Luminescence of CdSe Quantum Dots on Gold Colloids," *Nano Letters* **2**(12), 1449-1452 (2002).
141. J. S. Biteen, N. S. Lewis, H. Mertens, A. Polman, and H. A. Atwater, "Spectral tuning of plasmon-enhanced silicon quantum dot luminescence," *Appl. Phys. Lett.* **88**(131109)(2006).
142. Carly S. Levin, Benjamin G. Janesko, Rizia Bardhan, Gustavo E. Scuseria, Jeffrey D. Hartgerink, and Naomi J. Halas, "Chain-Length-Dependent Vibrational Resonances in Alkanethiol Self-Assembled Monolayers Observed on Plasmonic Nanoparticle Substrates," *Nano Letters* **6**(11), 2617 - 2621 (2006).
143. J. R. Lakowicz, "Radiative Decay Engineering: Biophysical and Biomedical Applications," *Anal. Biochem.* **298**, 1 - 24 (2001).
144. J. R. Lakowicz, Y. Shen, S. D'Auria, J. Malicka, J. Fang, Z. Gryczynski, and I. Gryczynski, "Radiative Decay Engineering - Effects of Silver Island Films on Fluorescence Intensity, Lifetimes, and Resonance Energy Transfer," *Anal. Biochem.* **301**, 261 - 277 (2002).

145. A. C. Pease, D. Solas, E. J. Sullivan, M. T. Cronin, C. P. Holmes, and S. P. A. Fodor, "Light-generated oligonucleotide arrays for rapid DNA sequence analysis," *Proc. Natl. Acad. Sci.* **91**(11), 5022 - 5026 (1994).
146. S. Weiss, "Fluorescence Spectroscopy of Single Biomolecules," *Science* **283**(5408), 1676 - 1683 (1999).
147. A.W.A. Weinberger, B. Kirchhof, B.E. Mazinani, and N.F. Schrage, "Persistent indocyanine green (ICG) fluorescence 6 weeks after intraocular ICG administration for macular hole surgery," *Graefe's Archive for Clinical and Experimental Ophthalmology* **239**(5), 388 - 390 (2001).
148. K. H. Drexhage, "Analysis of Light Fields with Monomolecular Dye Layers," *Journal of the Optical Society of America* **60**(11), 1541-& (1970).
149. K. Ray, R. Badugu, and J. R. Lakowicz, "Distance-Dependent Metal-Enhanced Fluorescence from Langmuir-Blodgett Monolayers of Alkyl-NBD Derivatives on Silver Island Films," *Langmuir* **22**(20), 8374-8378 (2006).
150. D. A. Weitz, S. Garoff, C. D. Hanson, T. J. Gramila, and Gersten J. I., "Fluorescent Lifetimes And Yields Of Molecules Adsorbed On Silver Island Films," *J Lumin.* **24/25**, 83-86 ( 1981 ).
151. Pascal Anger, Palash Bharadwaj, and Lukas Novotny, "Enhancement and Quenching of Single-Molecule Fluorescence," *Physical Review Letters* **96**(11), 113002 (2006).
152. E. Dulkeith, A. C. Morteani, T. Niedereichholz, T. A. Klar, J. Feldmann, S. A. Levi, F. C. J. M. van Veggel, D. N. Reinhoudt, M. Möller, and D. I. Gittins, "Fluorescence Quenching of Dye Molecules near Gold Nanoparticles: Radiative and Nonradiative Effects," *Physical Review Letters* **89**(20), 203002 (2002).
153. Andrew Burns, Hooisweng Ow, and Ulrich Wiesner, "Fluorescent core-shell silica nanoparticles: towards Lab on a Particle architectures for nanobiotechnology," *Chemical Society Reviews* **35**, 1028-1042 (2006).
154. Werner Stöber, Arthur Fink, and Ernst Bohn, "Controlled Growth of Monodisperse Silica Spheres in the Micron Size Range," *J. Colloid Interface Sci.* **26**(1), 62-69 (1968).
155. Elizabeth M. McCorquodale and Christa L. Colyer, "Indocyanine green as a noncovalent, pseudofluorogenic label for protein determination by capillary electrophoresis," *Electrophoresis* **22**(12), 2403-2408 (2001).
156. E. Prodan, Allen Lee, and P. Nordlander, "The effect of a dielectric core and embedding medium on the polarizability of metallic nanoshells," *Chemical Physics Letters* **360**(3-4), 325-332 (2002).

157. Steven A. Soper and Quincy L. Mattingly, "Steady-State and Picosecond Laser Fluorescence Studies of Nonradiative Pathways in Tricarbocyanine Dyes: Implications to the Design of Near-IR Fluorochromes with High Fluorescence Efficiencies," *Journal of the American Chemical Society* **116**(9), 3744-3752 (1994).
158. Elizabeth M. C. Hillman and Anna Moore, "All-Optical Anatomical Co-registration for Molecular Imaging of Small Animals Using Dynamic Contrast," *Nature Photonics* **1**(9), 526-530 (2007).
159. Joy L. Kovar, Melanie A. Simpson, Amy Schutz-Geschwender, and D. Michael Olive, "A Systematic Approach to the Development of Fluorescent Contrast Agents for Optical Imaging of Mouse Cancer Models," *Analytical Biochemistry* **367**(1), 1-12 (2007).
160. R. Weissleder, "A Clearer Vision For in vivo Imaging," *Nature Biotech.* **19**, 316-317 (2001).
161. K. H. Drexhage, "Monomolecular Layers and Light," *Scientific American* **222**(3), 108-119 (1970).
162. Jeffrey N. Anker, W. Paige Hall, Olga Lyandres, Nilam C. Shah, Jing Zhao, and Richard P. Van Duyne, "Biosensing With Plasmonic Nanosensors," *Nature Materials* **7**(6), 442-453 (2008).
163. Hongwei Liao, Colleen L Nehl, and Jason H Hafner, "Biomedical applications of plasmon resonant metal nanoparticles," *Nanomedicine* **1**(2), 201-208 (2006).
164. Hui Wang, Daniel W. Brandl, Peter Nordlander, and Naomi J. Halas, "Plasmonic Nanostructures: Artificial Molecules," *Accounts of Chemical Research* **40**(1), 53-62 (2007).
165. Jae-Hyun Lee, Young-wook Jun, Soo-In Yeon, Jeon-Soo Shin, and Jinwoo Cheon, "Dual-Mode Nanoparticle Probes for High-Performance Magnetic Resonance and Fluorescence Imaging of Neuroblastoma," *Angewandte Chemie* **45**(48), 8160-8162 (2006).
166. M. C. Daniel and D. Astruc, "Gold Nanoparticles: Assembly, Supramolecular Chemistry, Quantum-size-related Properties, and Applications Toward Biology, Catalysis, and Nanotechnology," *Chem. Rev.* **104**(1), 293-346 (2004).
167. Hui Wang, Glenn P. Goodrich, Felicia Tam, Chris Oubre, Peter Nordlander, and Naomi J. Halas, "Controlled Texturing Modifies the Surface Topography and Plasmonic Properties of Au Nanoshells," *Journal of Physical Chemistry B* **109**(22), 11083-11087 (2005).

168. Babak Nikoobakht and Mostafa A. El-Sayed, "Preparation and Growth Mechanism of Gold Nanorods (NRs) Using Seed-Mediated Growth Method," *Chemistry of Materials* **15**(10), 1957-1962 (2003).
169. G. Decher, J. D. Hong, and J. Schmitt, "Buildup of ultrathin multilayer films by a self-assembly process: III. Consecutively alternating adsorption of anionic and cationic polyelectrolytes on charged surfaces," *Thin Solid Films*, **210-211**(2), 831-835 (1992).
170. Alexander G. Tkachenko, Huan Xie, Yanli Liu, Donna Coleman, Joseph Ryan, Wilhelm R. Glomm, Mathew K. Shipton, Stefan Franzen, and Daniel L. Feldheim, "Cellular Trajectories of Peptide-Modified Gold Particle Complexes: Comparison of Nuclear Localization Signals and Peptide Transduction Domains," *Bioconjugate Chemistry* **15**(3), 482-490 (2004).
171. N. L. Rosi and C. A. Mirkin, "Nanostructures in Biodiagnostics," *Chem. Rev.* **105**, 1547-1562 (2005).
172. S. H. Brewer, W. R. Glomm, M. C. Johnson, M. K. Knag, and S. Franzen, "Probing BSA Binding to Citrate-Coated Gold Nanoparticles and Surfaces," *Langmuir* **21**, 9303-9307 (2005).
173. N. Patel, M. C. Davies, R. J. Heaton, C. J. Roberts, S. J. B. Tendler, and P. M. Williams, "A scanning probe microscopy study of the physisorption and chemisorption of protein molecules onto carboxylate terminated self-assembled monolayers," *Applied Physics A: Materials Science & Processing* **66**(Supplement 1), S569-S574 (1998).
174. T. K. Sau and C. J. Murphy, "Seeded High Yield Synthesis of Short Au Nanorods in Aqueous Solution," *Langmuir* **20**(15), 6414-6420 (2004).
175. S. Link, M. B. Mohamed, and M. A. El-Sayed, "Simulation of the Optical Absorption Spectra of Gold Nanorods as a Function of Their Aspect Ratio and the Effect of the Medium Dielectric Constant," *J. Phys. Chem. B* **103**, 3073-3077 (1999).
176. Stuart W. Prescott and Paul Mulvaney, "Gold nanorod extinction spectra," *Journal of Applied Physics* **99**(12), 123504 (2006).
177. O. Valdes-Aguilera, L. Cincotta, J. Foley, and I. E. Kochevar, "Photobleaching of a Cyanine Dye in Solution and in Membranes," *Photochemistry and Photobiology* **45**, 337-344 (1987).
178. J. R. Lakowicz, "Time-Domain Lifetime Measurements," in *Principles of Fluorescence Spectroscopy*, 2nd ed. (Kluwer Academic/Plenum, New York, 1999), pp. 95-184.

179. Shunsuke Ohnishi, Stephen J. Lomnes, Rita G. Laurence, Andrew Gogbashian, Giuliano Mariani, and John V. Frangioni, "Organic Alternatives to Quantum Dots for Intraoperative Near-Infrared Fluorescent Sentinel Lymph Node Mapping," *Molecular Imaging* **4**(3), 172-181 (2005).
180. T. Soller, M. Ringler, M. Wunderlich, T. A. Klar, J. Feldmann, H.-P. Josel, Y. Markert, A. Nichtl, and K. Kurzinger, "Radiative and Nonradiative Rates of Phosphors Attached to Gold Nanoparticles," *Nano Lett.* **7**(7), 1941 - 1946 (2007).
181. Brian O'Regan and Michael Grätzel, "A low-cost, high-efficiency solar cell based on dye-sensitized colloidal TiO<sub>2</sub> films," *Nature* **353**(6346), 737-740 (1991).
182. Kylie R Catchpole, "Nanostructures in photovoltaics," *Philosophical Transactions of the Royal Society A* **364**(1849), 3493-3503 (2006).
183. D. M. Schaadt, B. Feng, and E. T. Yu, "Enhanced semiconductor optical absorption via surface plasmon excitation in metal nanoparticles," *Applied Physics Letters* **86**(6), 063106 (2005).
184. D. Derkacs, S. H. Lim, P. Matheu, W. Mar, and E. T. Yu, "Improved performance of amorphous silicon solar cells via scattering from surface plasmon polaritons in nearby metallic nanoparticles," *Applied Physics Letters* **89**(9), 093103 (2006).
185. S. Pillai, K. R. Catchpole, T. Trupke, and M. A. Green, "Surface plasmon enhanced silicon solar cells," *Journal of Applied Physics* **101**(9), 093105 (2007).
186. S. H. Lim, W. Mar, P. Matheu, D. Derkacs, and E. T. Yu, "Photocurrent spectroscopy of optical absorption enhancement in silicon photodiodes via scattering from surface plasmon polaritons in gold nanoparticles," *Journal of Applied Physics* **101**(10), 104309 (2007).
187. Howard R. Stuart and Dennis G. Hall, "Absorption enhancement in silicon-on-insulator waveguides using metal island films," *Applied Physics Letters* **69**(16), 2327-2329 (1996).
188. Tsutomu Ishi, Junichi Fujikata, Kikuo Makita, Toshio Baba, and Keishi Ohashi, "Si Nano-Photodiode with a Surface Plasmon Antenna," *Jpn. J. Appl. Phys.* **44**, L364-L366 (2005).
189. Liang Tang, David A. Miller, Ali K. Okyay, Joseph A. Matteo, Yin Yuen, Krishna C. Saraswat, and Lambertus Hesselink, "C-shaped nanoaperture-enhanced germanium photodetector," *Optics Letters* **31**(10), 1519-1521 (2006).
190. Kannan Balasubramanian, Marko Burghard, Klaus Kern, Matteo Scolari, and Alf Mews, "Photocurrent Imaging of Charge Transport Barriers in Carbon Nanotube Devices," *Nano Letters* **5**(3), 507-510 (2005).

191. Serhiy Malynych, Igor Luzinov, and George Chumanov, "Poly(Vinyl Pyridine) as a Universal Surface Modifier for Immobilization of Nanoparticles," *Journal of Physical Chemistry B* **106**(6), 1280-1285 (2002).
192. Isabel Romero, Javier Aizpuru, Garnett W. Bryant, and F. Javier García De Abajo, "Plasmons in nearly touching metallic nanoparticles: singular response in the limit of touching dimers," *Optics Express* **14**(21), 9988-9999 (2006).
193. Alex W. H. Lin, Nastassja A. Lewinski, Jennifer L. West, Naomi J. Halas, and Rebekah A. Drezek, "Optically tunable nanoparticle contrast agents for early cancer detection: model-based analysis of gold nanoshells," *Journal of Biomedical Optics* **10**(6), 064035 (2005).
194. P. Nordlander and E. Prodan, "Plasmon Hybridization in Nanoparticles near Metallic Surfaces," *Nano Letters* **4**(11), 2209-2213 (2004).
195. F. Moreno, F. González, and J. M. Saiz, "Plasmon spectroscopy of metallic nanoparticles above flat dielectric substrates," *Optics Letters* **31**(12), 1902-1904 (2006).
196. Victor V. Gozhenko, Leonid G. Grechko, and Keith W. Whites, "Electrodynamics of spatial clusters of spheres: Substrate effects," *Physical Review B* **68**(12), 125422 (2003).
197. E. Prodan, P. Nordlander, and N. J. Halas, "Effects of dielectric screening on the optical properties of metallic nanoshells," *Chemical Physics Letters* **368**(1-2), 94-101 (2003).
198. Daniel W. Brandl, Chris Oubre, and Peter Nordlander, "Plasmon hybridization in nanoshell dimers," *Journal of Chemical Physics* **123**(2), 024701 (2005).
199. M. V. Bashevoy, V. A. Fedotov, and N. I. Zheludev, "Optical whirlpool on an absorbing metallic nanoparticle," *Optics Express* **13**(21), 8372-8379 (2005).
200. Michael I. Tribelsky and Boris S. Luk'yanchuk, "Anomalous Light Scattering by Small Particles," *Physical Review Letters* **97**(26), 263902 (2006).
201. B. S. Luk'yanchuk, M. I. Tribelsky, Z. B. Wang, Y. Zhou, M. H. Hong, L. P. Shi, and T. C. Chong, "Extraordinary scattering diagram for nanoparticles near plasmon resonance frequencies," *Applied Physics A: Materials Science & Processing* **89**(2), 259-264 (2007).
202. Sadao Adachi, *Optical Constants of Crystalline and Amorphous Semiconductors - Numerical Data and Graphical Information* (Kulwer Academic Publishers, Norwell, MA, 1999).

203. Z. B. Wang, B. S. Luk'yanchuk, M. H. Hong, Y. Lin, and T. C. Chong, "Energy flow around a small particle investigated by classical Mie theory," *Physical Review B* **70**(3), 035418 (2004).
204. Stefano Palomba and Lukas Novotny, "Near-Field Imaging with a Localized Nonlinear Light Source," *Nano Letters* **9**(11), 3801–3804 (2009).
205. Hongxing Xu, Erik J. Bjerneld, Mikael Käll, and Lars Börjesson, "Spectroscopy of Single Hemoglobin Molecules by Surface Enhanced Raman Scattering," *Physical Review Letters* **83**(21), 4357-4360 (1999).
206. J. Britt Lassiter, Javier Aizpurua, Luis I. Hernandez, Daniel W. Brandl, Isabel Romero, Surbhi Lal, Jason H. Hafner, Peter Nordlander, and Naomi J. Halas, "Close Encounters between Two Nanoshells," *Nano Letters* **8**(4), 1212-1218 (2008).
207. Lisa V. Brown, Heidar Sobhani, J. Britt Lassiter, Peter Nordlander, and Naomi J. Halas, "Heterodimers: Plasmonic Properties of Mismatched Nanoparticle Pairs," *ACS Nano* **4**(2), 819-832 (2010).
208. F. Le, N. Z. Lwin, J. M. Steele, M. Käll, N. J. Halas, and P. Nordlander, "Plasmons in the Metallic Nanoparticle-Film System as a Tunable Impurity Problem," *Nano Letters* **5**(10), 2009-2013 (2005).
209. Jack J. Mock, Ryan T. Hill, Aloyse Degiron, Stefan Zauscher, Ashutosh Chilkoti, and David R. Smith, "Distance-Dependent Plasmon Resonant Coupling between a Gold Nanoparticle and Gold Film," *Nano Letters* **8**(8), 2245-2252 (2008).
210. F. Le, N. Z. Lwin, N. J. Halas, and P. Nordlander, "Plasmonic interactions between a metallic nanoshell and a thin metallic film," *Physical Review B* **76**(16), 165410 (2007).
211. H. Ditlbacher, A. Hohenau, D. Wagner, U. Kreibig, M. Rogers, F. Hofer, F. R. Aussenegg, and J. R. Krenn, "Silver nanowires as surface plasmon resonators," *Physical Review Letters* **95**(25), 257403 (2005).
212. Yurui Fang, Hong Wei, Feng Hao, Peter Nordlander, and Hongxing Xu, "Remote-Excitation Surface-Enhanced Raman Scattering Using Propagating Ag Nanowire Plasmons," *Nano Letters* **9**(5), 2049-2053 (2009).
213. F. Hao and P. Nordlander, "Plasmonic coupling between a metallic nanosphere and a thin metallic wire," *Applied Physics Letters* **89**(10), 103101 (2006).
214. J. Britt Lassiter, Mark W. Knight, Nikolay A. Mirin, and Naomi J. Halas, "Reshaping the Plasmonic Properties of an Individual Nanoparticle," *Nano Letters* **9**(12), 4326-4332 (2009).

215. K. J. Siemsen and H. D. Riccius, "Experiments with point-contact diodes in the 30–130 THz frequency region," *Applied Physics A: Materials Science & Processing* **35**(3), 177-187 (1984).
216. V. Daneu, D. Sokoloff, A. Sanchez, and A. Javan, "Extension of Laser Harmonic-Frequency Mixing Techniques Into The 9  $\mu\text{m}$  Region With An Infrared Metal-Metal Point-Contact Diode," *Applied Physics Letters* **15**(12), 398-401 (1969).
217. K. M. Evenson, M. Inguscio, and D. A. Jennings, "Point Contact Diode at Laser Frequencies," *J. Appl. Phys.* **57**(3), 956-960 (1985).
218. D. J. E. Knight and P. T. Woods, "Application of nonlinear devices to optical frequency measurement," *Journal of Physics E: Scientific Instruments* **9**(11), 898-916 (1976).
219. Yookyung Jung, Hongtao Chen, Ling Tong, and Ji-Xin Cheng, "Imaging Gold Nanorods by Plasmon-Resonance-Enhanced Four Wave Mixing," *Journal of Physical Chemistry C* **113**(7), 2657–2663 (2009).
220. Jan Renger, Romain Quidant, Nick Van Hulst, and Lukas Novotny, "Surface-Enhanced Nonlinear Four-Wave Mixing," *Physical Review Letters* **104**(4), 046803 (2010).
221. Mark W. Knight, Nathaniel K. Grady, Rizia Bardhan, Feng Hao, Peter Nordlander, and Naomi J. Halas, "Nanoparticle-Mediated Coupling of Light into a Nanowire," *Nano Letters* **7**(8), 2346-2350 (2007).
222. P. Nordlander and F. Le, "Plasmonic structure and electromagnetic field enhancements in the metallic nanoparticle-film system," *Applied Physics B: Lasers and Optics* **84**(1-2), 35-41 (2006).
223. Oscar Eduardo Martinez, "300 Times Grating Compressor with Positive Group Velocity Dispersion: Application to Fiber Compensation in 1.3-1.6  $\mu\text{m}$  Region," *IEEE Journal of Quantum Electronics* **QE-23**(1), 59-64 (1987).
224. John M. Dudley, Goëry Genty, and Stéphane Coen, "Supercontinuum generation in photonic crystal fiber," *Reviews of Modern Physics* **78**(4), 1135-1184 (2006).
225. John M. Dudley, Xun Gu, Lin Xu, Mark Kimmel, Erik Zeek, Patrick O'Shea, Rick Trebino, Stéphane Coen, and Robert S. Windeler, "Cross-correlation frequency resolved optical gating analysis of broadband continuum generation in photonic crystal fiber: simulations and experiments," *Optics Express* **10**(21), 1215-1221 (2002).
226. Zhaoju Luo, "Linear Optical Thin Films Formed by Electrostatic Self-Assembly," (Virginia Polytechnic Institute and State University, Blacksburg, Virginia, 2000).

227. Frank N. Crespilho, Valtencir Zucolotto, Osvaldo N. Oliveira Jr., and Francisco C. Nart, "Electrochemistry of Layer-by-Layer Films: a review," *Int. J. Electrochem. Sci.* **1**(5), 194-214 (2006).
228. Stephan T. Dubas and Joseph B. Schlenoff, "Factors Controlling the Growth of Polyelectrolyte Multilayers," *Macromolecules* **32**(24), 8153-8160 (1999).
229. Hazel L. Tan, Meredith J. McMurdo, Guiquan Pan, and P. Gregory Van Patten, "Temperature Dependence of Polyelectrolyte Multilayer Assembly," *Langmuir* **19**(22), 9311-9314 (2003).
230. E.C. Le Ru and P.G. Etchegoin, "Rigorous justification of the  $|E|^4$  enhancement factor in Surface Enhanced Raman Spectroscopy," *Chemical Physics Letters* **523**(1-3), 63-66 (2006).
231. Jorge Zuloaga, Emil Prodan, and Peter Nordlander, "Quantum Description of the Plasmon Resonances of a Nanoparticle Dimer," *Nano Letters* **9**(2), 887-891 (2009).
232. Mark W. Knight and N. J. Halas, "Nanoshells to nanoeggs to Nanocups: symmetry breaking beyond the quasistatic limit in complex plasmonic nanoparticles," *New Journal of Physics* **10**, 105006 (2008).
233. Matthew Pelton, Mingzhao Liu, Sungnam Park, Norbert F. Scherer, and Philippe Guyot-Sionnest, "Ultrafast resonant optical scattering from single gold nanorods: Large nonlinearities and plasmon saturation," *Physical Review B* **73**(15), 155419 (2006).
234. V V Kruglyak, R J Hicken, M Ali, B J Hickey, A T G Pym, and B K Tanner, "Ultrafast third-order optical nonlinearity of noble and transition metal thin films," *Journal Of Optics A: Pure And Applied Optics* **7**(2), S235-S240 (2005).
235. Hongkun Park, Andrew K. L. Lim, A. Paul Alivisatos, Jiwoong Park, and Paul L. McEuen, "Fabrication of metallic electrodes with nanometer separation by electromigration," *Applied Physics Letters* **75**(2), 301-303 (1999).
236. Daniel R. Ward, Nathaniel K. Grady, Carly S. Levin, Naomi J. Halas, Yanpeng Wu, Peter Nordlander, and Douglas Natelson, "Electromigrated Nanoscale Gaps for Surface-Enhanced Raman Spectroscopy," *Nano Letters* **7**(5), 1396-1400 (2007).